ULTRASHORT AND SHORT PULSED FIBER LASER DEVELOPMENT FOR TRANSPARENT MATERIAL PROCESSING, IMAGING AND SPECTROSCOPY APPLICATIONS

A DISSERTATION SUBMITTED TO

THE GRADUATE SCHOOL OF ENGINEERING AND SCIENCE

OF BILKENT UNIVERSITY

IN PARTIAL FULFILLMENT OF THE REQUIREMENTS FOR

THE DEGREE OF

DOCTOR OF PHILOSOPHY

IN

MATERIALS SCIENCE AND NANOTECHNOLOGY

By

Seydi Yavaş

January, 2015

ULTRASHORT AND SHORT PULSED FIBER LASER DEVELOPMENT FOR TRANSPARENT MATERIAL PROCESSING, IMAGING AND SPECTROSCOPY APPLICATIONS

By Seydi Yavaş

January, 2015

We certify that we have read this thesis and that in our opinion it is fully adequate, in scope and in quality, as a dissertation for the degree of Doctor of Philosophy.

Assoc. Prof. Dr. Fatih Ömer İlday(Advisor)

Assist. Prof. Dr. Giovanni Volpe

Assoc. Prof. Dr. Hilmi Volkan Demir

Assoc. Prof. Dr. Hakan Altan

Prof. Dr. Oğuz Gülseren

Approved for the Graduate School of Engineering and Science:

Prof. Dr. Levent Onural
Director of the Graduate School

ABSTRACT

ULTRASHORT AND SHORT PULSED FIBER LASER DEVELOPMENT FOR TRANSPARENT MATERIAL PROCESSING, IMAGING AND SPECTROSCOPY APPLICATIONS

Seydi Yavaş
PhD in Materials Science and Nanotechnology
Advisor: Assoc. Prof. Dr. Fatih Ömer İlday
January, 2015

Since the invention of the laser in the 60s, the main advances in laser technology were done in two directions; shorter pulses and higher powers. In order to achieve this purpose, many laser types are developed and always replaced with simpler, smaller, cheaper alternatives that can deliver the same or better parameters. In the past 20 years, fiber lasers have become an important alternative that can match and even enhance the performance of currently used lasers while reducing the complexity, costs and instability.

Optical fibers, which are the main components of fiber lasers, were first developed just as a substitute for conventional cables since they offer much less attenuation in carrying signals over long ranges. So, most of the studies were focused on making the fibers better for communication channels. After realizing that fiber lasers offer better beam qualities, which is also a vital parameter for many laser applications, researches started finding ways to use fibers for lasers and they achieved this in 80s by the first ever utilization of low-attenuation active fibers. After the invention of double-clad fibers, utilization of diode lasers for pumping and development of efficient rare-earth doped fibers, fiber lasers became more than just a research topic in the laboratory and began to find use in many applications.

The utilization of fiber lasers for short (nanoseconds) and ultrashort (picoseconds, femtoseconds) pulse generation was a difficult task for researchers. The biggest challenge to overcome was nonlinear effects caused by the confinement of the beam into small volumes. By using smart designs like chirped pulse amplification and highly doped lasers, pulse energies and peak powers close to solid-state ultrafast lasers can be achieved. These nonlinear effects were not just problems in the power scalability of fiber lasers, on the other hand, they were an opportunity for new possible applications. For example, using these nonlinear effects inside

fibers, supercontinuum generation was demonstrated and found usage in many areas like spectroscopy, imaging and metrology.

Today, more than 50 worldwide companies sell short-pulse fiber lasers for applications as diverse as ophthalmology, micromachining, medical imaging and precision metrology. Especially, fiber-laser-based micromachining is routinely implemented in the fabrication processes for widely used consumer products. New applications of fiber lasers are being continuously developed.

Consequently, in this Ph.D. thesis study, new application areas of fiber lasers are investigated. Ultrashort and short pulsed fiber lasers are developed and utilized for biological and transparent material processing, spectroscopy and imaging. In the first part of thesis study, we have demonstrated the use of a custom-built fiber laser-based microscope system for nanosurgery and tissue ablation experiments. Through the use of custom FPGA electronics acting through fiber-coupled AOMs, we are able to generate custom pulse sequence. Using this system, we have made photodisruption experiments in tissue level, cellular level and sub-cellular level.

In the second part of this thesis study, in collaboration with Bogazici University, we have developed a nanosecond fiber laser system that is able to generate wavelength components of 600 nm to 1300 nm, developed specifically for photoacoustic excitation. Using this system, we have made photoacoustic signal excitation in a ceramic sample and prepared the system for further experiments to generate photoacoustic images from biological specimens.

In the third part of thesis study, in collaboration with ODTU, the development of a THz-TDS system driven by a novel Yb-doped fiber laser whose repetition rate can be tuned, specifically for fast scan THz measurements, is realized. Characterization of the built laser system is done considering the necessities for the OSCAT technique as an alternative method for fast scan THz measurements. Stability of the oscillator is examined in terms of power, spectrum and pulse duration with the changing repetition rate of the laser. Using this system THz waveforms are generated at different wavelengths and the system is prepared for further research in spectroscopy.

In the last part of the thesis study, a high-pulse energy femtosecond laser system is developed and utilized for transparent material processing. The laser output is coupled to a fast galvo-scanner system, and a synchronized translation stage such that very wide areas (10 cm x 10 cm) are able to be processed with very high speed (2 m/s). Using this system, glass samples are cut, engraved and

photodarkened.

Keywords: Ultrashort Pulse Laser, Ultrafast Laser, Fiber Laser, Fiber Amplifier, High Pulse Energy Laser, Ultrafast Material Processing, Nanosurgery, Tissue Ablation, Multiphoton Ablation, Photoacoustic Imaging, Supercontinuum Generation, Photothermal Effects, THz Spectroscopy, Photodarkening, Glass Processing.

ÖZET

TRANSPARAN MALZEME İŞLEME, GÖRÜNTÜLEME VE SPEKTROSKOPİ AMAÇLI ULTRA KISA VE KISA ATIMLI FİBER LAZER GELİŞTİRİLMESİ

Seydi Yavaş
Malzeme Bilimi ve Nanoteknoloji, Doktora
Tez Danışmanı: Doç. Dr. Fatih Ömer İlday
Ocak, 2015

60'lı yıllarda lazerin icadından bu yana lazer teknolojisindeki gelişmeler temel olarak iki yönde ilerlemiştir; daha kısa atım üretme ve daha yüksek güçlere ulaşma. Bunu başarabilmek için birçok farklı lazer tipi geliştirilmiş ve bu lazer tipleri her seferinde, aynı işi ya da daha iyisini yapabilen, daha basit, daha küçük ve daha ucuz alternatiflerle yer değiştirmiştir. Son 20 yılda da fiber lazerler mevcut lazer teknolojisine önemli bir alternatif olarak ortaya çıkmış ve mevcut parametreleri daha da ileri götürmeyi başarırken bunu daha az sistem karmaşıklığı, maliyeti ve kararsızlığı ile sunmuştur.

Fiber lazerlerin temelini oluşturan optik fiberler ilk olarak yaygın olarak kullanılan kablolara alternatif olması için telekomünikasyon alanında, sinyalleri düşük kayıpla uzun mesafelere taşıyabilmesi sebebiyle kullanılmaya başlanmıştır. Bu nedenle fiber optik alanındaki çalışmaların çoğu fiberleri daha etkin telekomünikasyon kanalları yapmaya yoğunlaşmıştır. Fiberlerin yüksek kalitede lazer demeti sağlayabildiğinin fark edilmesi ve bu parametrenin lazerler için de önemli olması sebebiyle fiberlerin lazer alanında kullanılması için araştırmalar yapılmaya başlanmış ve 80li yıllarda ilk aktif fiberlerin düşük kayıplı olarak üretilmesiyle sonuçlar alınmaya başlanmıştır. Çift-kılıflı fiberlerin üretilmesi, diyot lazerlerin aktif fiberleri pompalama amaçlı kullanılmaya başlanması ve verimli nadir element katkılı fiberlerin geliştirilmesiyle fiber lazerler yalnızca laboratuvarda bir araştırma konusu olmaktan çıkıp birçok uygulama alanında kullanılmaya başlanmıştır.

Fiber lazerlerin kısa (nanosaniye) ve ultra kısa (pikosaniye ya da femtosaniye) atım üretmede kullanılmaya başlanması araştırmacılar için zorlu bir görev olmuştur. En büyük zorluk lazer demetinin içinde ilerlediği dalga kılavuzu ortamında küçük bir hacme sıkıştırılmış olan ışığın doğrusal olmayan etkilere sebep olmasıdır. Genişletilmiş atım yükseltgenmesi ve yüksek katkılı fiberlerin

kullanılması gibi zekice tasarımlarla, yalnızca katı-hal lazerlerle elde edilmesi mümkün olan yüksek atım enerjilerine ve tepe güçlerine ulaşılmıştır. Doğrusal olmayan etkiler gücün artırılabilmesi için sorun teşkil etmesinin yanı sıra bir taraftan da birçok yeni uygulama alanı için fırsat sunmaktadır. Örnek olarak, doğrusal olmayan etkilerin fiber içinde kullanımı ile süper tayf üretilebilmektedir ve spektroskopi, görüntüleme, metroloji gibi değişik alanlarda kullanımı bulmaktadır.

Günümüzde 50den fazla şirket kısa atımlı fiber lazer satmaktadır ve bu lazerler optalmolojiden, malzeme işlemeye, medikal görüntülemeden hassas metroloji uygulamalarına birçok alanda kullanılmaktadır. Özellikle fiber lazer temelli mikron hassasiyetinde malzeme işleme birçok ürünün üretimi için rutin olarak kullanılmaktadır. Fiber lazerlerin yeni uygulamaları da sürekli gelişim içindedir.

Sonuç olarak, bu doktora tez çalışmasında fiber lazerlerin yeni uygulama alanları araştırılmıştır. Ultrakısa ve kısa atımlı fiber lazerler biyolojik malzeme işleme, saydam malzeme işleme, spektroskopi ve görüntüleme amaçlı olarak uygulamaya özel şekilde tasarlanmış ve gerçeklenmiştir. Tezin ilk kısmında ultrahızlı atımlara sahip bir fiber lazer mikroskopa entegre edilmiş ve bu sistem ile nanocerrahi ve doku yıkımlama deneyleri gerçekleştirilmiştir. Akusto-optik değiştirimcileri kontrol eden FPGA temelli elektronik devre tasarımları ile atım dizileri isteğe bağlı olarak herhangi bir sınırlama olmaksızn üretilebilmiştir. Bu sistem kullanılarak yıkımlama deneyleri doku, hücre ve hücre-alı seviyede denenmiştir. Tez çalışmasının ikinci kısmında Boğaziçi Üniversitesi ile ortak olarak geliştirilen nanosaniye atımlara sahip 600-1300 nm aralığında dalgaboylarına sahip fiber lzer sisemi geliştirilmiş ve fotoakustik görüntüleme deneyleri için kullanıma hazır hale getirilmiştir. Bu sistem kullanılarak, seramik bir örnekten fotoakustik sinyal üretilmesi denenmiş ve geliştirilen sistem biyolojik malzemelerden fotoakustik görüntüleme elde etmeye hazır hale getirilmiştir.

Tez çalışmasının üçüncü kısmında ODTÜ ile ortak bir çalışma çerçevesinde THz-TDS sisteminde kullanılmak üzere özgün bir femtosaniye atımlı, Yb-katkılı, atım tekrar sıklığı kaydırılabilen fiber lazer geliştirilmiş ve THz ölçümleri için kullanıma hazır hale getirilmiştir. Geliştirilen lazer sisteminin THz öçümleri için gerekli OSCAT tekniğine uygun olup olmadığı kaydırma işlemi sırasındaki kararlılığı karakterize edilerek test edilmiştir. Lazer salıngacından elde edilen optik güç, spektrum ve atım süresi değişimleri ölçülmüştür. Bu sistem kullanılarak THz sinyal üretimi gerçekleştirilmiş ve spektroskopi ölçümleri için hazırlanmıştır.

Tez çalışmasının son kısmında saydam malzeme işleme amaçlı, yüksek atım

enerjili femtosaniye atımlı fiber lazer geliştirilmiştir. Geliştirilen lazerin çıkışı galvo-tarayıcıya iletilmiş ve bu tarayıcıyla senkronize hareket eden bir konumlama sistemi ile geniş alanları (10 cm x 10 cm) yüksek tarama hızında (2 m/s) taramak mümkün hale gelmiştir. Bu sistem kullanılarak cam örnekler üzerinde kesme, kazıma ve cam içinde karartma deneyleri yapılmıştır.

Anahtar sözcükler: Ultrakısa Atımlı Lazer, Ultrahızlı Lazer, Fiber Lazer, Fiber Yükselteç, Yüksek Atım Enerjili Lazer, Ultrahızlı Malzeme İşleme, Nanocerrahi, Doku Kesimleme, Çok-fotonlu Kesimleme, Fotoakustik Görüntüleme, Süpertayf Üretme, Fototermal Etkiler, THz Spektroskopisi, Fotokarartma, Cam İşleme.

Acknowledgement

I sincerely would like to thank to my supervisor F. Ömer İlday for his invaluable support, guidance and encouragement. He has not only guided me through my thesis but has also inspired me to see the bigger picture in any problem I encountered. He has been an excellent scientist with great aims and I am very grateful to have had the opportunity to work with him.

I would also like to thank Hamit Kalaycıoğlu for being a tutor and a second advisor, during my studies. He always sets an example for the young people for his determination and left us no excuse to give up in any situation.

I would like to thank all the former group members of UFOLAB, especially Levent Budunoğlu, Coşkun Ülgüdür, Kıvanç Özgören, Bülent Öktem, Alper Bayrı and Ebru Bayrı, not only for their collaborations, beneficial scientific discussions and for being helpful to me but also for being great friends outside of the lab too.

I would especially like to thank Mutlu Erdoğan and his wife Emel Erdoğan for their long-standing friendship beginning from the days in Ankara University and still going on.

I would like to thank the rest of the present UFOLAB members for their collaboration.

I would like to thank Ihor Pavlov, Onur Tokel and Önder Akçaalan for the fruitful scientific and non-scientific discussions.

During my thesis study, I had the opportunity to collaborate with great people from different groups that I enjoyed to work with. Here, I want to thank Mehmet Burçin Ünlü and his Medical & Biological Physics Group members Esra Aytaç Kipergil, Hakan Erkol, Ümit Arabul and the rest of his team for their patience and hospitality during the collaboration. I also want to thank Hakan Altan and his Terahertz Research Laboratory members Hakan Keskin and Yakup Midilli for their collaboration and enthusiasm. I want to thank also Şişecam R&D department as well as TOBB University Solar Cell Group members.

I sincerely would like to thank to my colleagues in FiberLAST, Inc., Koray Eken, Emre Yağcı, Ozan Aydın, Sarper Salman, Volkan Helvacı, Mesut Tasalı, Ramazan Çam, Veronika Ciernikova, Mehmet Ali Marar, Aykut Altınkaynak and Elif Gürleyik for their great collaboration and being helpful.

I would like to thank my dear friends Ceyda Günsel and Ceren Serap Akın for their friendship and encouragement.

I especially would like to thank Şöhret Görkem Karamuk for her support in any part of my thesis study during this tiring period.

Last but not the least; I would like to thank my parents Ganime and Şeref Yavaş in addition to my sister Hatice Güney for their endless support during my studies.

I would also like to thank my thesis committee members for sparing their valuable time and for their reviews and corrections on my thesis.

The financial support during my studies from TÜBITAK, Bilkent University and UNAM are also gratefully acknowledged.

Seydi Yavaş,

January, 2015

Dedicated to my family...

Contents

1 Introduction **1**

1.1 Optical Fibers 1

1.2 Nonlinear Optics 5

1.2.1 Nonlinear Schrödinger Equation 8

1.2.2 Dispersion in Optical Fibers 10

1.2.3 Self-Phase Modulation in Fibers 13

1.3 Rare-Earth Doped Fibers 15

1.4 Photonic Crystal Fibers 16

1.5 Fiber Lasers 20

1.6 Mode-Locking through Polarization Rotation 23

1.7 Fiber Amplifiers 28

1.8 Pulse Pickers 35

1.8.1 Acousto-Optic Effect 36

1.9 Material Processing with Ultrafast Lasers 38

1.9.1 Semiconductors 38

1.9.2 Dielectrics 41

2 Femtosecond Fiber Laser-Microscope System Development for Nanosurgery **45**

2.1 Introduction 45

2.2 Laser-Biological Material Interaction 46

2.2.1 Absorption 47

2.2.2 Tissue Ablation 49

2.2.3 Photodisruption 50

2.3 Experimental Setup and Results 52

2.3.1 Fiber Laser System 53
2.3.2 Customized Microscope Setup 56
2.3.3 Control Electronics and Software 57
2.4 Laser Experiments on Biological Samples and Results 58
2.5 Conclusion 61

3 Nanosecond Supercontinuum Fiber Laser System for Photoacoustic Microscopy 62
3.1 Introduction 62
3.2 Theoretical Background 63
3.2.1 Photothermal Effects 63
3.2.2 Photoacoustic Imaging 64
3.2.3 Supercontinuum Generation 66
3.3 Experimental Setup 68
3.3.1 Oscillator 68
3.3.2 Preamplifiers and AOM for Repetition Rate Control 69
3.3.3 Power Amplifier and Supercontinuum Generation 70
3.4 Photoacoustic Signal Results 73
3.5 Conclusion 74

4 Femtosecond Fiber Laser Development for Terahertz Spectroscopy 76
4.1 Introduction 76
4.2 THz-Time Domain Spectroscopy 77
4.3 Fast Scan THz Detection Method:OSCAT 80
4.4 Fiber Laser Results 84
4.4.1 Laser Setup 84
4.4.2 Laser Characterization 86
4.5 THz-TDS Measurements at Different repetition Rates of the Fiber Laser 93
4.6 Conclusion 96

5 Femtosecond Fiber Laser System Development for Glass Processing 99

5.1 Introduction 99
5.2 Theoretical Background 100
5.2.1 Ultrashort Pulse-Transparent Material Interaction 104
5.2.2 Applications of Ultrafast Laser Glass Processing 106
5.3 Results 108
5.3.1 Laser Setup 108
5.3.2 Glass Processing Results 112
5.4 Conclusion 115

6 Conclusion **117**

List of Figures

1.1 Snell's Law 3
1.2 Temporal (up) and spectral (down) profile of a 150 fs Gaussian pulse before (left) and after (right) propagating through a 1.3 m of a 5 μm single-mode fiber. Here nonlinearity and higher order terms of dispersion are neglected in order to show the effect of group velocity dispersion. In the graph, dotted lines show the change in instantaneous frequency. The group velocity disersion based linear chirp is visible in the right figure. The spectral components that are faster and slower are determined by the sign of β_2. The bottom row illustrates the unchanged spectrum by the effect of pure dispersion. 12
1.3 Temporal (up) and spectral (down) profile of a 150 fs Gaussian pulse before (left) and after (right) propagating through a 30 cm of a single-mode fiber with core diameter of 5 μm. Here dispersion is neglected in order to show the effect of nonlinearity. In the graph, dotted lines show the change in instantaneous frequency. During propagation the central part of the pulse becomes linearly chirped while the wings of the pulse obtains higher order phase. The bottom row illustrates the spectral alteration in the pulse and it is visible that new frequency components are created due to nonlinearity. 14
1.4 Pumping/emission band schematic (left) and absorption/emission spectra (right) of Ytterbium-doped fiber 16

1.5 When the beam encounters an air defect in silica, it is transmitted or reflected depending on the incidence angle. In the case of the product of the transverse wavevector and the thickness of the defect is an odd multiple of π, the light is resonantly guided in the waveguide. 17
1.6 Photonic bandgap fiber SEM image. The beam is trapped in the core part (diameter is around 9 μm) that is filled with air and surrounded by anti-resonant structures that prevents the light to escape. 18
1.7 a) Schematic for a PCF. Here solid core, with a diameter of D, constitutes a defect in a regular array of air holes. The size of the air holes (given with d), and the distance between them (given with Λ are vital parameters and should be preserved throughout the fiber for the guiding to be achieved. b) SEM image of a realized PCF structure 19
1.8 Nonlinear polarization rotation mechanism inside optical fiber . . 26
1.9 Three-level and four-level pumping schemes for fiber amplifiers. Wavy arrows indicate nonradiative fast transitions 29
1.10 Excitation in semiconductor by single and multiphoton absorption 39
1.11 Secondary processes take place on different time scales 40
1.12 Measured and calculated ablation thresholds for fused silica. The deviation from $\tau^{(1/2)}$ indicates that there forms a new region that is nonthermal 42
1.13 a) Nanosecond, b) femtosecond processing of tooth samples 43

2.1 Absorption spectra for water and most commonly found chromophores inside tissue 48
2.2 Laser-tissue interaction mechanisms for different laser durations and intensities 49
2.3 Schematic showing the development of optical breakdown due to ultrafast pulses inside tissue 52
2.4 Schematic of the laser setup. FPGA: field programmable gate array; AOM: acousto-optic modulator. 53

2.5 Spectrum and autocorrelation data of the compressed laser amplifier output 55
2.6 Schematic for electronics circuitry to control pulses and form arbitrary pulse pattern via AOMs 56
2.7 Schematic of the laser-fluorescence microscope optics 57
2.8 FPGA circuit scheme used for rep. rate adjustment and arbitrary pulse pattern generation using AOMs 58
2.9 Tissue slice (mouse gastrocnemius muscle) (a) before and (b) after ablation; 4.08 MHz, 240-fs, 7-nJ. 59
2.10 Fixed Saos-2 cells (c) before and (d) after sub-cellular surgery; 4.08 MHz, 240-fs, 7 nJ. 59
2.11 (a) Before and (b) after ablation of single mitochondrion stained with Mitotracker Red 580; 4.08 MHz, 240-fs, 2 nJ. 60
2.12 (a) Before and (b) after ablation of single mitochondrion stained with Mitotracker Red 580; 4.08 MHz, 240-fs, 2 nJ. 60
2.13 (a) Before and (b) at the moment of laser axotomy (white arrow indicates the incident laser beam on the axon). (c) After axotomy (white dashed arrow indicates the micro-damage); 32.7 MHz, 240-fs, 8 nJ. 61

3.1 Schematic showing basic mechanisms for photoacoustic imaging . 65
3.2 Schematic for the Oscillator Setup. WDM: Wavelength-division multiplexer. 68
3.3 Schematic of the preamplifiers and AOM 69
3.4 Schematic of the Power Amplifier and PCF for supercontinuum generation 71
3.5 (a)Pulse duration and (b)optical spectrum of the laser at the input of PCF 71
3.6 Photo of the cross-section of the PCF (NKT SC-5.0-1040) used for supercontinuum generation 72
3.7 (a)Spectrum for the generated supercontinuum at the output of the PCF, (b) Photograph of the output of PCF clearly showing that the light is in the visible domain and have different wavelengths together 73

3.8 Photoacoustic signal detected from the ceramic signal 74
3.9 Schematic of the system to be integrated with galvo scanner system and photoacoustic tunable filter 75

4.1 Schematic of a basic time resolved terahertz spectroscopy system based on Ti:sapphire laser 79
4.2 Schematic of a time resolved terahertz spectroscopy system based on fiber laser 82
4.3 Schematic for the OSCAT system 83
4.4 Schematic of the oscillator. QWP: quarter-wave plate; HWP: half-wave plate; BS: beam splitter; PBS: polarizing beam splitter . . . 84
4.5 Schematic of the preamplifier of the fiber laser based THz spectroscopy system 87
4.6 Autocorrelation of the outputs from BS port (left) and PBS port (right). Both of the pulses are directly measured, hence they are uncompressed 88
4.7 Spectrum graph taken from the output from PBS after coupling to the PM collimator 89
4.8 Spectrum graphs taken from the outputs at different locations of the laser oscillator from the fiber coupler outputs 89
4.9 a) RF spectrum data showing the repetition rate values for different positions of the translation stage that is moving the collimator b) Graph showing the linear relation between the translation stage position and the repetition rate of the oscillator 90
4.10 Graph showing the variation of pulse duration with the translation stage position 91
4.11 a) Pulse duration variation by changing the output power of the amplifier, b) The spectrum data taken from the output of the amplifier system 92
4.12 a) The amplifier pump power and obtained signal power, b) Graph showing the fluctuation of the amplifier power by changing the translation stage position at the operating power for spectroscopy measurement 93

4.13 THz-TDS system integrated to the fiber laser. P1-P2: Off-axis parabolic mirrors, FG: Function generator, M1-M5: Mirror, BS: Beam splitter, PCA: Batop PCA-40-05-10-1060-h antenna, DL: Delay line consisting of corner cube on translation stage, L: Lens with focal length 300 mm, ZnTe: <110 >cut ZnTe crystal, QWP: Achromatic quarter wave plate for 700-1100 nm, WP: Wollaston prism, BD: New Focus 2307 balanced photo receiver, Lock-in amplifier: Stanford Research System SR830 Lock-in Amplifier 94
4.14 THz signal for a) 0 mm, b) 3 mm, c) 6 mm oscillator scan stage position. d) Power spectra of the THz signals for different scan stage position 96

5.1 Schematic illustration of key steps in femtosecond-laser-induced structural change in bulk transparent materials. (a)(c) A hot electron-ion plasma is formed in the focal volume through nonlinear absorption of intense femtosecond laser pulses. (d) Depending on the amount of energy contained in the plasma, three different types of structural change can occur: isotropic refractive index change at low energy, birefringent refractive index change at intermediate energy, or void formation at high energy 105
5.2 Schematic of the system built for glass processing 109
5.3 Schematic of the oscillator seeding the glass processing laser system 110
5.4 Spectrum graphs for a) Oscillator PBS port, b) Preamplifier output 111
5.5 Measured temporal profile of 200 kHz pulses and 4-pulsed bursts that are generated via acousto-optic modulator driven by FPGA circuit 112
5.6 Schematic for the electronic system controlling the repetition rate of the system 113
5.7 Photo of the processed glass, alexandrite and quartz samples using femtosecond pulses 114
5.8 Photo and schematic for the glass photodarkening experiments done by changing pulse energy and scanning speed 115

List of Tables

4.1 Scan Types 80
4.2 Calculated OSCAT parameters 86

Chapter 1

Introduction

1.1 Optical Fibers

Optical fiber is a special type of waveguide aimed to enable light beams to propagate long distances by confining them into a small volume. Important parameters such as signal transmission bandwidth and signal propagation distance can be controlled by designing the refractive index of the fiber.

Generally speaking, optical fibers guide light using total internal reflection mechanism using the interface between higher refractive index in the interior side(core) and lower refractive index exterior side (cladding). Most of the modern fibers are produced with a 125 μm cladding diameter and core diameters can be between 1 μm to 100 μm depending on the application the fiber will be used in. The difference between the core and the cladding parts of the fiber can be given on a relative scale as Δ where

$$\Delta = \frac{n_{core} - n_{clad}}{n_{clad}} \tag{1.1}$$

Here n_{core} is the index of core and n_{clad} is the index of cladding. The difference

between cladding and core ranges between .1 % to 3 %. The cladding part of the fiber is covered with a higher refractive index polymer named "coating" that helps to take out the light that is not guided by the core and clad structure.

Total internal reflection mechanism is generally valid when analyzing relatively large core diameter multimode fibers. Total internal reflection takes place by the refraction at an interface which is explained by the Snell's Law:

$$n_1 \sin\theta_1 = n_2 \sin\theta_2 \tag{1.2}$$

where n_1 and n_2 are the refractive indexes of first and second mediums respectively. Here θ_1 is the incidence angle and θ_2 is the refracted beam angle in the second medium. These are shown in Figure 1.1. When $n_2 < n_1$ there is a critical angle, θ_{crit}, which corresponds to $\theta_2 = 90$ and light rays bigger than this angle can't propagate from medium 1 to medium 2. For the case of optical fibers, medium 1 corresponds to the core of the fiber and medium 2 is the cladding. For incidence angle $\theta < \theta_{crit}$, beams are confined to the core and can not escape. For the range of Δ given, critical angle for the beams propagating in the core is ranges from 79° to 86°. Hence, the optical fiber axis and the beam with the critical angle makes an angle between 11° and 4°.

The critical angle for a beam at the input or the output of the fiber is different due to refraction. It is named as critical acceptance angle of the fiber and characterized by the *numerical aperture* (NA) which is equal to the sine of the angle between optical axis of the fiber and critical ray for the end face of the fiber. NA is given as following:

$$NA = \sqrt{{n_{core}}^2 - {n_{clad}}^2} \tag{1.3}$$

so the NA of an optical fiber typically varies between 0.1 to 0.3. When Δ is much smaller than unity, as is the case for most optical fibers, the NA may be equivalently expressed as

$$NA = n_{clad}\sqrt{2\Delta} \tag{1.4}$$

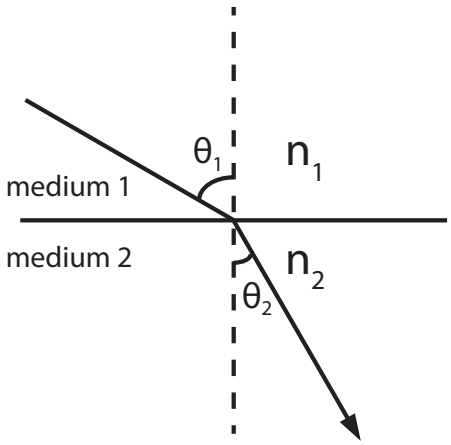


Figure 1.1: Snell's Law

Total internal reflection analysis of fiber until now is simplified and is not valid especially for single-mode optical fibers. In order to analyze propagation of beam inside fiber, beam should be considered as electromagnetic waves and Maxwell Equations should be used.

Spatial distribution of electromagnetic energy that propagates unaffected through a waveguide is called a *mode*. Number of modes inside fiber are determined by the refractive index configuration of the fiber and by proper structure fibers can be designed to guide single mode and eliminate the other modes. This single guided mode has a Gaussian intensity profile that has an amplitude maximum at the center of the core and diminishing quickly in the cladding. Spatial distribution of energy in multimode propagation have multiple maximums and minimums, however these modes' amplitude drops rapidly in the cladding of the fiber too. The diameter for obtaining single mode propagation at 1030 nm wavelength is generally less than 8 μm while multimode fibers at this wavelength generally have larger core diameter than 14 μm. The number of modes guided by an optical fiber is given with parameter V, normalized frequency of fiber;[1, 2]

$$V = \frac{2\pi R_{core} NA}{\lambda} = \frac{2\sqrt{2}\pi\sqrt{\Delta} R_{core} n_{clad}}{\lambda} \tag{1.5}$$

Here R_{core} is the radius of the core and λ is the wavelength. When $V < 2.405$ only fundamental mode is guided by the optical fiber , otherwise multiple modes can survive. Here we can define cutoff wavelength(λ_c) as the wavelength at $V = 2.405$ and the higher order modes can not propagate in fiber. The number of modes guided in the fiber increase with the increasing V. Fibers with small V are named as weakly guiding fibers. Using the equation 1.5 we can conclude that large core radius, large Δ, large NA and small λ_c increases the strength of guiding in optical fiber.

An optical beam's spatial size inside a single-mode optical fiber is usually given with the parameter of *mode field diameter*(MFD). Mode field diameter of a single mode fiber is dependent on the core diameter for most of the fibers. Optical fibers with smaller MFD are more prone to misalignment comparing to big MFD fibers. Different types of fibers show different mode field diameter characteristics. Mode field diameter in double clad fiber is wavelength dependent to achieve desired waveguiding. Polarization maintaining fibers(PMF) are similar to single mode fibers, but they have birefringence in their refractive index profile, so two polarization states propagate with different speeds inside these fibers. In order to achieve birefringence pattern in an optical fiber's refractive index, elliptical shaped cores can be used instead of circular shaped ones. More widely used method is to change mechanical properties of some regions inside cladding part by modifying the refractive index of the core due to the stress caused by this mechanically different regions called stress-applying members(SAM). The stress applied by SAM results in birefringence inside fiber.

In addition to these fibers, special types of fibers containing voids or air holes are developed and are widely used for many aaplications. Specialty of these fibers arised from the high contrast in refractive index between air and silica glass($\Delta \approx 33\%$). These voids inside fibers can be filled with special types of gases, metals or polymers in order to produce waveguides with unique properties for many applications. These fibers are also possible to be doped enabling them

to be used as gain fibers in fiber lasers and amplifiers.

1.2 Nonlinear Optics

The area of nonlinear optics is complex and comprises varieties of interesting applications. Despite being complex in nature, most of the effects in nonlinear optics can be simplified to be examined with just a few equations. Analysing the nonlinear optics is possible by starting with the Maxwells Equations for the propagation of light. In a dielectric media with no free charges and currents, Maxwell's Equations are as following:

$$\vec{\nabla} \cdot \mathbf{D}(\mathbf{r}, t) = 0 \tag{1.6}$$

$$\vec{\nabla} \cdot \mathbf{B}(\mathbf{r}, t) = 0 \tag{1.7}$$

$$\vec{\nabla} \times \mathbf{E}(\mathbf{r}, t) = -\frac{\partial \mathbf{B}(\mathbf{r}, t)}{\partial t} \tag{1.8}$$

$$\vec{\nabla} \times \mathbf{H}(\mathbf{r}, t) = \frac{\partial \mathbf{D}(\mathbf{r}, t)}{\partial t} \tag{1.9}$$

where $\mathbf{D}$ is the electric displacement and $\mathbf{E}$, $\mathbf{B}$ are the electric field and magnetic field respectively[3]. $\mathbf{H}$ and $\mathbf{D}$ are given as:

$$\mathbf{B}(\mathbf{r}, t) = \mu_0 \mathbf{H}(\mathbf{r}, t) \qquad \text{and} \qquad \mathbf{D}(\mathbf{r}, t) = \epsilon_0 \mathbf{E}(\mathbf{r}, t) + \mathbf{P}(\mathbf{r}, t) \tag{1.10}$$

where $\mathbf{P}$ is the polarization vector and ϵ_0, μ_0 are the permittivity and permeability of free space respectively. Equations 1.6-1.10 can be separated and, by taking $\vec{\nabla} \cdot \mathbf{E}(\mathbf{r}, t) = 0$, the expression below is attained

$$-\nabla^2 \mathbf{E}(\mathbf{r}, t) + \frac{1}{c^2} \frac{\partial^2 \mathbf{E}(\mathbf{r}, t)}{\partial t^2} = -\mu_0 \frac{\partial^2 \mathbf{P}(\mathbf{r}, t)}{\partial t^2} \tag{1.11}$$

where c is the speed of light in vacuum. The polarization is given by

$$\mathbf{P}(\mathbf{r}, t) = \epsilon_0 \chi \mathbf{E}(\mathbf{r}, t) \tag{1.12}$$

Here χ is the optical susceptibility. χ can be obtained iteratively by applying first order perturbation methods [4] and as a result the polarization can be given

as an addition of a linear term and succeeding nonlinear terms

$$\mathbf{P} = \mathbf{P}_l + \mathbf{P}_{nl} = \epsilon_0 \chi^{(1)} \cdot \mathbf{E} + \epsilon_0 \sum_{j>2} \chi^{(j)} \mathbf{E}^{(j)} \tag{1.13}$$

$\chi^{(j)}$ is usually complex and its imaginary parts gives the ratio of gain/loss. Dielectric function's linear part is then given by $\epsilon(w) = \epsilon_0(1+\chi^{(1)}) = n^2(w)$.Hence equation 1.11 can be written as

$$-\nabla^2 \mathbf{E}(\mathbf{r}, t) + \frac{n(w)^2}{c^2} \frac{\partial^2 \mathbf{E}(\mathbf{r}, t)}{\partial t^2} = -\frac{\partial^2 \mathbf{P}_{nl}(\mathbf{r}, t)}{\partial t^2} \tag{1.14}$$

Here we see that nonlinear polarization term governs the properties of the derived wave equation. When there is no nonlinear polarization term, $\mathbf{P}_{nl}$, the beam simply propagates as a free wave with speed $v = c/n$. Most of the nonlinear effects can be described using this equation and can be correlated to a given $\chi^{(j)}$-tensor. For instance, second harmonic generation can be described with the real part of $\chi^{(2)}$, similarly third harmonic generation with the real part of $\chi^{(3)}$ as well as self-phase modulation, four-wave mixing and self-focusing. The imaginary part of $\chi^{(3)}$ can be used to analyze Raman gain, two-photon absorption, etc. There are higher order processes but they are generally omitted due to weakness of their effect. Since amorphous SiO_2 has inversion symmetry, all the even orders of χ are wiped out in optical fibers and main contribution is coming from the $\chi^{(3)}$. Taking this into account, nonlinear polarization can be simplified as[3]:

$$\mathbf{P}_{nl}(\mathbf{r}, t) = \epsilon_0 \int \int \int_{-\infty}^{+\infty} \chi^{(3)}(t, t_1, t_2, t_3) \mathbf{E}(\mathbf{r}, t_1) \mathbf{E}(\mathbf{r}, t_2) \mathbf{E}(\mathbf{r}, t_3) dt_1 dt_2 dt_3 \tag{1.15}$$

$\chi^{(3)}(t, t_1, t_2, t_3)$ can be approximated by $\chi^{(3)}(t, t_1, t_2, t_3) = \chi^{(3)} R(t-t_1)\delta(t-t_2)\delta(t-t_3)$ where interaction between the vibrational modes of silica and the propagating light are taken into account using the functional form of $R(t)$ below

$$R(t) = (1 - f_R)\delta(t) + f_R h_R(t) \tag{1.16}$$

Here f_R is the fractional part of the response governed by Raman scattering and h_R is the Raman response function [3, 5, 6].

Considering the fibers, if we return to Equation 1.14 by neglecting the nonlinear terms, the equation can be solved via Fourier transformation by replacing $\frac{\partial^2}{\partial t^2}$ with $-w^2$

$$-\nabla^2 \mathbf{E}(\mathbf{r}, w) = -\frac{w^2}{c^2} n^2(w) \mathbf{E}(\mathbf{r}, w) \tag{1.17}$$

A superposition of plane waves is a solution to this equation and since the light must also be confined in the transverse dimension of the fiber, a linearly polarized solution must be of the form

$$\mathbf{E}(\mathbf{r}, w - w_0) = \hat{x} F(x, y) \cdot A(z, w - w_0) \cdot e^{-i(\beta_0 z - w_0 t)} \tag{1.18}$$

where F is the transverse field distribution, A is a slowly varying envelope, w_0 is a fast carrier frequency and β_0 is the wave-number for the central frequency. A is normalized such that $|A|^2$ gives the optical power. The product of the independent transverse and longitudinal parts leads to two conditional equations [3, 7]

$$(\frac{\partial^2}{\partial x^2} + \frac{\partial^2}{\partial y^2}) F(x, y) + n^2(w) \frac{w^2}{c^2} F(x, y) = \beta^2 F(x, y) \tag{1.19}$$

$$2i\beta_0 \frac{\partial}{\partial z} A(z, w) + 2\beta_0(\beta - \beta_0) A(z, w) = 0 \tag{1.20}$$

where the second derivative of the slowly varying envelope $A(z, w - w_0)$ has been neglected and the approximation $(\beta^2 - {\beta_0}^2) \sim 2\beta_0(\beta - \beta_0)$ has been used in deriving equation 1.20. Equation 1.19 is known as the scalar Helmholtz equation and it leads to the conditions for the guided modes and their field distribution $F(x, y)$ in the fiber. Propagation along the fiber is governed by equation 1.20 which will finally result in a nonlinear Schrödinger equation.

The scalar Helmholtz equation (equation 1.19) is an eigenvalue problem where β is an eigenvalue of the transverse field distribution $F(x, y)$. In absence of

nonlinear polarization, the solutions for $F(x, y)$ are superpositions of Bessel and Neumann functions and it can be shown that there are only confined modes when $k^2{n_1}^2 > \beta^2 > k^2{n_2}^2$ [8]. There may be several values of β fulfilling this condition in which case the fiber is multi-mode - meaning that more than one spatial field distribution is possible in the fiber. Single-mode operation prerequisity was given in the previous section by defining V parameter (Equation 1.5).

1.2.1 Nonlinear Schrödinger Equation

If Kerr-nonlinearity is taken into account int the equation 1.14, the weak nonlinear term $\epsilon_{NL} = \frac{3}{4}\chi^{(3)}|\mathbf{E}(\mathbf{r}, t|^2$ modifies the refractive index and it becomes

$$\tilde{n}^2(w) = \epsilon(w) = 1 + Re\left[\chi^{(1)}\right] + \frac{3}{4}\chi^{(3)}|\mathbf{E}(\mathbf{r}, t|^2 \tag{1.21}$$

change in $n(w)$ is minor and can be neglected, so

$$\tilde{n}^2(w) = (n(w) + \Delta n)^2 \sim n^2(w) + 2n(w)\Delta n \tag{1.22}$$

which makes solution of the equation 1.19 using first order perturbation methods. As a first step field distribution $F(x, y)$ and parameter β is obtained using $n^2(w)$. Then first correction to the β due to the term $2n\Delta n$ is done using the eigenfunctions of $F(x, y)$. To first order, the modal distribution is therefore unaffected while the propagation constant is changed to

$$\tilde{\beta}(w) = \beta(w) + \Delta\beta \tag{1.23}$$

We can use a Taylor expansion around the carrier frequency w_0 to obtain an unperturbed linear propagation constant approximation:

$$\beta(w) = \beta_0 + \beta_1(w - w_0) + \frac{1}{2}\beta_2(w - w_0)^2 + \frac{1}{6}\beta_3(w - w_0)^3 + \ldots... \tag{1.24}$$

where $\beta_i = \left.\frac{\partial^i \beta_L}{\partial w^i}\right|_{w_0}$

When propagation constant is put into use in equation 1.20 and an inverse fourier transform applied to obtain time domain equation, time dependent slowly varying envelope is obtained as following

$$\frac{\partial A}{\partial z} + \sum_{n=1} \beta_n \frac{i^{n-1}}{n!} \frac{\partial^n}{\partial t^n} A = i\Delta\beta A \tag{1.25}$$

For a given field distribution, $\Delta\beta$ is given by:

$$\Delta\beta = \frac{w_0 \int\int_{-\infty}^{+\infty} \Delta n |F(x,y)|^2 dxdy}{c \int\int_{-\infty}^{+\infty} |F(x,y)|^2 dxdy} \tag{1.26}$$

with

$$\Delta n = \frac{3}{8n} \mathrm{Re}\left[\chi^{(3)}\right] |E|^2 + i\left(\frac{1}{2n} \mathrm{Im}\left[\chi^{(1)}\right] + \frac{3}{8n} \mathrm{Im}\left[\chi^{(3)}\right] |E|^2\right) \tag{1.27}$$

Omitting the imaginary part of $\chi^{(j)}$ (absorption) Equation 1.26 simplifies considerably:

$$\Delta\beta = \frac{n_2 w_0}{c A_{eff}} |A|^2 \tag{1.28}$$

Here n_2 is the nonlinear refractive index and in silica it is $\sim 3 \cdot 10^{-20} (W \cdot m)^{-1}$ and A_{eff} is the effective mode area. The final result thus becomes

$$\frac{\partial A}{\partial z} + \sum_{n=1} \beta_n \frac{i^{n-1}}{n!} \frac{\partial^n}{\partial t^n} A = i\gamma |A|^2 A \tag{1.29}$$

here γ is the nonlinear parameter and given by $\gamma = \frac{n_2 w_0}{c A_{eff}}$. Equation 1.29 is important since it contains all the information about the basic effects optical pulses experience during propagation in single-mode fibers and it is named as the "Nonlinear Schrödinger Equation"[3].

1.2.2 Dispersion in Optical Fibers

When an electromagnetic wave propagates through a material, the group of atoms exposed to the wave become polarized and the resulting total polarization also radiates at the exact frequency of the incoming beam but with a delay with frequency dependence. Hence, different frequency components of the beam propagates with different speeds resulting in separation and spreading in time. It is called *dispersion*. The temporal dispersion may arise from a few different reasons in optical systems. One of them is subsequent absorption and emission process of frequencies which match to the atomic resonance continuously, causing the frequencies to be delayed. Another possibility for multi-mode beams is that due to spatial distribution they may disperse in time since different modes will expose to different refractive indexes. It is especially important for multi-mode fibers where higher order modes penetrate more into the cladding thereby propagate in lower refractive index medium. The other dispersion type is waveguide dispersion that occurs only in single mode fibers when the fundamental mode is not completely confined into the core of the fiber and leak into the cladding and experience lower refractive index. This leakage ratio is defined by the core diameter of the fiber and the refractive index difference between core and the cladding. Using this mechanism zero dispersion wavelength(ZDW) of the fiber can be altered and shifted from the zero dispersion wavelength of bulk silica which is around 1300 nm. This method is widely used for telecommunication fibers to be used in the low-loss window at 1550 nm by shifting the zero dispersion wavelength to this region as well as PCFs to be used in visible region.

The expansion of $\beta(w)$ in equation 1.24 includes all the dispersion types. (β_1)

,(β_2) and (β_3) give the group velocity, group velocity dispersion (GVD) and third-order dispersion (TOD) respectively. Analyzing this system becomes easier if we move to a new coordinate system by defining a retarded frame with $T = t - z/v_{group} = t - \beta_1 z$. Equation 1.25 then simplifies to

$$\frac{\partial A}{\partial z} + \sum_{n=2} \beta_n \frac{i^{n-1}}{n!} \frac{\partial^n}{\partial T^n} A = i\gamma |A|^2 A \tag{1.30}$$

The effect of group velocity dispersion, β_2, becomes more clear when we omit higher order dispersion terms and nonlinearities ($\gamma = 0$). Taking the fourier transform of the equation 1.30 gives us;

$$\frac{\partial A(z,w)}{\partial z} - \frac{i}{2}\beta_2 w^2 A(z,w) = 0 \tag{1.31}$$

which has a solution of

$$A(z,w) = A(0,w) exp(\frac{i}{2}\beta_2 w^2 z) \tag{1.32}$$

This solution depicts that β_2 does not change pulse spectrum but a frequency dependent phase is applied to pulse. When the inverse Fourier transform is applied to the acquired result, time dependent pulse envelope becomes

$$A(z,T) = \frac{1}{2\pi} \int_{-\infty}^{+\infty} A(0,w) \exp(\frac{i}{2}\beta_2 w^2 z - iwt) dw \tag{1.33}$$

If the input beam is a Gaussian beam as $A(0,T) = \exp(-\Gamma_0 t^2) \cdot \exp(iw_0 T)$, the integral can be solved as

$$A(z,T) = \exp(i[\phi_0 + w_0 T + \frac{2\Gamma_0^2 \beta_2 z T^2}{1 + (2\Gamma_0 \beta_2 z)^2}]) \cdot \exp(-\frac{\Gamma_0 T^2}{1 + (2\Gamma_0 \beta_2 z)^2}) \tag{1.34}$$

According to this result, pulse is temporally broadened since it attains a time dependent phase. The time dependence of the phase is quadratic which results that the instantaneous frequency for carrier is chirped linearly $w(T) = \frac{\partial \phi}{\partial T}$. Negative or positive chirp is determined by the sign of β_2. When an unchirped pulse acquires a linear chirp over the entire pulse, leading edge of the fiber contains red-shifted components while the trailing edge contains blue-shifted component. A simulated 150 fs Gaussian pulse after propagation through a 1.3 meter of a fiber with normal dispersion is given in Figure 1.2. Here higher order dispersion terms and nonlinearity is neglected to make the effect of dispersion more clear. It can be seen that initially unchirped pulse obtains a chirp all over the pulse and the leading edge of the pulse is red-shifted while the trailing edge is blue-shifted.

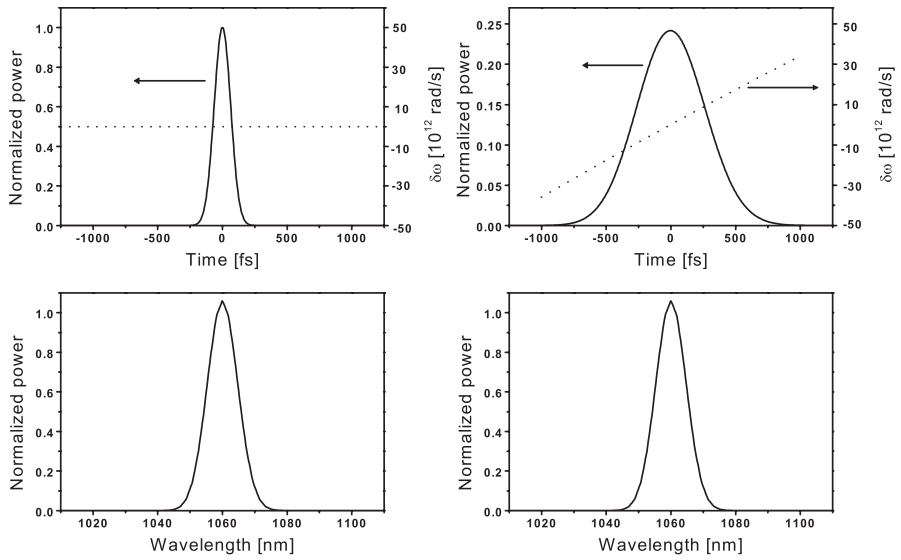


Figure 1.2: Temporal (up) and spectral (down) profile of a 150 fs Gaussian pulse before (left) and after (right) propagating through a 1.3 m of a 5 μm single-mode fiber. Here nonlinearity and higher order terms of dispersion are neglected in order to show the effect of group velocity dispersion. In the graph, dotted lines show the change in instantaneous frequency. The group velocity disersion based linear chirp is visible in the right figure. The spectral components that are faster and slower are determined by the sign of β_2. The bottom row illustrates the unchanged spectrum by the effect of pure dispersion.

Unless the analyzed pulse is ultrashort (femtoseconds) higher order terms are usually neglected. For ultrashort pulses a decent analysis necessitates the inclusion of third, even fourth order terms to be taken into account in equation 1.30. Similar to β_2, higher order dispersion terms do not effect the spectrum but changes the shape of the temporal profile significantly [3]. Practically second order dispersion is possible to be compensated using grating pair or prisms so they don't constitute a problem for the compressibility of the pulses. On the other hand, higher order terms are not that easy to compensate and usually results in decrease of the pulse quality[9].

1.2.3 Self-Phase Modulation in Fibers

Clarification of the importance of nonlinear term in Equation 1.30 is best possible by removing the dispersion term. The equation then becomes

$$\frac{\partial A}{\partial z} = i\gamma |A|^2 A \tag{1.35}$$

which can be solved by

$$A(z,T) = A(0,T)\exp(i\gamma\,|A(z,T)|^2 z) \tag{1.36}$$

Equation 1.36 shows that the nonlinearity does not change the pulse shape but merely imposes a nonlinear phase which depends on the temporal profile of the pulse itself - hence the effect is named self phase modulation (SPM). Figure 1.3 shows a simulated 150 fs Gaussian pulse after propagation through 30 cm of a 5 μm single-mode fiber when dispersion is neglected. The chirp is seen to be linear at the center and nonlinear at the wings of the pulse. The central chirp is similar to the chirp caused by normal group velocity dispersion (see figure 1.2) with red frequency components being shifted to the leading edge of the pulse and blue components to the trailing edge. The joint action of normal dispersion and SPM is therefore to rapidly chirp and broaden the pulse. However, negative GVD can in

some cases balance the linear part of the SPM chirp and the pulse can propagate without changing its form in time and frequency. This type of solution is called a fundamental soliton[3]. Physically, the negative dispersion shifts the blue spectral components to the leading edge of the pulse where they get red-shifted back again by SPM. Fundamental solitons can propagate through thousands of kilometers of fiber without degrading and have been used successfully for data transmission in telecommunication lines[10]. If the dispersion is not exactly balanced by SPM, the pulse will breathe in the sense that it broadens and contracts periodically in time and frequency as it propagates along the fiber. This type of solution is called a higher order soliton and fission of such solitons is fundamental for the understanding of super continuum generation in optical fibers.

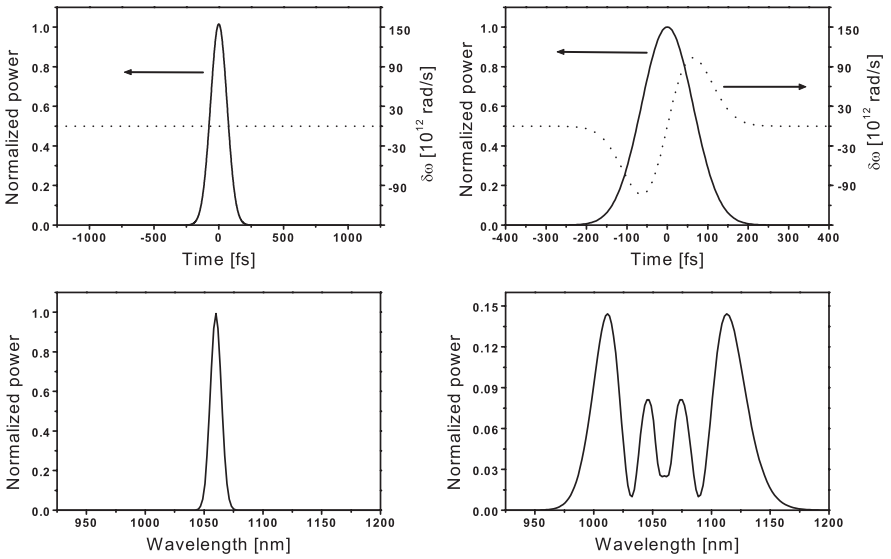


Figure 1.3: Temporal (up) and spectral (down) profile of a 150 fs Gaussian pulse before (left) and after (right) propagating through a 30 cm of a single-mode fiber with core diameter of 5 μm. Here dispersion is neglected in order to show the effect of nonlinearity. In the graph, dotted lines show the change in instantaneous frequency. During propagation the central part of the pulse becomes linearly chirped while the wings of the pulse obtains higher order phase. The bottom row illustrates the spectral alteration in the pulse and it is visible that new frequency components are created due to nonlinearity.

In order to fully analyze an ultrashort pulse, higher order terms should also be included in modeling. Particularly, Raman scattering have a significant effect on pulse dynamics, but further analyze requires cross-phase modulation, self steepening and four-wave mixing effects to be included as well. In order to derive extended version of Nonlinear Schrödinger Equation, all elements of $\chi^{(3)}$ should be taken into account.

1.3 Rare-Earth Doped Fibers

Glass properties can be altered by doping rare-earth ions and the promising possibilities that these doped glasses offered has attracted attention of researchers for over 40 years. In the beginning of eighties, rare earth ions started to be used in optical fibers and since then fiber lasers and fiber amplifiers became a hot field for investigation. Rare earth ions dissolve in fiber host material, which is glass, and ionize from third degree by losing two outer 6s orbital electrons and an inner 4f electron[11]. This partially filled 4f orbital determines the optical properties of the fiber. 5p and 5s orbital electrons shield the 4f electrons from the field of the host glass material, leading to the gain bandwidth and wavelength of the laser becomes nearly independent of the host. Most widely used materials to dope fibers as of today are Ytterbium(Yb), Erbium(Er), Thulium(Tm) and Neodynium(Nd). In this thesis study, all the lasers are done using Yb-doped fibers.

Yb transitions for optical region occurs between the $F_{5/2}$ and the $F_{7/2}$ levels. The Stark Splitting caused by the field of the silica host is shown in Figure 1.4. Here homogenous broadening alter the discrete energy levels into energy bands [11]. Significant property here is that out of band transitions such as excited state absorption are not possible since these two bands are isolated in terms of energy levels. The energy difference between two ground states is approximately 976 nm photon energy and this enables the possibility of using widely used and commercially available telecom pump laser diodes to pump such fibers. After an electron is excited using 976 nm pump laser to the $F_{5/2}$ level, the most probable scenario is to return to the first Stark level of $F_{7/2}$ band and emitting a photon

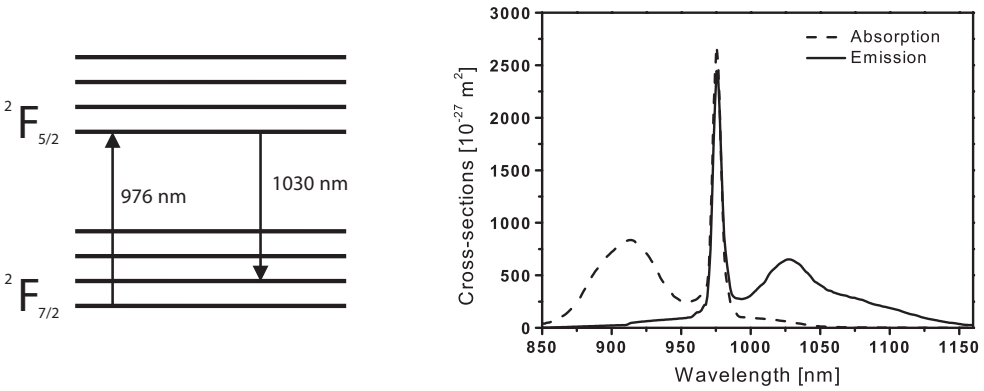


Figure 1.4: Pumping/emission band schematic (left) and absorption/emission spectra (right) of Ytterbium-doped fiber

corresponding to energy level $\lambda = 1030$ nm. Similarly excited electrons can return to higher energy states in $F_{7/2}$ band and emitting photons at different energy levels spanning all 976 nm to 1200 nm region. Probabilities of this emission spectrum as cross-section of absorption and emission as a function of wavelength is given in Figure 1.4. Upper state lifetime for this process is approximately 900 μs which is directly linked to spontaneous emission. Since the beam is confined in the fiber in a very limited area, these spontaneously emitted photons can be guided in the fiber and may even be amplified. This phenomena is called amplified spontaneous emission (ASE) and constitutes a serious challenge when one wants to extract high energy and high powers out of a fiber amplifier.

1.4 Photonic Crystal Fibers

Applications of optical fibers were mostly dominated by the telecommunication applications beginning from the early 90's. By the developments in the research activities of optical fibers, it was understood that optical fibers could be much more than just data transmitters and can also be used as sensors, nonlinear

wavelength converters and even as active medium for lasers. Erbium-doped fiber lasers were the breakthrough for fibers to be used as lasers in addition to helping them to dominate telecommunication field. Another breakthrough for optical fibers took place when Russell proposed a new type of fiber which can guide the light not by total internal reflection mechanism, but on a structure that is causing a bandgap effect similar to semiconductors[12]. Practically bandgap structure was formed by making defects in silica such that these defects are not allowing the beam to propagate through them and confine the light just to the core of the fiber[13]. Mathematical analysis of this guiding scheme is given in [14], still it is easier to illustrate it by the schematic shown in Figure 1.5.

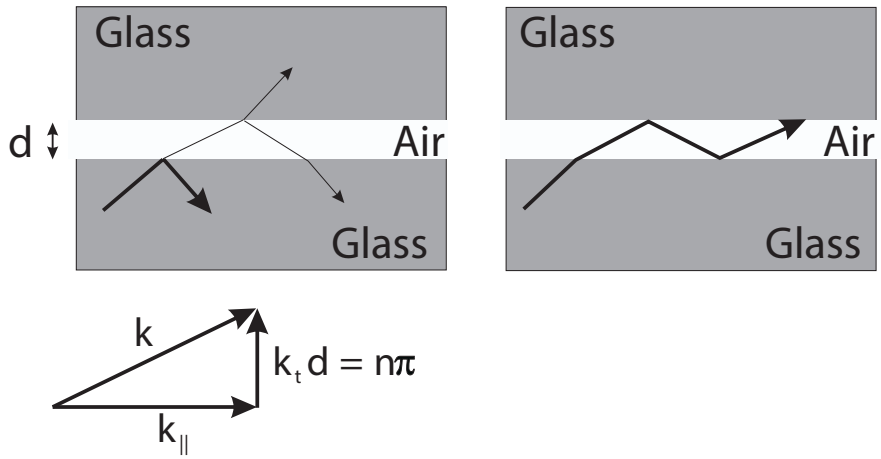


Figure 1.5: When the beam encounters an air defect in silica, it is transmitted or reflected depending on the incidence angle. In the case of the product of the transverse wavevector and the thickness of the defect is an odd multiple of π, the light is resonantly guided in the waveguide.

Here an optical beam shown with ray illustration is propagating through a silica slab that has a defect filled with air and has a thickness of d. According to Snell's Law, ray will be reflected or transmitted at the air/silica interface. However, differently from classical optical fibers, if the wavelength of the propagating light matches the size of the defect, a resonant state arises and the light escapes to the defect. For a definite incidence angle, some wavelengths matching this condition

propagate through the defect and will quit from the silica slab. In the case of the defect is made as small as the wavelength of the beam, no resonances will occur in silica and all the wavelengths will be maintained in the silica. By forming this sized defects around the core of the fiber, it is possible to confine all the light into the core and this phenomenon is the main idea behind photonic bandgap fibers (PBG).

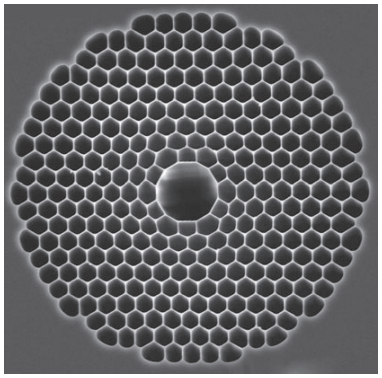


Figure 1.6: Photonic bandgap fiber SEM image. The beam is trapped in the core part (diameter is around 9 μm) that is filled with air and surrounded by anti-resonant structures that prevents the light to escape.

Figure 1.6 shows a cross section of a PBG fiber[15]. Core part of the fiber is filled with air and it is encircled by a structure formed by air holes running along all fiber length. Transverse propagation is not possible due to the non-resonant nature of the air holes and the silica walls supporting the structure. It is also possible to design single-mode fibers such that the higher order modes will have resonances around the band structure and vanish by propagating in the air defects. Due to difficulties in manufacturing PBGs with air-filled-core, first bandgap structured fibers are produced with solid silica core [13]. This type of fiber is named as photonic crystal fibers(PCF). Even though the guiding mechanism is the same as PBGs, for easier illustration of the mechanism it is often thought like total internal reflection with cladding index is defined as the average index of silica/air structure. Similar to standard fibers, it is possible to define a V parameter for PCFs to determine the number of supported modes.

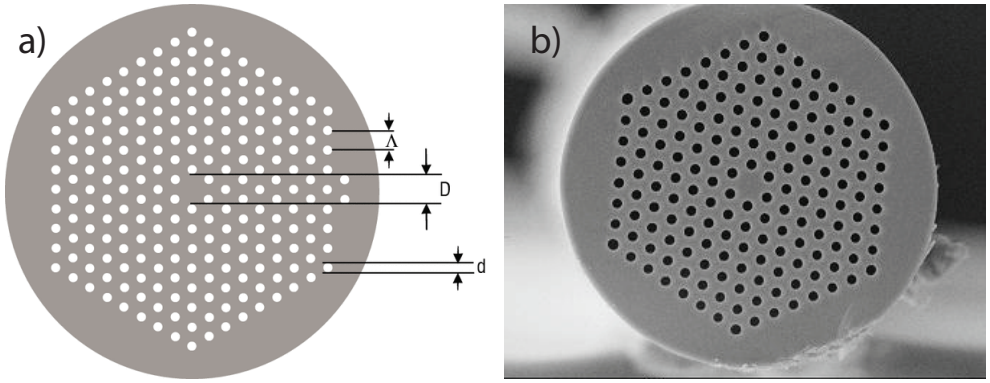


Figure 1.7: a) Schematic for a PCF. Here solid core, with a diameter of D, constitutes a defect in a regular array of air holes. The size of the air holes (given with d), and the distance between them (given with Λ are vital parameters and should be preserved throughout the fiber for the guiding to be achieved. b) SEM image of a realized PCF structure

Figure 1.7a shows a schematic for a PCF where the core is formed by an unstructured area in the middle of an array of air filled holes of diameter d. The distance between air holes is called *pitch* and given with Λ. In Figure 1.7b, an SEM image of such kind of PCF is given. Most important difference between a standard fiber and a PCF is that it is possible to guide a beam completely single mode in PCF since the cladding part of it is intensely wavelength dependent. In standard optical fibers, for a given NA and core diameter, cladding part is wavelength independent and fiber is single-mode only above a certain threshold of wavelength (equation 1.5). Reducing the NA provides single mode operation at a cost of making it difficult to couple the light into the fiber. In PCFs, shorter wavelengths are constrained more into the core while longer wavelengths spread and are exposed to lower refractive index in the cladding. This causes a wavelength dependence in V parameter and makes it possible to maintain V parameter lower than single-mode propagation cut-off for all wavelengths. It is shown that a ratio of $d/\Lambda > 0.4$ provides this situation[16, 17]. Moreover, the higher index difference between the core and the cladding part enables easier and efficient light coupling into smaller cores since NA values as high as 0.55 can be obtained in PCFs.

PCF's another advantage is that they have a dispersion profile that can be customized. Parameters d and Λ can be selected such that zero dispersion wavelength of waveguide can be shifted to the visible region by adding dispersion. Using this fact, Hermann et al. demonstrated supercontinuum generation using Ti:Sapphire oscillators by shifting the zero dispersion wavelength of PCF to 800 nm where sub-100 fs pulses are possible to be achieved by these lasers[18]. Since there is no dispersion at this wavelength, the pulses maintained their pulse duration and revealed a vast nonlinear response. It is also shown that the PCFs with higher core areas are also achievable. Similar to standard fibers, it is possible to get higher core areas by reducing NA while still preserving single-mode operation. Especially for high power applications, PCFs with core diameters as big as 60 μm are realized. In these fibers nonlinear effects confine light into the low NA core part in a single-mode fashion while the outer part of air holes forms a cladding for the pump light to be propagated by its relatively high NA of around 0.6. Here high NA provides the possibility of using cheaper and more powerful multi-mode pump laser diodes and big intersection between the pump region and the core region ensures efficient pump absorption in strongly Yb-doped core. This leads to very efficient amplification and energy storage in the large area core.

1.5 Fiber Lasers

The early lasers, in a vast majority, had free propagating wave in the gain and other parts of the cavity. The main limitation of the laser amplification is the volume of the pump that can be applied. The nonlinear interaction is also limited by the Rayleigh range which is given by ρ_0. One of the most efficient way of increasing interaction length and have a long gain media is to confine the beam inside a waveguide and use this media as gain and nonlinear interaction media by proper modification. An optical fiber is ideal medium for such purposes since little loss (as small as a few dB/km) and high beam confinement (microns) is possible. Another significant advantage of using optical fibers as gain media is that, using the proper combination such as negative dispersion and positive self-phase modulation enables forming and maintaining soliton waves. Using similar

approaches, in the last 20 years, such doped fibers have been used to build fiber laser oscillators and amplifiers which are compact, turn-key commercial systems which can generate watts of average powers, micro-joule pulse energies and pulse durations less than 100 fs.

Since fibers are made of glass, all the rare earth ions to dope glass lasers can be used to dope fibers too. Biggest advantage of such a gain medium is that it can have extraordinarily long interaction length. First demonstration of such a fiber is done by Duling[19, 20]. Since then, rare earth doped fiber lasers are in use in ultrafast pulses area to generate pulses less than 100 fs long by using passive mode-lock mechanism. Most common mediums used in fiber lasers are ytterbium (Yb^{3+}), erbium((Er^{3+}), neodymium(Nd^{3+}), thulium((Tm^{3+}), praseodymium((Pr^{3+}). Depending on the material, the output wavelength of laser varies, for instance Yb-doped fiber lasers operate around 1030 nm while Er-doped lasers operate at 1550 nm. In some cases combinations of these materials can be used in order to increase absorption and consequently emission rate of fiber lasers as in the case of Yb-Er co-doped fibers. When Erbium is co-doped with Yb, absorption band of fiber extends beyond 1000 nm and the emission caused by Yb dopant can be used to pump Er ions. High output powers and gain ratios can be achieved using diode laser pumped compact fiber lasers since they do not need any bulk optic components such as mirrors, prisms, gratings or saturable absorber devices or materials. Ideal system for a fiber laser is to be an all-fiber configuration and by the advances in fiber optic device manufacturing techniques, nearly all components needed for laser amplification, coupling, dispersion compensation and other purposes to build laser started to be realized suitable to all-fiber designs.

Comparing to most commonly used lasers like solid-state and gas lasers, fiber lasers have a distinct advantage in terms of surface to volume ratio which enables more efficient cooling. In addition, single mode operation possibility of optical fibers give an advantage over other methods for mode-locking as follows:

- High efficiency in wavelength conversion from pump to the signal. For example, ytterbium and erbium doped fibers are quasi-three level systems and

high confinement of the pump inside fiber leads to effective up-conversion from the ground state to higher energy states.

- Minimized non-radiative energy transfers between ions in the upper energy states of laser which causes energy loss. This kind of transition inside silica is highly undesired due to their excessive phonon energies. In case of such phonons' existence inside silica, dopants with three valance electrons do not mix properly inside the silica matrix which have four valance electrons and cause to arrange vigorously interactive groups of atoms at high concentrations[21]. Since laser and pump modes are confined inside optical fiber, gain dopants are distributed all along the fiber with lower concentration still maintaining total efficiency and eliminating the undesired interactions mentioned.

- Practically available pump diode lasers. Laser diodes readily developed at 915, 976 and 1480 nm wavelengths for telecommunications purpose are suitable to pump Ytterbium and Erbium doped fibers leading to efficient amplification. Even multimode lasers can be used to pump four-level systems such as neodymium-doped fibers, leading to higher power pumps and consequently higher power outputs [22]. For multimode diodes to be used as pump source, fibers should be designed to guide light in cladding.

- Despite the low nonlinear index of silica($(\bar{n_2} = 3 \cdot 10^{-16}\text{cm}^2/\text{W})$), self-phase modulation can be maximized using high confinement and long lengths of propagation.

One shortcoming of fiber lasers is that producible pulse energy can be limited by the confinement inside fiber. In solid-state lasers this limitation could be overcome by expanding the laser beam. A few of the most important techniques developed to mode lock lasers are:

1. nonlinear polarization rotation[23]
2. nonlinear loop mirrors[24]
3. saturable absorber mirror based mode locking[25]

In this thesis study, most of the lasers built were passively mode-locked lasers using the nonlinear polarization rotation method. Thus, in the next section, we will examine this method briefly.

1.6 Mode-Locking through Polarization Rotation

In addition to self-phase modulation, the polarization state of the laser beam inside fiber is affected by nonlinear effects and these effects can be used to mode lock fiber lasers. In order to analyze this, we should start by assuming a pulse that have an arbitrary polarization with complex amplitudes given with $\tilde{\mathcal{E}}_x(t)$ and $\tilde{\mathcal{E}}_y(t)$. We can define the unit vectors for principal axis as $\hat{x}$ and $\hat{y}$. Using these vectors, pulse can be defined as;

$$\mathbf{E} = \frac{1}{2}(\hat{x}\tilde{\mathcal{E}}_{0x}(t) + \hat{y}\tilde{\mathcal{E}}_{0y}(t))e^{i(w_l t - k_l z)} \tag{1.37}$$

During the propagation of a field through a material that has a non-zero nonlinear index, coupling between two polarization states occur. This coupling results in a nonlinear index change that can be calculated along $\hat{x}$ and $\hat{y}$ using the principles in [3] as;

$$\begin{aligned}\Delta n_{nl,x} &= n_2\left[\left|\tilde{\mathcal{E}_{0x}}\right|^2 + \frac{2}{3}\left|\tilde{\mathcal{E}_{0y}}\right|^2\right] \\ \Delta n_{nl,y} &= n_2\left[\left|\tilde{\mathcal{E}_{0y}}\right|^2 + \frac{2}{3}\left|\tilde{\mathcal{E}_{0x}}\right|^2\right]\end{aligned} \tag{1.38}$$

The birefringence induced by coupling of two polarizations leads to phase modification and transition between two axis of the field vector in a medium with a thickness of d_m. This phase change can be given as:

$$\Delta\Phi(t) = \frac{2\pi}{\lambda_l}(\Delta n_{nl,x} - \Delta n_{nl,y}) = \frac{2\pi n_2 d_m}{3\lambda_l}\left[\left|\tilde{\mathcal{E}}_{0x}(t)\right|^2 - \left|\tilde{\mathcal{E}}_{0y}(t)\right|^2\right] \tag{1.39}$$

As it can be seen from the equation, shift in phase is depending on time. Using in combination with another effect, it can be used as an intensity dependent loss element. In order to illustrate such an effect let us assume we have such a birefringent component and a linear polarizer. If we begin with the incident pulse as $E_0\cos(wt)$ which is linearly polarized and have polarization components as:

$$\begin{aligned}\mathcal{E}_{0x}(t) &= \mathcal{E}_0(t)\cos\alpha \\ \mathcal{E}_{0y}(t) &= \mathcal{E}_0(t)\sin\alpha\end{aligned} \tag{1.40}$$

When the polarizer pass direction is set to $\alpha + 90°$, no transmission occurs for the low-intensity beam $\Delta\Phi \approx 0$. If we neglect the common phase, at the output of nonlinear element the field components are:

$$\begin{aligned}\mathcal{E}'_x(t) &= [\mathcal{E}_0(t)\cos\alpha]\cos(w_l t) \\ \mathcal{E}'_y(t) &= [\mathcal{E}_0(t)\sin\alpha]\cos[(w_l t) + \Delta\Phi(t)]\end{aligned} \tag{1.41}$$

After this, the pulse goes into a linear polarizer and the output of the resulting beam is the superposition of the components from $\mathcal{E}'_x(t)$ and $\mathcal{E}'_y(t)$ along the polarizer's path direction;

$$\mathcal{E}_{out}(t) = \mathcal{E}_0(t)\cos\alpha\sin\alpha\left\{\cos(w_l t) + \cos[w_l t + \Delta\Phi(t)]\right\} \tag{1.42}$$

Intensity of the output $I_{out}(t) = \langle\mathcal{E}^2(t)\rangle$ is

$$I_{out}(t) = I_{in}(t)\frac{1}{2}[1 - \cos\Delta\Phi(t)]\sin^2(2\alpha) \tag{1.43}$$

If the input pulse is in the form of a Gaussian as $I_{in} = I_0 \exp[2(t/\tau_G)^2]$ and the nonlinear element's parameters are defined such that the pulse center has the phase difference as follows;

$$\Delta\Phi(t=0) = \frac{2\pi n_2 d_m}{3\lambda_l} \mathcal{E}_0^2(t=0) \left(\sin^2\alpha - \cos^2\alpha\right) = \pi. \tag{1.44}$$

under these circumstances the transmitted pulse is:

$$I_{out}(t) = \frac{1}{2} I_{in}(t) \left\{1 - \cos[\pi e^{-2(t/\tau_G)^2}]\right\} \tag{1.45}$$

When the nonlinear element acts as a half-wave plate via rotating the polarization by 90°, the transmission is maximum. Considering the parameters we have assumed, this condition occurs just for the center of the pulse (t=0). Away from the pulse center phase shift $\Delta\Phi$ gets smaller producing an elliptically polarized beam and the output reduces as a result. For the wings of the pulse, transmission eventually reaches to zero. Consequently a sequence ensuring such a condition provides a transmission profile dependent on intensity similar to fast saturable absorber.

Using this principle, in combination with polarizers nonlinear polarization rotation can be used to mode-lock a laser. When nonlinear polarization rotation is used inside a fiber laser, an intensity dependent polarization state occurs across the pulse. This polarization profile is then converted into intensity-dependent loss/transmission profile by inserting a linear polarizer at the output of the birefringent element leading to transmission for the high intensity parts(central part of the pulse assuming it has a Gaussian distribution) and attenuation for the low-intensity parts(pulse wings). Using this mechanism, pulses as short as 28 fs could be achieved[26]. For the mentioned nonlinear element, a standard fiber is adequate. Standard fiber has usually low birefringence and the birefringence level is determined by the following parameter:

$$B = \frac{|k_x - k_y|}{2\pi/\lambda_l} = |n_x - n_y| \tag{1.46}$$

Here n_x and n_y are the effective refractive indices for two orthogonal polarization states. For a given B, two modes (field components along $\hat{x}$ and $\hat{y}$) exchange optical power periodically with a period called "beat length" and shown with L_B according to [27] :

$$L_B = \frac{\lambda_l}{B} \tag{1.47}$$

The axis with higher mode index is named as the slow axis. The beat length for a conventional single mode optical fiber varies between 2 to 10 m at 1.55 μm wavelength[28]. Winful [29] has shown that nonlinear polarization effects are observable even in low powers in weakly birefringent fibers(in contrary to polarization maintaining fibers). In a usual fiber cavity in ring design, firstly a polarization controller generates an elliptical polarization. In this polarization state principal axis have an angle θ with the slow axis for the succeeding fiber part. As shown before, the resulting phase difference between two orthogonal states of polarization is dependent on the intensity of the pulse and the length of propagation d. It can be attuned such that the polarization becomes linear after a certain propagation distance d_m. A polarizer can be used to attenuate lower intensities more, comparing to higher intensities as illustrated in Figure 1.8

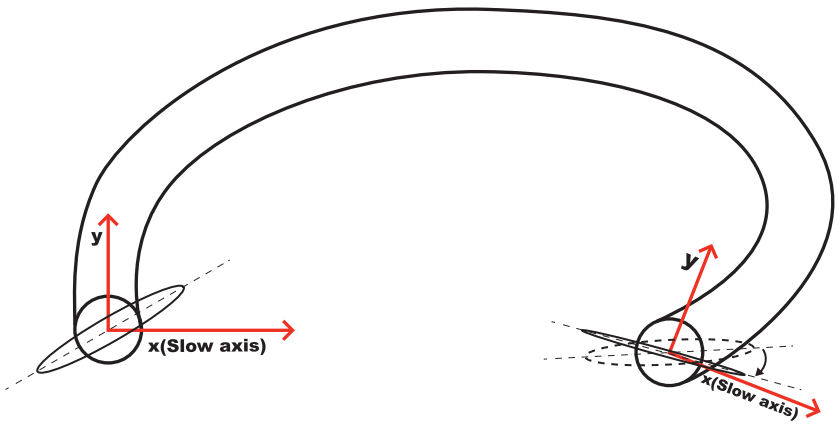


Figure 1.8: Nonlinear polarization rotation mechanism inside optical fiber

Since we have already obtained the fundamental equations associated with

nonlinear polarization rotation, to illustrate a fiber laser, we need to observe the progress of two polarization states. To do this a column vector can be used for the electric field at a particular point in the cavity

$$\begin{pmatrix} \tilde{\mathcal{E}}_x \\ \tilde{\mathcal{E}}_y \end{pmatrix} \tag{1.48}$$

and 2×2 matrices (M) for the resonator elements[30, 31]. Thus, a fiber of length L can be analyzed in two parts; a linear propagation problem and nonlinear phase modulation. The matrix that will be obtained according to this approach is a product of two matrices. Accordingly resulting vector is given as:

$$\begin{aligned} \begin{pmatrix} \tilde{\mathcal{E}}_x(L) \\ \tilde{\mathcal{E}}_y(L) \end{pmatrix} &= \begin{pmatrix} e^{-i\Phi_{NL,x}} & 0 \\ 0 & e^{-i\Phi_{NL,y}} \end{pmatrix} \cdot \begin{pmatrix} e^{-ik_xL} & 0 \\ 0 & e^{-ik_yL} \end{pmatrix} \cdot \begin{pmatrix} \tilde{\mathcal{E}}_x(0) \\ \tilde{\mathcal{E}}_y(0) \end{pmatrix} \\ &= \begin{pmatrix} e^{-i\Phi_x} & 0 \\ 0 & e^{-i\Phi_y} \end{pmatrix} \cdot \begin{pmatrix} \tilde{\mathcal{E}}_x(0) \\ \tilde{\mathcal{E}}_y(0) \end{pmatrix} \end{aligned} \tag{1.49}$$

where

$$\Phi_{x,y} = \frac{2\pi n_2 L}{\lambda_l} \left[\left| \tilde{\mathcal{E}}_{x,y} \right|^2 + \frac{2}{3} \left| \tilde{\mathcal{E}}_{y,x} \right|^2 \right] - \frac{2\pi n_{x,y} L}{\lambda_l} \tag{1.50}$$

Same approximations that were made for the nonlinear phase are also used here. Constants for linear propagation are $k_{x,y} = w_l n_{x,y}/c$. This analysis is especially useful since the Jones calculus can be used for the already known matrices of components like polarizers and wave plates.

The other parameters like saturable absorption, gain, mirrors, etc. do not depend on the polarization, so they do not need to be included. If we define a transfer function to include all the elements mentioned, a transfer matrix can be defined as:

$$(M) = T \begin{pmatrix} 1 & 0 \\ 0 & 1 \end{pmatrix} \tag{1.51}$$

Gain and loss rates in fiber lasers are usually high. The laser operates under high saturation condition while pulses are much shorter than the relaxation period of lasing energy transfer. The gain transition usually enough wide for the modulation of phase since the saturation is negligible. Hence, the T in the transfer matrix that gives gain have only real part and can be acquired as

$$T_g = \left[\frac{e^{W_0(t)/W_s}}{e^{-a} - 1 + e^{W_0(t)/W_s}} \right]^{1/2} \tag{1.52}$$

Another possible way is to take fiber laser as a continuous medium, which results in coupled differential equations for the components $\tilde{\mathcal{E}}_x$ and $\tilde{\mathcal{E}}_y$.

1.7 Fiber Amplifiers

Similar to fiber lasers, fiber amplifiers also use stimulated emission to amplify incident light. Actually a fiber amplifier's only difference from a fiber laser is that it has no feedback mechanism. Main element of amplifier is optical gain, and to obtain gain, amplifier should be pumped by a source to achieve inversion population. Relying on the material used to dope the fiber, amplifier pumping schemes can be classified as three-level or four-level systems[32, 33, 34]. Two types of pumping methods are illustrated in Figure 1.9. For both methods, photons are absorbed by the dopants and causing them to reach higher state of energy, and then excited state dopants relax immediately to slightly lower state of energy without any radiation. Using stimulated emission mechanism this stored energy amplifies the incident signal. Three-level and four-level pumping schemes' key difference is due to the dopant energy states succeeding the stimulated emission, i.e. the dopant pumped in three-level scheme returns to the ground state while the dopant in four-level scheme stays in an excited energy state. Characteristics of the amplifier change considerably according to pumping scheme. Ytterbium and erbium doped fiber amplifiers exhibit three-level pumping scheme.

To understand signal amplification, pumping details are not significant. Only thing that should be known is that pumping generates population inversion, between ground state and the excited state, necessary to provide optical gain

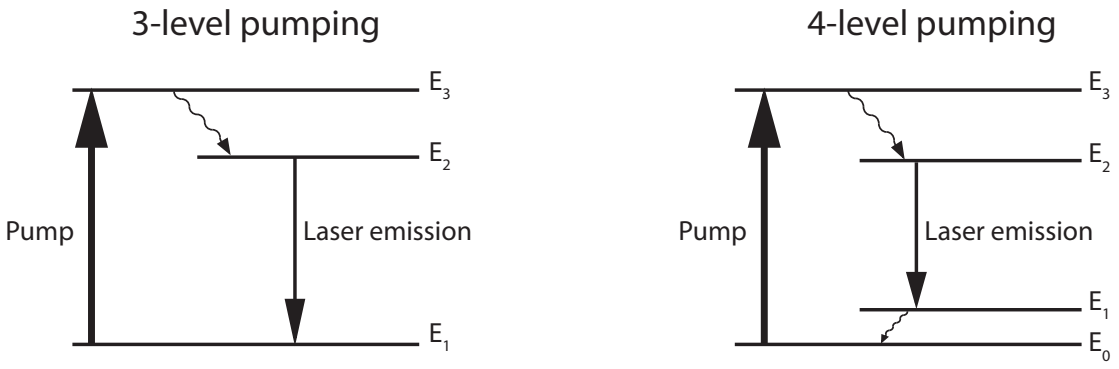


Figure 1.9: Three-level and four-level pumping schemes for fiber amplifiers. Wavy arrows indicate nonradiative fast transitions

$g = \sigma(N_1 - N_2)$. Here σ is cross section for transition and N_1 and N_2 are atomic densities for corresponding energy states. Using the suitable rate equations [32, 33, 34], the gain coefficient g can be obtained for three-level and four-level pumping schemes. For a gain medium that is broadened homogeneously, gain coefficient can be given as:

$$g(w) = \frac{g_0}{1 + (w - w_a)^2 T_2^2 + P/P_s} \tag{1.53}$$

Here g_0 is peak value, w is incident signal frequency, w_a is the frequency of the atomic transition, and P is the optical power for continuous-wave that is being amplified. Dopant parameters such as cross section of transition σ and fluorescence time T_1 have direct effect on saturation power P_s. T_2 parameter in equation 1.53 is named *dipole relaxation time* and for fiber amplifiers it is usually subtle (~0.1 ps). Depending on the dopant type, T_1 may be between $0.1\mu s$ and 10 ms. In order to determine important characteristics such as amplification factor, gain bandwidth and output saturation power, Equation 1.53 can be used. Assuming $P/P_s \ll 1$ all through the amplifier, fiber amplifier works in an unsaturated regime during amplification.

By omitting the term P/P_s in Equation 1.53, the gain coefficient simplifies to

$$g(w) = \frac{g_0}{1 + (w - w_a)^2 T_2^2} \tag{1.54}$$

As the equation indicates, when the frequency of the signal w and the frequency of the transition w_a match, gain becomes maximum. Gain profile is ruled by a Lorentzian function shape which is usual for homogeneously broadened systems [32, 33, 34]. However actual gain profile of fiber amplifiers may diverge significantly from Lorentzian profile. Definition of "gain bandwidth" is usually done by calculating full width at half maximum(FWHM) value of the spectrum of the gain $g(w)$ and it is given for a Lorentzian profile as;

$$\Delta v_g = \frac{\Delta w_g}{2\pi} = \frac{1}{\pi T_2} \tag{1.55}$$

For example, $\Delta v_g \approx 3$ THz when $T_2 = 0.1$ ps. For optical communication systems and ultrashort pulse amplification systems, larger bandwidth amplifiers are desired.

Here we will give a brief explanation of ultrashort pulse amplification inside optical fiber. Since fiber amplifiers have large bandwidths, when they are used as the gain media, no distortion occurs during amplification of ultrashort pulses. Certainly, EDFA's one of the primary uses just after its development was the amplification of ultrashort pulses. In this part, we will generate a more comprehensive Nonlinear Schrödinger (NLS) equation including gain in fiber amplifiers.

Optical fiber amplifiers can be modeled as two-level systems since just two energy levels take place in light-inducing transition of energy between levels. The dynamic response for two-level systems is usually given with Maxwell-Bloch equations [33]. These equations can be applied to the case of fiber amplifiers. The induced polarization term $\mathbf{P}(\mathbf{r}, t)$ should be modified to include another term $\mathbf{P}_d(\mathbf{r}, t)$ that is expressing the dopant influence. This influence can be calculated using an approach that the dopant-induced dipole moment interact with the

optical field $\mathbf{E}(\mathbf{r},t)$. Using slowly varying envelope estimation, $\mathbf{P}_d(\mathbf{r},t)$ can be written as

$$\mathbf{P}_d(\mathbf{r},t) = \frac{1}{2}\hat{x}[P(\mathbf{r},t)\exp(-iw_0t) + \text{c.c.}] \tag{1.56}$$

Here $\hat{x}$ is unit vector of polarization, related to the optical field $\mathbf{E}(\mathbf{r},t)$. By solving the Bloch equations, the slowly varying part $P(\mathbf{r},t)$ is attained and it can be rewritten as [33]

$$\frac{\partial P}{\partial t} = -\frac{P}{T_2} - i(w_a - w_0)P - \frac{i\mu^2}{\hbar}EW \tag{1.57}$$

$$\frac{\partial W}{\partial t} = -\frac{W_0 - W}{T_1} + \frac{1}{\hbar}Im(E^*P) \tag{1.58}$$

Here μ is the dipole moment, w_a is the frequency of atomic transition. $W = N_2 - N_1$ is density of population-inversion with initial value W_0. T_1 and T_2 are relaxation times for population and dipole. $\mathbf{E}(\mathbf{r},t)$ is the slowly varying envelope related to optical field. The modification of NLSE equation by the effect of dopants is given as

$$\frac{\partial A}{\partial z} + \beta_1\frac{\partial A}{\partial t} + \frac{i\beta_2}{2}\frac{\partial^2 A}{\partial t^2} + \frac{\alpha}{2}A = i\gamma|A|^2A + \frac{iw_0}{\epsilon_0 c}\langle P\exp(-i\beta_0 z)\rangle \tag{1.59}$$

Here angle brackets mean averaging over the mode profile $|F(x,y)|^2$. In order to contain the effects of inhomogeneous broadening, frequencies of atomic transitions should also be averaged.

The three equations for Maxwell-Bloch should be solved for the pulses that are shorter than the dipole relaxation time ($T_2 < 0.1$ ps). Nevertheless, for relatively broader pulses one can simplify the analysis by using rate equation approximation for the dopants responding fast enough that the optical field is followed by the induced polarization[33].

By working in the Fourier space and defining the dopant susceptibility, dispersive effects of the dopants can also be taken into account;

$$\tilde{P}(\mathbf{r}, w) = \epsilon_0 \chi_d(\mathbf{r}, w) \tilde{E}(\mathbf{r}, w) \tag{1.60}$$

where ϵ_0 is the permittivity for vacuum. The tilde expresses the Fourier transform. The susceptibility is found to be given by

$$\chi_d(\mathbf{r}, w) = \frac{\sigma_s W(\mathbf{r}) n_0 c / w_0}{(w - w_a) T_2 + i} \tag{1.61}$$

Defining n_0 as refractive index of the host medium at frequency w_0, cross-section of the transition σ_s is linked to the dipole moment μ with $\sigma_s = \mu^2 w_0 T_2 / (\epsilon_0 n_0 \hbar c)$.

In order to obtain propagation equation for optical pulses using equations 1.57 through 1.61, we should apply an analysis that $\Delta\beta$ turns into frequency dependent since χ_d is also frequency dependent. Both β and $\Delta\beta$ should be expanded into Taylor series in order to include dispersive effects related to the dopants, when the optical field is transformed back to the time domain. Using $w - w_a = (w - w_0) + (w_0 - w_a)$ and expanding into Taylor series, one can derive the equation as [35]

$$\frac{\partial A}{\partial z} + \beta_1^{eff} \frac{\partial A}{\partial t} + \frac{i}{2} \beta_2^{eff} \frac{\partial^2 A}{\partial t^2} + \frac{1}{2}(\alpha + \alpha_2 |A|^2) A = i\gamma |A|^2) A + \frac{g_0}{2} \frac{1 + i\delta}{1 + \delta^2} A \tag{1.62}$$

where

$$\beta_1^{eff} = \beta_1 + \frac{g_0 T_2}{2} \left[\frac{1 - \delta^2 + 2i\delta}{(1 + \delta^2)^2} \right] \tag{1.63}$$

$$\beta_2^{eff} = \beta_2 + g_0 {T_2}^2 \left[\frac{\delta(\delta^2 - 3) + i(1 - 3\delta^2)}{1 + (\delta^2)^3} \right] \tag{1.64}$$

and the detuning parameter $\delta = (w_0 - w_a)T_2$. The definition of the gain g_0 is

$$g_0(z,t) = \frac{\sigma_s \int\int_{-\infty}^{\infty} W(\mathbf{r},t)|F(x,y)|^2 dxdy}{\sigma_s \int\int_{-\infty}^{\infty} |F(x,y)|^2 dxdy} \tag{1.65}$$

Here complete range of x and y are integrated. Two photon absorption effect is taken into acount in equation 1.62 using the parameter α_2. Although silica fiber mediated two photon absorption is minor, for the fibers made with high nonlinearity coefficient it may become significant [36].

As it can be seen from Equation 1.62, dopant involvement changes the host fiber dispersion parameter. As ν_g is equal to β_1^{-1}, deviations in β_1 points out that the dopants influence the pulse group velocity dispersion. Still the adjustment in the group velocity dispersion induced by the dopant contribution is insignificant in reality since under the usual working conditions the second term of equation 1.63 is nearly 10^4 times smaller. In contrast, deviations in β_2 can not be neglected since the two terms of Equation 1.64 may become similar in values particularly around the amplifier's zero dispersion wavelength. Even for the extreme case of $\delta = 0, \beta_2^{eff}$ is not equal to β_2. Actually, for $\delta = 0$ it is shown by Equation 1.64 that;

$$\beta_2^{eff} = \beta_2 + ig_0 T_2^2 \tag{1.66}$$

Here it can be seen that β_2^{eff} is complex factor with an imaginary part caused from the gain supplied by the dopants. The physical meaning of this situation can be explained with the finite bandwidth of gain in fiber amplifiers. Because of the wavelength dependence of the gain, it is called *gain dispersion*. Equation 1.66 is a result of an estimation in which fiber amplifier is assumed to have a parabola shape for pulse spectral bandwidth.

Applying an integration in Equation 1.65 is not an easy task since the inversion W does not only depend on spatial directions x, y, and z but it is also dependent on mode profile $|F(x,y)|^2$ due to saturation of gain. In reality, rare-earth ions

are doped into only a small part of the core part. In case of the dopant density and mode intensity are undeviating over the doped region, W can be expected to be a constant for the doped part and zero outside of it. Then the integration gives us the following result:

$$g_0(z,t) = \Gamma_s \sigma_s W(z,t) \tag{1.67}$$

Here Γ_s stands for the ratio of mode power for the doped region of the fiber. The dynamics of gain can be found using the equations 1.58 and 1.67 as:

$$\frac{\partial g_0}{\partial t} = \frac{g_{ss} - g_0}{T_1} - \frac{g_0 |A|^2}{T_1 P_s^{sat}} \tag{1.68}$$

Here $g_{ss} = \Gamma_s \sigma_s W_0$ is small signal gain and P_s^{sat} is the saturation power. Due to variations in pump power, g_0 is varying at different parts of the fiber. The dependence of g_0 on z is governed by the pumping configuration.

In classical approach, 1.62 and 1.68 should be solved together. Nevertheless, for the majority of fiber amplifiers, the fluorescence time T_1 is too long (0.1-10 ms) when compared to usual pulse durations, so it can be supposed that neither spontaneous emission nor pumping happen during the pulse duration. Equation 1.68 can then be used to get the following result:

$$g_0(z,t) \approx g_{ss} \text{exp}\left(-\frac{1}{E_s}\int_{-\infty}^{t} |A(z,t)|^2 dt\right) \tag{1.69}$$

Here the definition of saturation energy is given with $E_s = \hbar w_0 (a_s/\sigma_s)$. Usual values of E_s for fiber amplifiers are roughly around 1 μJ. However, the actual pulse energies in reality are much lower than the saturation energy. Consequently, for the duration of a single pulse, the gain saturation can be neglected. However, it is not negligible anymore for the train of pulses lasting over durations longer than T_1. Then the saturated gain inside amplifier is determined as $g_0 = g_{ss}(1+P_{av}/P_s^{sat})^{-1}$.

As a result, pulse propagation inside fiber amplifiers is ruled by a generalized Nonlinear Schrdinger Equation such that it has coefficients as β_1^{eff} and β_2^{eff} which

are complex as well as being variable along the z-direction(propagation direction) of the fiber. For the particular case of $\delta = 0$, Equation 1.62 can be rewritten with a significant simplification as:

$$\frac{\partial A}{\partial z} + \frac{i}{2}(\beta_2 + ig_0 T_2^2)\frac{\partial^2 A}{\partial T^2} = i\left(\gamma + \frac{i}{2}\alpha_2\right)|A|^2 A + \frac{1}{2}(g_0 - \alpha)A \tag{1.70}$$

Here $T = t - \beta_1^{eff} z$ gives us reduced time. Equation 1.70 is the equation that governs optical pulse propagation inside fiber amplifiers. T_2 term helps to find the reduction in gain for the spectral components that are far from the peak value of gain. Equation 1.70 is a generalized Nonlinear Schrödinger Equation with complex coefficients which can be reduced to Ginzburg-Landau equation[3].

1.8 Pulse Pickers

The repetition rate of the pulses generated in a mode-locked ultrafast laser is usually in the order of 10 MHz to 10 GHz[37]. For different reasons depending on the application, sometimes it becomes necessary to control the pulses in a sense that transmitting some of them and blocking the others. This picking process can be accomplished using a pulse picker, that is basically acting like an optical switch controlled by electronic circuits[38].

When an electro-optic modulator[39] or acousto-optic modulatorcite-dixon1967photoelastic is combined with an electronic driver circuit accomplishes to do pulse picking process. In order to form an electro-optic pulse picker device one should use a Pockels cell with certain polarized optics like thin-film polarizers such that the Pockels cell varies the state of the polarization of the input beam and the polarizer at the output blocks or transmits the pulse according to the polarization state.

The working mechanism of acousto-optic pulse picker relies on applying an RF field to the acousto optic modulator in order to deflect the desired optical pulse

into a direction that will be taken as output such that transmitting them through an aperture and blocking all the others.

In order to obtain high pulse energies for ultrafast pulses inside optical fiber amplifiers, it is often necessary to decrease repetition frequency. This reduction in repetition rate is generally achived via employing a pulse picker between the the amplifier and the seed laser. In this case the amplifier will amplify only the selected pulses. The loss resulted due to blocked beam can easily be compensated inside amplifier since the seed lasers are generally low average power compared to the amplifiers but still it can be adjusted such that the average power at the output of the pulse picker is enough to saturate the amplifier.

In the context of this thesis study, pulse pickers are used in order to increase energy per pulse as well as generating arbitrary pulse patterns, forming burst-mode pulses and controlling exposure durations of the laser beams by controlling the number of pulses to be applied onto the sample.

1.8.1 Acousto-Optic Effect

Acoust-optic modulators(AOM) are devices that can control the frequency, power or spatial direction of a laser beam via an electrical signal generated by a driver[40]. The fundamental principle of acousto-optic modulator is called *acousto-optic effect* which can be defined as the modification of the refractive index via a periodical mechanical pressure of an acoustic wave.

The fundamental element of an AOM is a crystal that the input light is propagating through. In order to excite a sound wave through this crystal, a piezoelectric transducer is generally attached to the surface of it and excited using an electronic signal. The excited acoustic wave can be in the order of hundreds of MHz. Then a Bragg diffraction occurs inside the crystal due to traveling change of refractive index caused by the acoustic wave. Because of this, AOMs sometimes are called as *Bragg cells*. The optical frequency of the diffracted beam is also affected by the diffraction process; depending on the direction of diffraction

(hence the direction of acoustic wave) a slight shift in optical frequency as an increase or decrease occurs. Since the wavenumber of the acoustic wave is very small, the shift is also small compared to the optical beam. In addition to frequency control, the frequency of the acoustic wave can also be used to control the direction of the diffracted beam while power of the acoustic wave constitutes a control for optical power. In case of the enough acoustic wave is applied to the crystal, more than %50, in extreme cases even more than %95, diffraction efficiency can be achieved.

At the other end of the crystal, acoustic wave can be absorbed. Traveling-wave geometry allows to accomplish a wide range of modulation bandwidth in the order of MHzs. Since other devices have resonances with the acoustic wave, a strong reflection for the acoustic wave at the other end of the crystal may often occur. This resonant boost can significantly increase the strength of the modulation (or reduce the necessary acoustic power), but decreases the modulation range in terms of bandwidth.

The most widely used materials for acousto-optic modulation are tellurium dioxide (TeO_2), crystalline quartz and fused silica[41]. While choosing the material, some criterias like the transparency range, optical damage threshold, coefficient of elasto-opticity and required dimensions should be taken into account. It is also possible to use different acoustic waves. Most widely used acoustic wave type is longitudinal waves since they lead to the highest diffraction efficiencies. However, it brings polarization dependency. Polarization independent diffraction is possible, with less diffraction efficiency, by using an acoustic movement in the direction of the laser propagation, which is called *acoustic shear waves*.

It is also possible to have more than one acousto-optic modulators by integrated optical device technology[42]. To give an example, an integrated optics on a piezoelectric material such as lithium niobate($LiNbO_3$) can be accomplished in order to generate surface-acoustic wave via metallic electrodes on the chip surface. Using such a device can be used as a tunable optical filter or an optical switch[43].

1.9 Material Processing with Ultrafast Lasers

The most important parameter for laser material structuring is the amount of energy deposited on to the material to be processed. The modification is governed by the temporal and spatial energy distribution as well as the total energy. In this section we will examine the material processing in two parts as semiconductors and dielectrics.

1.9.1 Semiconductors

In solids, leading interaction mechanism is the excitation of electrons via absorption of photons from their resting state to a higher energy excited states. In semiconductors, a single photon can excite valence band electron and cause it to occupy a conduction band state, as shown in Figure 1.10.

Even if the single photon energy of the applied laser does not match the electronic transition bandgap of the material, it is still possible to excite electrons and process materials through multiphoton electronic transitions. For a given fluence value, probability of the nonlinear absorption driven by multiphoton process increases sharply with shorter pulse duration and spatial focusing, hence increase in intensity.

After the initial excitation is formed on the material, secondary processes govern the process leading to modification on the material. Time order of these secondary processes are given in Figure 1.11.

The main electronic excitation is related with the coherent polarization of the material which has a very short lifetime. The polarization is terminated by the dephasing processes in very short time periods around 10^{-14} s[44]. Dephasing process does not affect the electronic energy state distribution during the phase of the excited states changes. The notion of dephasing depends on the spin-spin relaxation processes and from magnetic resonance it is familiar that matching

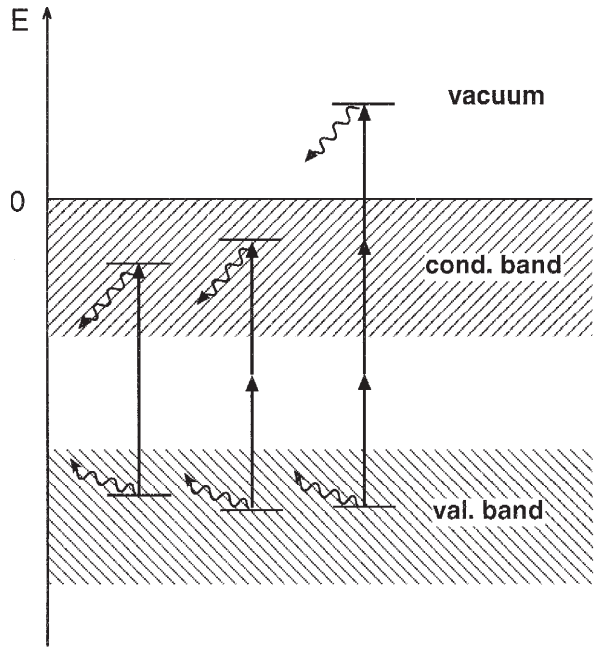


Figure 1.10: Excitation in semiconductor by single and multiphoton absorption

relaxation time is T_2[45].

The first distribution of the electronic states that are excited resembles the states coupled via the optical transitions. The primary state occupation quickly changes via carrier-carrier interactions, and in a time scale of roughly 10^{-13} s a quasi-equilibrium situation is reached amongst electrons. Fermi-Dirac distribution gives the distribution of carrier electron energy for free states with an electron temperature T_e higher than the temperature of the lattice. Knox et al. [46] have demonstrated that GaAs/GaAlAs quantum well structures constitute a rational example for electron thermalization.

The electrons in quasi-equilibrium state returns to equilibrium state by emitting phonons in time orders of 10^{-13} to 10^{-12} s. An experimental study to show cool-down of a thermal distribution of energetic electrons in silicon that is excited optically is given in Reference [47].

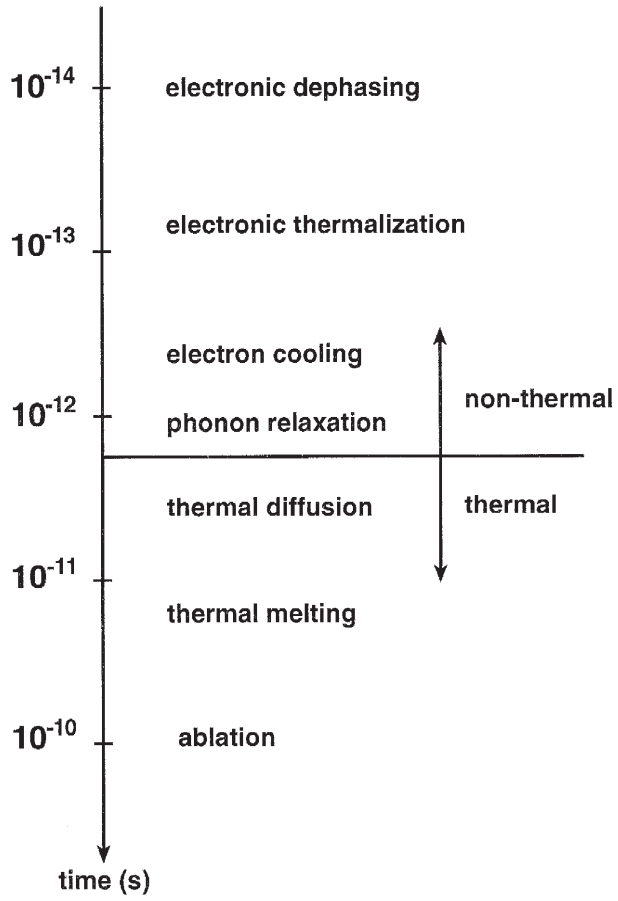


Figure 1.11: Secondary processes take place on different time scales

When electrons cool down by emitting photons, population of particular phonon modes increase. These phonons also interact with other phonon modes and emits secondary phonons such as acoustic phonons [48] and eventually returns to the original state. It is generally agreed that after the deposition of the energy by the laser, a few picoseconds is enough to assume that the energy distribution is in thermal equilibrium for most of the practical situations. Succeeding the thermalization process, the temperature profile gives good result for the spatial mapping of the energy distribution, hence optical absorption profile determines it for short pulses resulting in materials with strong absorption coefficients have very sharp gradients of temperature. For this condition diffusion of

the heat occurs in the orders of 10^{-11} s.

In solids, as soon as the adequate amount of energy is applied onto the material, the temperature reaches to the melting level, and a process of state change begins from solid to liquid. Regular thermal melting happens inhomogeneously via nucleation and liquid phase growth. The border untying two phases moves from the liquid to the solid. The duration needed to melt a solid layer is relatively high due to the upper limit of the velocity of the solid liquid interface is in the order of the speed of sound.For instance, the time duration needed to melt a surface layer of silicon with a thickness of 20 nm is around 50 to 100 ps [49].

An important conclusion of thermalization process is that there is a distinctive limit of 10^{-12} s between thermal and non-thermal material processing. Using the femtosecond pulses, if a process takes longer than 10^{-12} s than it is considered to be governed by the thermal processes. Under these circumstances, the initial pulse duration plays a minor role in the initialization of the process.

1.9.2 Dielectrics

When a transparent dielectric material is exposed to ultra-short pulses with high intensity, first free electrons are generated via multiphoton ionization. High-intensity laser field accelerates these free electrons and causing them to collide with other electrons, subsequently generating new free electrons. The ratio of these two acting mechanisms is determined by the width of the laser pulse. When the pulse is focused on the dielectric sample surface, at a very thin layer (1 μm) critical density plasma is formed and cause ablation by expansion of the approximately 10 eV plasma away from the surface[50]. Since the duration needed to transfer energy from the electrons to the lattice is in the orders of a few picoseconds in the dielectric materials, nearly no energy couples to the bulk of the material from the laser treated region. Experimentally measured and calculated thresholds for ablation to occur in fused silica are given in Figure 1.12. It can be seen that around $\approx$ 20 ps durations, deviation from long pulse behavior (given by $\tau^{(1/2)}$) occurs, showing that non-thermal ablation begins from this point on.

The measurements done in glass down to nearly 20 fs by Kautek et al.[51] are also included. As it can be seen, the threshold is decreasing for shorter pulses indicating that less energy is transferring to the adjacent areas as thermal load or shock. When the pulse widths are tremendously short, even avalanche ionization do not occur and only multiphoton ionization takes part in the ablation process by generating critical density plasma.

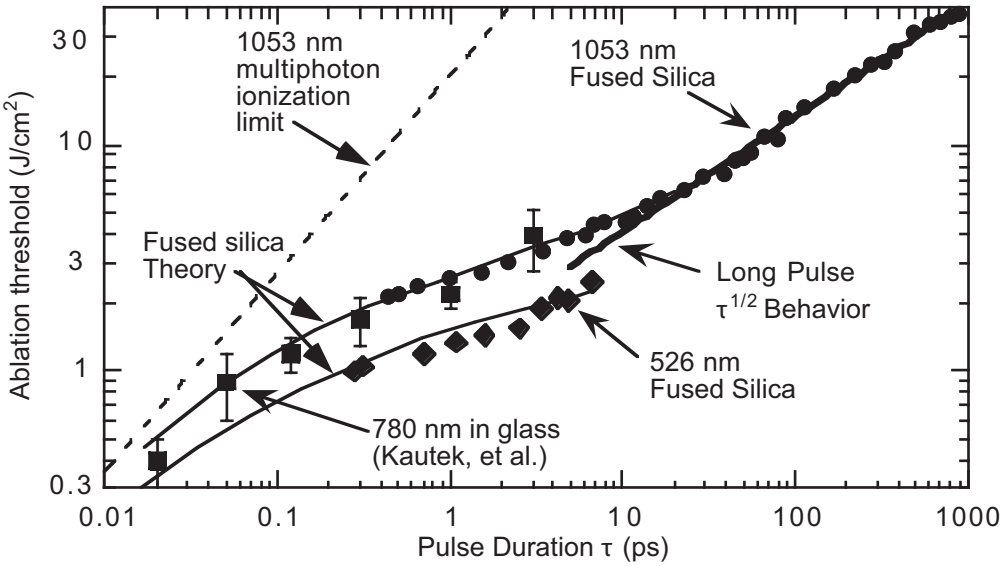


Figure 1.12: Measured and calculated ablation thresholds for fused silica. The deviation from $\tau^{(1/2)}$ indicates that there forms a new region that is nonthermal

Using the perspective of this mechanism for laser-material interaction, many materials like bones and enamel are basically dielectrics and show the same properties as fused silica. Stuart et. al. shown the difference between the nanosecond and femtosecond pulse material processing on dielectrics[52]. Figure 1.13 shows the surface of the tooth that is processed by two different regimes; 1.4 ns pulses and 350 fs pulses. In the sample processed by nanosecond pulses the thermal shock-induced cracks around the ablated area are clearly visible. In this time regime, thermal stresses and inhomogeneous energy absorption due to linear absorption of defects causes the ablation to occur firstly at the points with lowest

material strength. However, in the sample ablated with femtosecond pulses all the regions irradiated by laser beam exposed to energy levels well beyond the ablation threshold leading to exceptional ablation and removal of material homogeneously and precisely. When the morphology of the region processed by the femtosecond laser is examined, no cracks or other effects exist showing heat transfer to the surrounding area, even in the close vicinity.

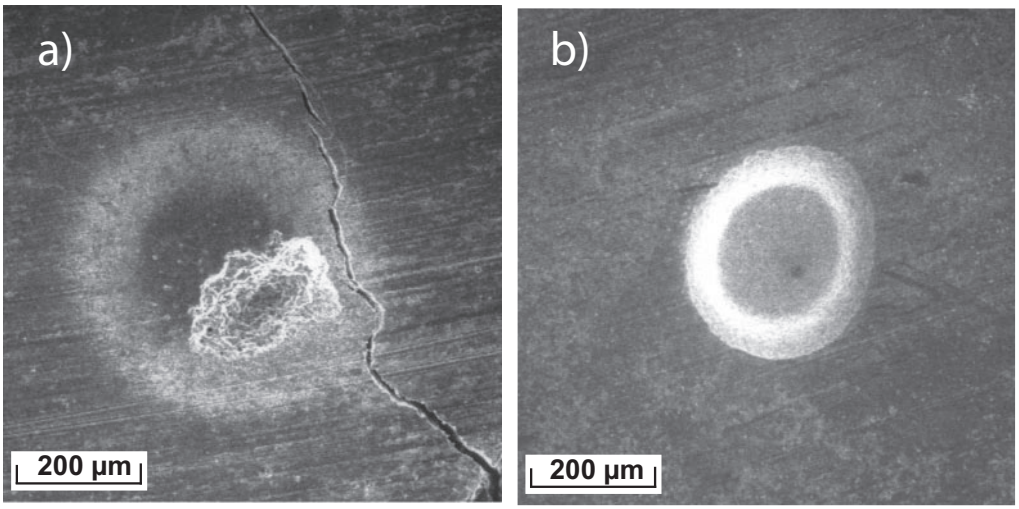


Figure 1.13: a) Nanosecond, b) femtosecond processing of tooth samples

The non-thermal nature of this material ablation mechanism leads to no temperature increase around the treated area. Thermal measurements on the sample show that when 500 pulses with 1 ns pulse duration are irradiated to a 1 mm thick slide of tooth tissue, it causes 40 °C temperature rise while it was only 2 °C for the same material removal that was done by femtosecond pulses. In both cases, the fluence parameter for both of the lasers were adjusted to remove 1 μm depth removal of material per pulse. This process necessitated only 3 J/cm^2 for the fs pulses while it was 30 J/cm^2 for the ns pulsed case. It can be foreseen that the consequences for dentistry is significant. Practically for the temperature changes over 5 °C, active cooling of teeth are required during a tooth operation and if this operation is done using femtosecond pulses, no cooling would be necessary.

Another example to show the effectiveness of femtosecond laser-induced material processing for dielectric materials is the ablation experiments on highly explosive materials. Machining and cutting of such materials exhibit substantial difficulty since they are highly energetic. When the widely-used machines and tools for material processing are used for such materials, process is highly dangerous and may cause significant reactions from the material in cases like improper configuration of the machine or improper adjustment of speed. Furthermore, hazardous waste is usually generated during the cutting process from the machining chips or the fluids used to cool the material during the process. Hence, ablation of explosives using femtosecond pulses promises an alternative solution for the machines currently used. Nonlinear absorption of femtosecond pulses results in nearly no heat deposition on sample resulting in "cold ablation" of the sample[53].

Chapter 2

Femtosecond Fiber Laser-Microscope System Development for Nanosurgery

2.1 Introduction

In the recent years, ultrashort pulsed lasers have been utilized in diverse biomedical applications. In addition to well-known applications such as nonlinear imaging [54, 55] and biomedical implant surface modification, dissection and manipulation of cellular and even subcellular structures, such as neuronal axons [56], dendritic spines[57], mitochondria[58] and cytoskeletal elements[59] shown to be possible using ultrashort pulses. This process of manipulation cells and tissues at submicron precision level is named nanosurgery. In recent years, various research have shown that the femtosecond photodisruption technique represents a useful tool for in vivo nanosurgical operations [60, 61]. To date, nanosurgery researches have relied on solid state lasers, especially Ti:sapphire lasers. Even though these lasers provide good laser properties such as good beam quality and high pulse energies with short pulses, they have big disadvantages like being large in size, complex to operate and having long-term stability issues. In addition to these,

their oscillators operate at a fixed repetition rate around 80 MHz and amplified systems are constrained to a few kHz. Repetition rate control of these lasers' oscillators are provided by complex and expensive Pockels cells. In the recent years, research in the fiber laser field led to development of fiber lasers which can provide necessary energy levels for nanosurgical applications. Fiber lasers' biggest advantages over solid state lasers are that they are more compact in size, simpler to operate and cost much less. Moreover their pulse repetition rate can be controlled using acousto-optic modulators (AOM). Another important property of fiber lasers and amplifiers are that they have low intensity noise which can be an important parameter for ablation precision due to nonlinear nature of ablation process. Although fiber laser based multiphoton imaging systems have been built in the recent years, fiber lasers have not been used for nanosurgery up to date. Here in this thesis study, for the first time to our knowledge, mode-locked fiber laser system is utilized for nanosurgery[62]. The custom-developed laser is coupled into a home-built diffraction limited microscope system with computerized imaging and sample positioning. The capability of system demonstrated by the experiments on tissue, cellular and subcellular level experiments.

2.2 Laser-Biological Material Interaction

In order to comprehend different types of interactions when laser irradiated onto a tissue, it is vital to understand how photons penetrate into tissue. As photons reach the tissue surface, due to refractive index difference between tissue and the air, some part of the photons reflect back from the surface. The photons that are not reflected and go through the tissue refracts according to the Snells Law. Since the refractive index of the tissue is higher (n_{tissue}=1.4) than the refractive index of air, the photons are refracted in the direction of the vertical axis of the surface. Snell's Law indicates:

$$\frac{\sin \alpha_1}{\sin \alpha_2} = \frac{n_2}{n_1} = n_{12} \tag{2.1}$$

Basically, two interactions may occur in the tissue; photons may scatter, i.e. change their path according to the anisotropy factor g, or they can be absorbed; leading to an energy increase for the absorbed molecule by means of electronic transition.

2.2.1 Absorption

Absorption in molecules is possible only in a special condition where the photon energy, $E = h\nu$ is equal to the energy gap between the states of a molecule. When a photon is absorbed by a chromophore, it causes either a change for the distance of charges(generally by UV or visible light) or a change in the vibrational mode of the molecule (generally by near infrared light). The most common absorbing materials inside tissue are hemoglobin, melanin, poryphyrin, flavin, nuclear acids, retinol, deoxyribonucleic acid (DNA) and ribonucleic acid (RNA). Absorption in these molecules leads to intense and discrete absorption bands. Water absorption dominates the near infrared(NIR) and mid infrared(MIR) region absorption profile of tissue. The peak value for water absorption is around 3 μm wavelength. While the coefficient μ_a (cm^{-1}) gives an idea about absorption, the inverse, l_a characterizes the depth for penetration(mean free path) into the tissue.

In order to analyze how the absorption works, for a chromophore placed under a parallel laser beam, we should define an effective cross-section of the chromophore, σ_a cm^2, which is usually smaller than the geometrical cross-section, A. If we make the analysis for a solution with chromophore density of $\rho_a(\text{cm}^{-3})$, the absorption coefficient can be calculated as $\mu_a = \rho_a\sigma_a(\text{cm}^{-1})$. Beers Law can be used to calculate the light transmission through a cuvette with thickness d, filled with absorbing liquid given with the mentioned chromophore density. Accordingly the transmission, T, through the fluid can be found as;

$$T = \frac{I}{I_0} = \exp(-\sigma_a N_a l) = \exp(-\mu_a l) \tag{2.2}$$

Here σ_a is effective cross-section of absorption in cm^2, N_a is the density of

absorbing molecules in cm^{-3}, l is the optical path in cm and μ_a is the absorption coefficient in cm^{-1}

Absorption spectra for the water and the commonly found chromophores inside tissue are given in Figure 2.1.

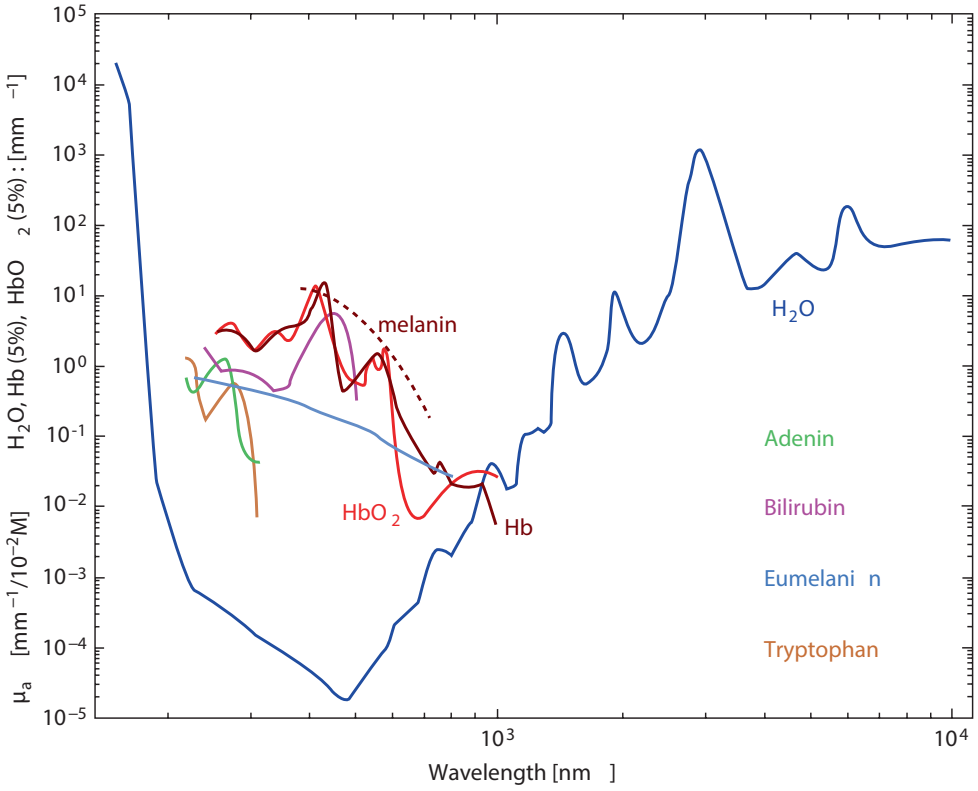


Figure 2.1: Absorption spectra for water and most commonly found chromophores inside tissue

The first methodical exhibition of laser-tissue interaction according to laser fluence, intensity and pulse duration was done in 1986 by Boulnois [63] (Figure 2.2). For very short and ultrashort pulses, there are two mechanisms dominating the laser-tissue interaction; *photo-ablation* and *photo-disruption*.

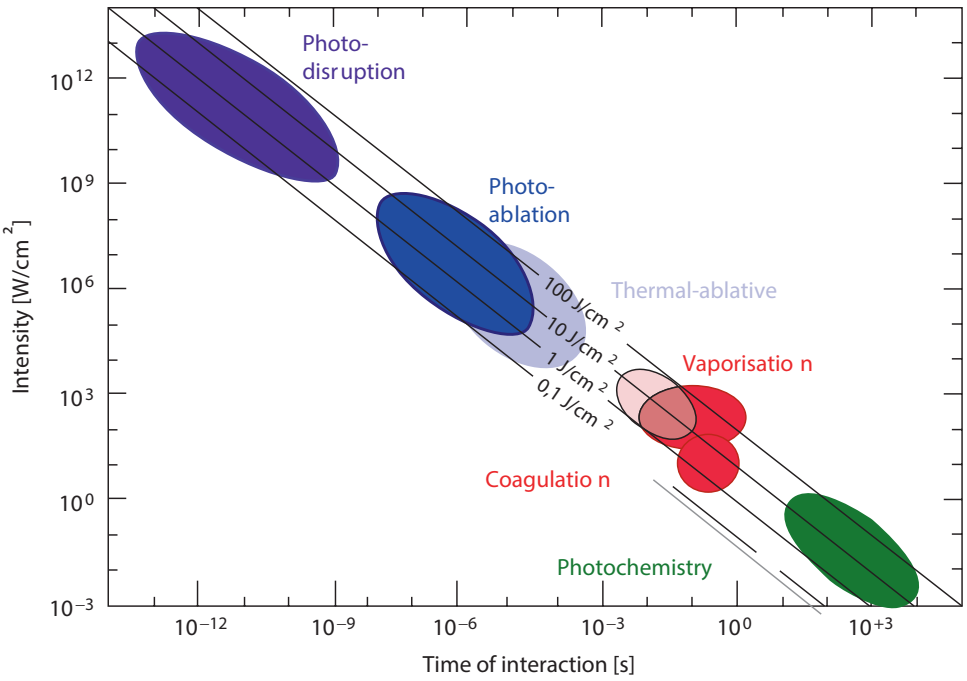


Figure 2.2: Laser-tissue interaction mechanisms for different laser durations and intensities

2.2.2 Tissue Ablation

The requirements for tissue ablation to occur are very short-pulsed laser beam and high absorption rate. When the tissue is heated using laser pulses, a stress wave develops inside the heated volume and propagates to the outer direction. If the pulse is shorter than the stress propagation time, t_m, similar to the heat confinement, stress confinement occurs and stress wave will not find enough time to travel outside the processed volume. The internal stress is given with *Grüneisen coefficient*[64], Γ,

$$\Gamma = \alpha/(\rho c_w \kappa_T) \tag{2.3}$$

Here α is thermal expansion coefficient, ρ is the density, c_w is the specific heat, and κ_T is the isothermal compressibility. For the stress wave propagating through the irradiated volume, the propagation time, t_m is given by the following:

$$t_m = 1/(c_a \mu_a)[\mathrm{s}] \tag{2.4}$$

Here c_a is the sound speed for the processed medium. If the stress wave can not leave the heated volume with the speed c_a until the pulse ends, then the stress is also removed with the ablated material and can not reach to the surrounding area and into the material.

In order to obtain ablation in tissue, a threshold value should be exceeded. The depth of the ablation, d, per laser pulse is increases with the pulse energy until a threshold of saturation. This simple model derived for calculating the ablation depth is called blow-off model [64]. In this model it is assumed that there is a threshold, $F_s(d)$, for ablation to occur and no material removal happens below this threshold. Ablation threshold is given by: $F_s(d) = F_0 \exp(-\mu_a d)$. Using this relation, ablation depth, d, can be found as:

$$d = (1/\mu_a) \ln(F_0/F_s) \tag{2.5}$$

UV lasers (ArF excimer laser) and pulsed mid infrared (MIR) lasers are in the range of the necessity for high absorption that they are suitable for photoablation.

2.2.3 Photodisruption

When the pulses with durations of nanoseconds (e.g. generated from Q-switch Nd:YAG lasers) or picoseconds and femtoseconds (e.g. Ti:sapphire lasers or more recently; mode-locked fiber lasers) are focused into a tight spot, it is possible to exceed power densities of $10^{12}\mathrm{W/cm}^2$. This high-intensity light can extract electrons out of the atoms, causing a plasma to form and generate an optical

breakdown that disrupts the tissue. Boulnois [63] and Vogel [64] give the details of this photomechanical process.

When the laser intensity in the focused volume reaches $10^{11}\mathrm{W/cm}^2$, nonlinear absorption process begins and absorbed light ratio increases significantly. An intense white light and an acoustic signal follow the nonlinear absorption causing an optical breakdown with plasma formation inside tissue. The ionization of atoms occurs due to multiphoton absorption that is highly intensity dependent and varies with I^4. High-intensity electromagnetic field in the environment causes the free electrons to accelerate (inverse Bremsstrahlung). These accelerated and highly energetic electrons generate new free electrons through collision ionization (Avalanche effect, Figure 2.3). The hot electrons and ions lead to plasma formation with a temperature at $15000 - 20000^\circ$ K and a pressure between 20 to 60 bars. This process in the tissue is followed by a formation of a cavitation bubble of water vapor. The size of this bubble is determined by the pulse energy and pulse duration of the laser. While the pulse gets shorter, optical breakdown occurs at lower pulse energies; cavitation bubble gets also smaller and side effects caused by the bubble decreases.

In case of a Gaussian beam is focused, it creates a plasma with a length of Z_{max}. This length is defined using Rayleigh length of the focus (Z_R) and pulse intensity that is above the threshold, I_0/I_{th}, for the optical breakdown to take place.

Plasma length can be found using the equation below:

$$Z_{max} = Z_R(I_0/I_{th} - 1)^{1/2} \tag{2.6}$$

Here Z_R is the Rayleigh length and it is defined as $Z_R = \pi {w_0}^2/\lambda$ where w_0 is the beam waist and λ is the wavelength in the medium modified by the refractive index. Ultrashort laser pulses also found use in medical applications such as ophthalmology in cutting flaps of the cornea. Very successful and precise tissue removal for both soft and hard tissue are achieved using femtosecond pulses,

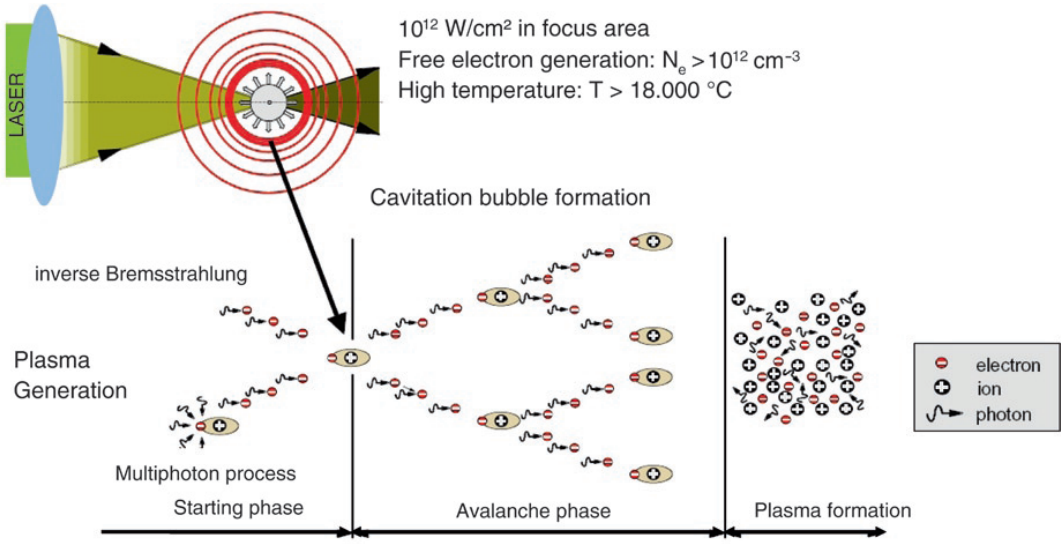


Figure 2.3: Schematic showing the development of optical breakdown due to ultrafast pulses inside tissue

but the removal rate and efficiency has not been very high enough up to date. Therefore most of the applications of multiphoton absorption stayed limited in the application areas like microscopy and tissue diagnostics.

2.3 Experimental Setup and Results

The system developed for the study of nanosurgery can be examined in three main titles:

- Fiber Laser System
- Customized Microscope Setup
- Control Electronics and Software

2.3.1 Fiber Laser System

The fiber laser setup is shown in Figure 2.4.

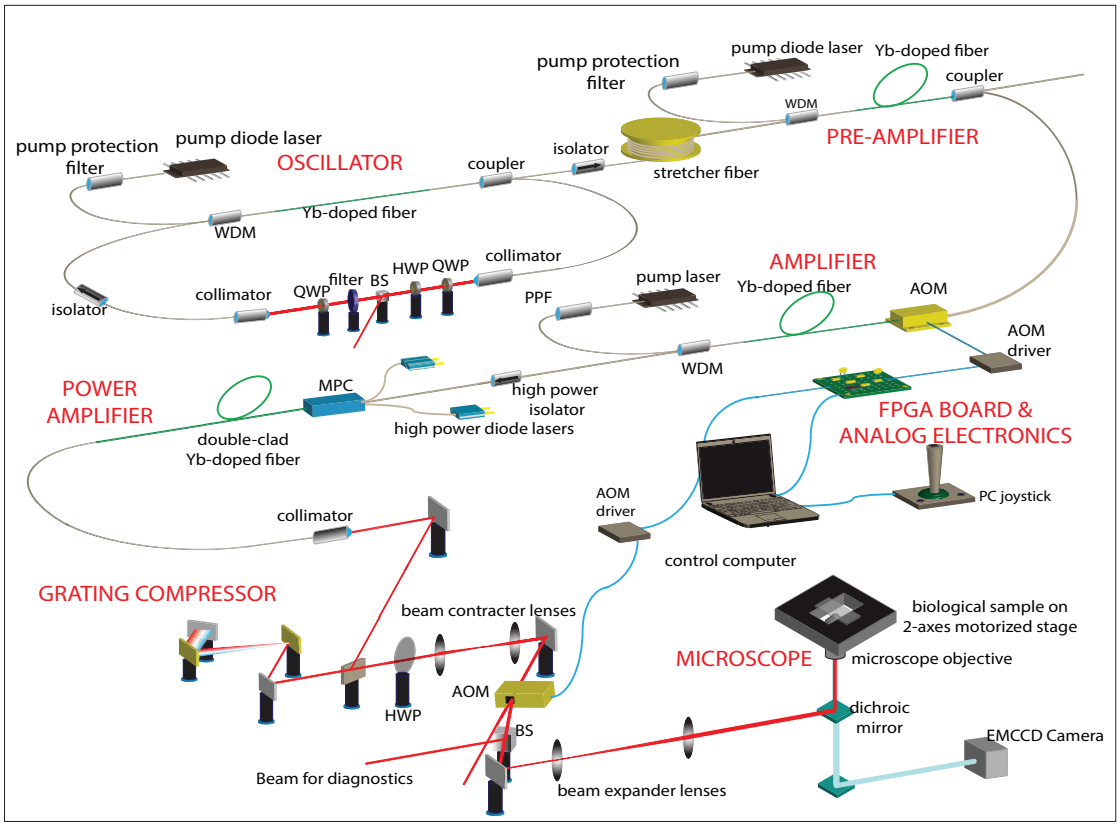


Figure 2.4: Schematic of the laser setup. FPGA: field programmable gate array; AOM: acousto-optic modulator.

The seed oscillator is an Yb-doped fiber laser, operating in the all-normal-dispersion regime [65]. The choice of the mode-locked regime was dominated by the desire to have an extremely robust system. This mode-locking regime results in relatively longer and structured pulses. However, it is the amplifier system that effectively determines the pulse duration as a result of gain narrowing and residual higher-order dispersion [66]. The oscillator incorporates a 5 m-long section of single-mode fiber (SMF, of the type HI-1060) and 0.6 m-long Yb-doped fiber, followed by another 0.4 m of SMF. Net group velocity dispersion, GVD_{net},

of the oscillator is calculated to be around 0.138 ps^2. The gain fiber is pumped in core with a pump diode delivering 310 mW of power through a 980/1030 nm wavelength division multiplexer. Unidirectional operation is ensured using an in-line optical isolator. Mode-locking is initiated and stabilized by nonlinear polarization evolution. Single pulse operation of the laser output is verified via long-range autocorrelation against bound pulse generation and RF spectral measurements (with up to 12 GHz) against regular multiple pulsing. The in-line amplifier system comprises of a fiber stretcher, a fiber-pigtailed AOM, and three gain stages.

The first two stages are core-pumped. The final stage is cladding-pumped, where pump light is delivered through a signal-pump combiner. The lengths of single-mode Yb-doped fibers used for pre-amplifier and amplifier stages are 1.0 m and 0.5 m, respectively. The core diameters are 6 μm. First stage is pumped with 300 mW pump power in the forward direction and the second stage is pumped with 120 mW in the backward direction. The final stage comprises of a 2 m-long Yb-doped fiber with 20 μm core, 125 μm cladding diameters and numerical aperture of 0.08. The gain fiber is pumped in the forward direction with a pump diode laser producing 2 W centered around 976 nm. The beam extracted from the amplifier using a fiber-coupled collimator. The amplified pulses are dechirped in a standard diffraction grating compressor.

The oscillator mode-locks easily and remains mode-locked with the characteristic optical spectrum shown in Figure 2.5. Low-noise operation is verified by the 80 dB signal-to-sideband suppression as observed through RF spectral measurements (inset of Figure 2.5(b)). The oscillator produces 3-ps-long chirped pulses with a bandwidth of 15 nm at a repetition rate of 32.7 MHz. Output coupling from the cavity is achieved through a %20 output coupler, which delivers 32 mW of average power to the fiber stretcher, which consists of 40 m of single mode fiber (HI-1060). Pulses are stretched to $\sim$35 ps and then amplified to 4.5 nJ energy per pulse in the first amplifier stage. After the first amplifier stage, repetition rate of the pulses are reduced to a desired repetition rate, which can be chosen between 1.02 to 32.7 MHz, depending on the application. The role of the second amplifier stage is to compensate for the power reduction due to pulse picking in

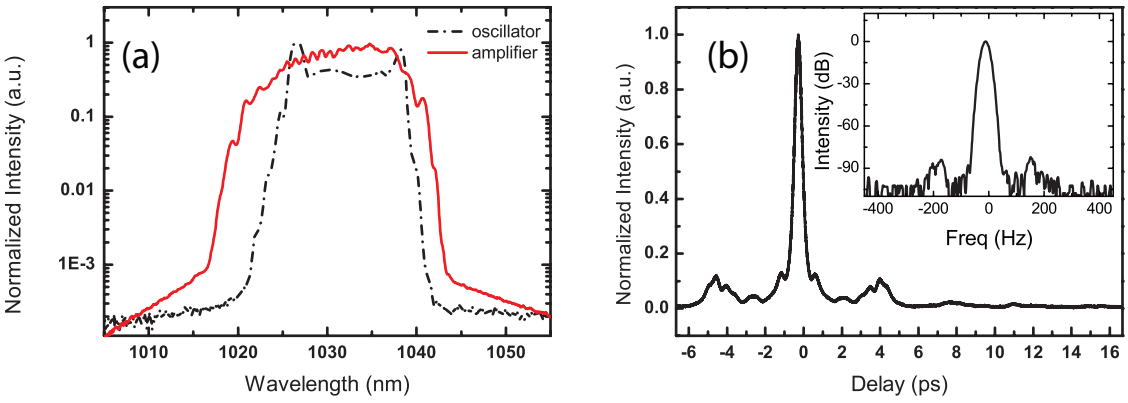


Figure 2.5: Spectrum and autocorrelation data of the compressed laser amplifier output

the AOM (the insertion loss is ∼4 dB, in addition to losses due to pulse elimination), producing approximately 110 mW of average power, virtually independent of the pulse picking frequency in the AOM. The final power amplifier functions as a power booster to reach pulse energies necessary for ablation of the biological specimens, with a maximum pulse energy of ∼125 nJ, which corresponds to an average power of 500 mW at 4.08 MHz repetition rate. The laser system itself is not limited in average power (with a similar configuration, we were able to reach 50 W), but in pulse energy by nonlinear effects. It is also indirectly limited in average power by the damage threshold of the microscope objectives. After dechirping in the grating compressor, the compressed pulse duration is approximately 240 fs. The optical spectrum of the chirped, amplified pulses and autocorrelation after dechirping are shown in Figure 2.5 (a) and Figure2.5 (b), respectively. A second, free-space AOM is present for gating of the individual pulses, enabling precise control of the exposure time of the laser on the specimen as well as the further reducing of the repetition rate down to 1 kHz or formation of pulse bursts (Figure2.6)

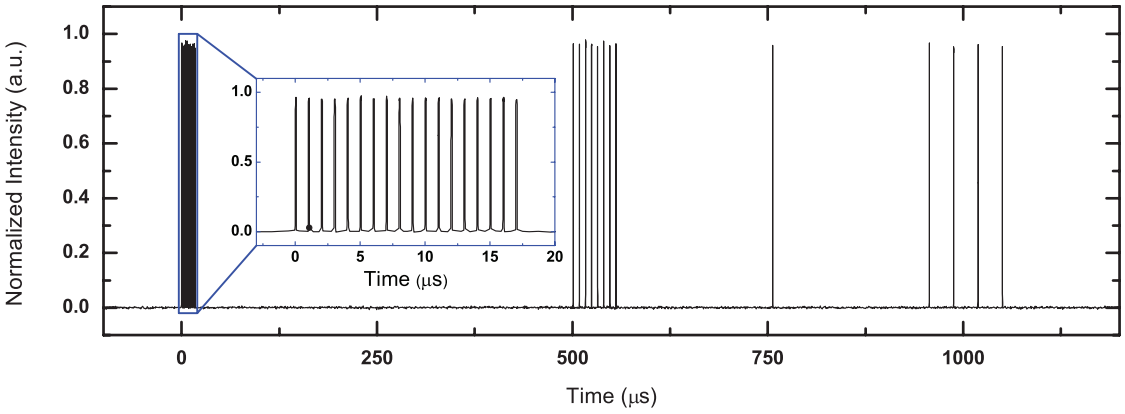


Figure 2.6: Schematic for electronics circuitry to control pulses and form arbitrary pulse pattern via AOMs

2.3.2 Customized Microscope Setup

For real-time imaging of the biological sample, a customized epi-fluorescent microscope (Nikon Ti-U) is used. A telescope is used to expand the beam, which is directed to the objective with a dichroic mirror housed in an extra turret. The dichroic mirror is highly reflective at the laser wavelength, while transmitting visible light and fluorescence excitation (Fig 2.7). Sample positioning is accomplished via a 2D micropositioning stage (with a precision of $\sim$ 1 μm) and a 3D piezo stage with $\sim$20 nm precision. For most applications, the micropositioning stage alone provides sufficient resolution. Visualization is based on fluorescent and phase-contrast imaging. A 60X,1.2-NA objective and a 100X, 1.3-NA objective are used interchangeably for sub-cellular ablation and a 20X, 0.4-NA, phase-contrast objective is used for multicellular/tissue-level ablation, on both cases, together with a high-sensitivity EMCCD camera for imaging. All major aspects of the laser-microscope system, including control of the FPGA system for pulse picking and gating, positioning of the sample, control of the camera and image acquisition are controlled via a computer for nearly completely hands-free operation. A computer joystick allows ease of use for positioning.

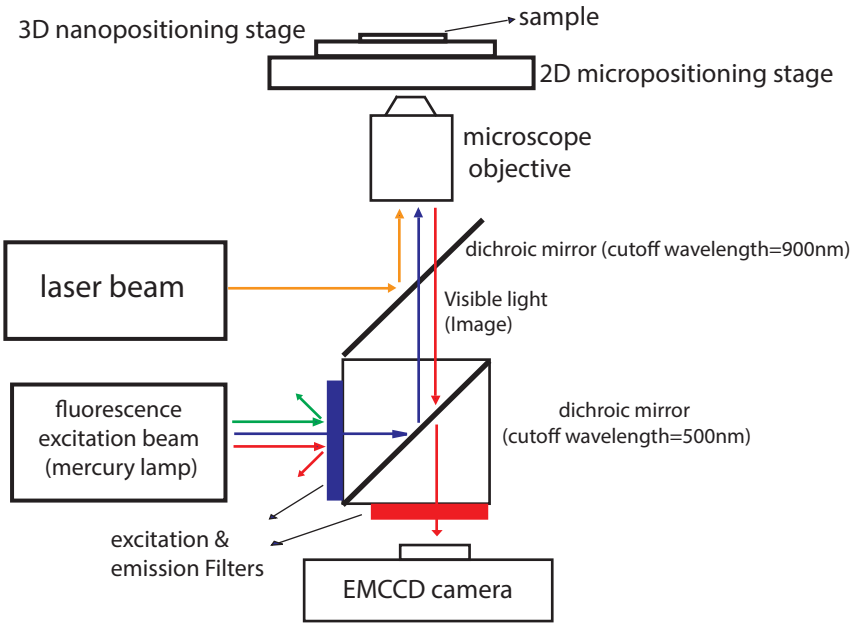


Figure 2.7: Schematic of the laser-fluorescence microscope optics

2.3.3 Control Electronics and Software

The pulse picking is handled by an in-house developed FPGA design to pick pulses at two AOMs positioned after the amplifier stages. The FPGA is controlled through a user interface software running on a PC. A portion of the laser signal is detected at a fast photodiode and the output is fed to the FPGA as the clock source. In order to have higher temporal resolution in picking out the optical pulses, a faster clock signal is needed. Thus, the clock signal derived from the repetition rate of the laser, is multiplied by 8 at the digital clock manager inside the FPGA to ∼262 MHz. A one-time-only delay adjustment in the FPGA allows the new clock signal to be fully synchronized to arriving optical pulses at the AOMs. The FPGA starts counting the pulses and sends gating signal to the AOM drivers when a pulse is to be picked. As well as picking out the pulses continuously, the system is capable of working in arbitrary picking mode. The user is able to pick and drop any number of pulses through the software interface, which can be configured to produce a predefined pulse sequence upon the press

of a button. There are virtually no limitations on the pulse sequences that can be defined.

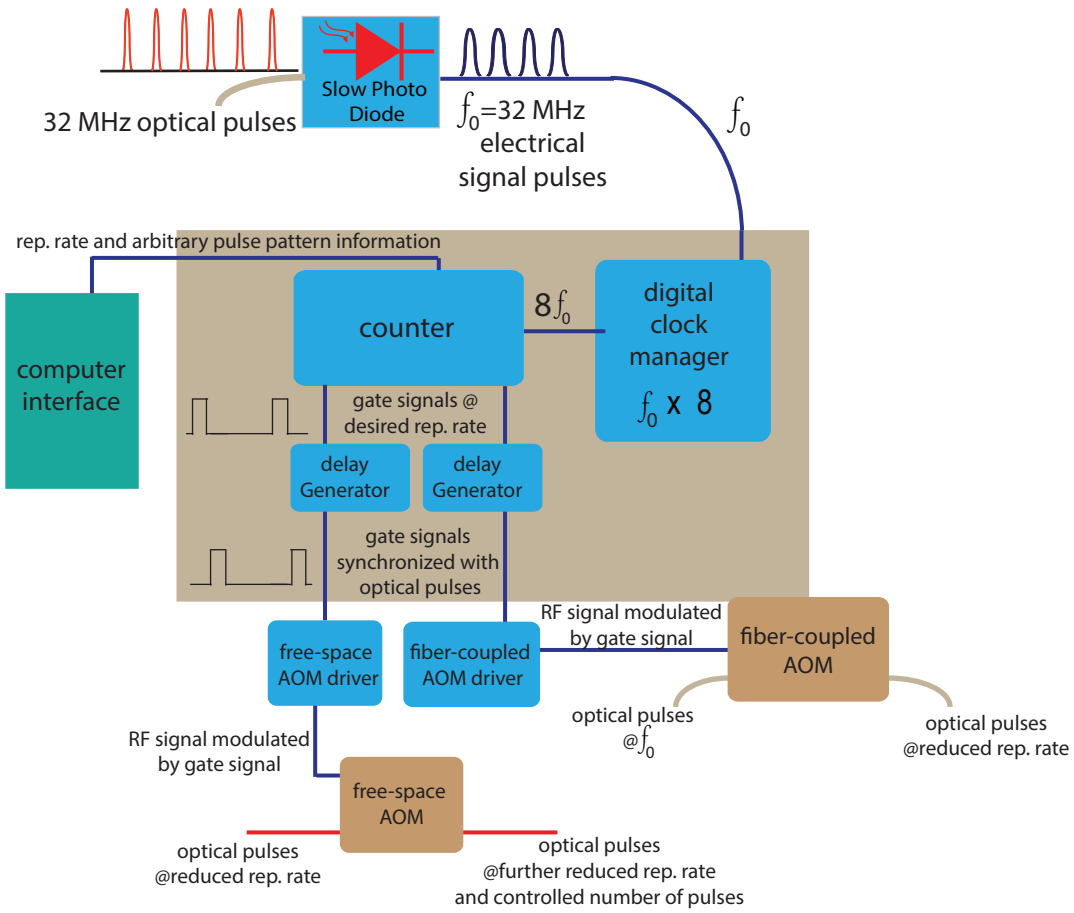


Figure 2.8: FPGA circuit scheme used for rep. rate adjustment and arbitrary pulse pattern generation using AOMs

2.4 Laser Experiments on Biological Samples and Results

In order to demonstrate the system's capability to achieve femtosecond photodisruption of biological samples, 240-fs, 7-nJ pulses at 4.08 MHz were used to make

cuts on frozen sections of mouse gastrocnemius muscle. The beam was focused to a spot size of ~ 2.2 μm using the 20X objective; the telescope is adjusted to fill the aperture of the 60X and 100X objectives completely, resulting in underfilling of the 20X objective. 5 parallel, linear cuts were made, as shown in Figure 2.9.

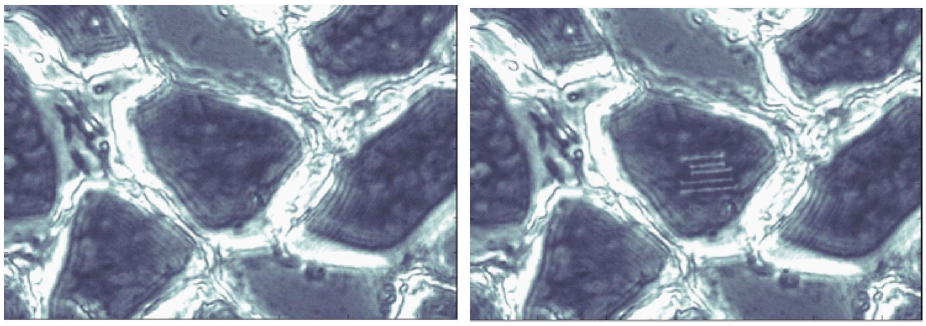


Figure 2.9: Tissue slice (mouse gastrocnemius muscle) (a) before and (b) after ablation; 4.08 MHz, 240-fs, 7-nJ.

The line widths were measured to be $2 - 2.5$ μm, consistent with the spot size. Next, femtosecond photodisruption is performed on chemically fixed Saos-2 cells using the 60X objective. In this mode of operation, sub-micron features are obtained (Figure 2.10).

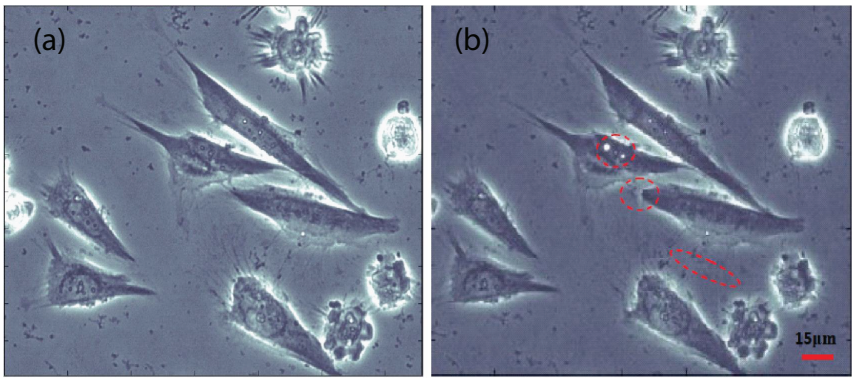


Figure 2.10: Fixed Saos-2 cells (c) before and (d) after sub-cellular surgery; 4.08 MHz, 240-fs, 7 nJ.

The system's capability of targeting single organelle of live Saos-2 cells were

examined using the 100X objective. We ablated part of a single mitochondrion (stained with Mitotracker Red 580, Invitrogen) with 2 nJ pulses(Figure 2.11). We have ruled against photobleaching, by applying FRAP (fluorescence recovery after photobleach) [67] several hours after the operation. Continuous monitoring of the cell during this time showed that the cell viability was not affected.

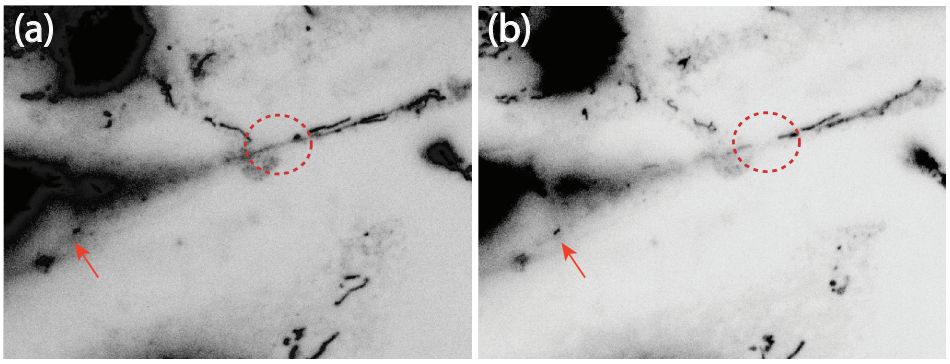


Figure 2.11: (a) Before and (b) after ablation of single mitochondrion stained with Mitotracker Red 580; 4.08 MHz, 240-fs, 2 nJ.

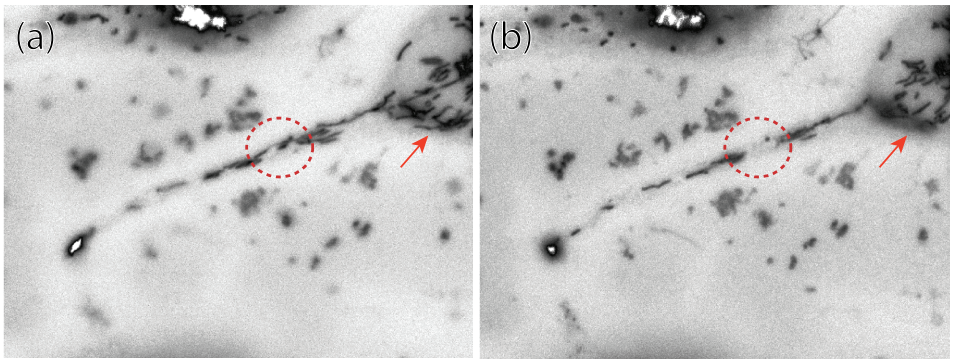


Figure 2.12: (a) Before and (b) after ablation of single mitochondrion stained with Mitotracker Red 580; 4.08 MHz, 240-fs, 2 nJ.

Finally, we have utilized our system to perform axotomy on differentiated neuroendocrine PC12 cells. An axon of a PC12 cell was damaged with the laser beam with 8 nJ pulse energy at 32.7 MHz repetition rate (Figure 2.13). The

procedure interrupted the viability of the cell and after a few minutes wallerian degeneration came up, with prominence of the bead-like structures.



Figure 2.13: (a) Before and (b) at the moment of laser axotomy (white arrow indicates the incident laser beam on the axon). (c) After axotomy (white dashed arrow indicates the micro-damage); 32.7 MHz, 240-fs, 8 nJ.

2.5 Conclusion

In conclusion, we have demonstrated the use of a custom-built fiber laser-based microscope system for nanosurgery and tissue ablation experiments. Our system constitutes a novel and highly practical instrumentation for ultrafast photodisruption, making maximal use of the advantages offered by fiber technology. The laser system is extremely robust. Through the use of custom FPGA electronics acting through fiber-coupled AOMs, we are able to generate pulse sequence with no limitations (apart from the maximum repetition rate, which is that of the oscillator), while the MOPA architecture ensures that the individual pulse energy remains the same. The highly computerized operation of the system paves the way towards automated execution of a sequence of operations on a number of cells. These advantages are obtained at a fraction of the cost of a Ti:sapphire laser, which has traditionally been the system of choice for these experiments. We expect the demonstration of a highly practical and low-cost system will aid the proliferation of ultrafast laser-based ablation experiments in biological sciences.

Chapter 3

Nanosecond Supercontinuum Fiber Laser System for Photoacoustic Microscopy

3.1 Introduction

Photoacoustic microscopy (PAM), as an imaging modality, has shown promising results in imaging angiogenesis [68] and cutaneous malignancies like melanoma [69], revealing systemic diseases including diabetes [70], hypertension [71], tracing drug efficiency [72] and assessment of therapy [73], monitoring healing processes such as wound cicatrization [74], brain imaging and mapping [75]. Clinically, PAM is emerging as a capable diagnostic tool. Parameters of the laser used in PAM, particularly, pulse duration, energy, pulse repetition frequency (PRF), and pulse-to-pulse stability affect the signal amplitude and quality, data acquisition speed and indirectly, spatial resolution. Lasers used in PAM are typically Q-switched lasers, low-power laser diodes, and recently, fiber lasers. Significantly, in all of these lasers, the key parameters can not be adjusted independently, whereas microvasculature and cellular imaging, e.g., have different requirements. Here, we report an integrated fiber laser system producing nanosecond pulses, covering

from 600 nm to 1300 nm, developed specifically for photoacoustic excitation[76]. The system comprises of Yb-doped fiber oscillator and amplifier, an acousto-optic modulator (AOM) and photonic-crystal fiber to generate supercontinuum. Complete control over the pulse train, including generation of non-uniform pulse trains, is achieved via the AOM through custom-developed field-programmable gate-array (FPGA) electronics. The system is unique in that all the important parameters are adjustable: pulse duration (1-3 ns), energy (up to 10 μJ), repetition rate (50 kHz - 3 MHz). Different photocoustic imaging probes can be excited with the ultrabroad spectrum. The entire system is fiber-integrated; guided-beam-propagation renders it misalignment free and largely immune to mechanical perturbations. The laser is robust, low-cost and built using readily available components.

3.2 Theoretical Background

3.2.1 Photothermal Effects

The most common encountered type of laser-tissue interaction in biomedical applications is the thermal effects. Since they do not need ultra-short pulse durations that became available relatively in the recent years, they are one of the first to be investigated. There are various medical applications of photothermal effects such as tumour vaporization [77], removal of skin marks such as tattoo or port wine birthmarks [78], and welding gastrointestinal ulcers [79].

In photochemical effects(such as photodynamic therapy), tissue damage is usually done by following a specific reaction chain. However, for the photothermal effects there is no path to follow and any biomolecule may absorb the incident photons, and these photons may result in thermal effects. In photothermal effects, firstly energy is deposited into the material through absorption of photons and this energy converts into heat energy by relaxation of photons by colliding of atoms. These collisions are the source of temperature rise of the tissue. By

diffusion, the heat transfers to the surrounding area and cause an increase in the temperature of the surrounding tissue too.

3.2.2 Photoacoustic Imaging

In addition to the mentioned applications, phothermal effects are also an effective tool for diagnostics in biomedicine. Photoacoustics is a newly developed and promising diagnostic method with possible applications in breast imaging, blood vessel microstructure visualization up to 1-2 cm depth which can also be utilized to see tumours using unusual structuring in vasculature. It has already began to be used for mostly preclinical studies such as small animal imaging.

The fundamental principles of photoacoustic imaging is given below and illustrated in Figure 3.1 [80].

1. Firstly, the tissue to be imaged is illuminated using a wide enough beam with short duration (usually nanoseconds), using a diode laser, Q-switched Nd:YAG laser. For our case, this illumination is done using a nanosecond fiber laser.

2. The light from the illumination source is scattered in the tissue. Specific chromophores absorb the scattered light, to give one example; in red blood cells, heme molecules inside the hemoglobin absorb visible light at 555 nm wavelength[81].

3. The energy brought by the photons to the tissue are converted into heat energy and by collisional/vibrational relaxation, this energy results in a localized temperature and pressure increase. If the pulse is short enough, this process happens very fast, and tissue will not find enough time for deformation and there will be not enough time for the density to change. The pressure increase in the tissue is named as *acoustic pressure distribution*.

4. Since the tissue is elastic, the pressure increase in the irradiated area cause an acoustic wave as an ultrasonic pulse to travel from the focal area to the

surrounding tissue. An array of ultrasound detectors can be used to detect this signal if placed onto the tissue surface.

5. By using the detected signal from the detector array and applying an image reconstruction algorithm, an image of the initial distribution of acoustic pressure can be achieved. This pressure distribution known as photoacoustic image.

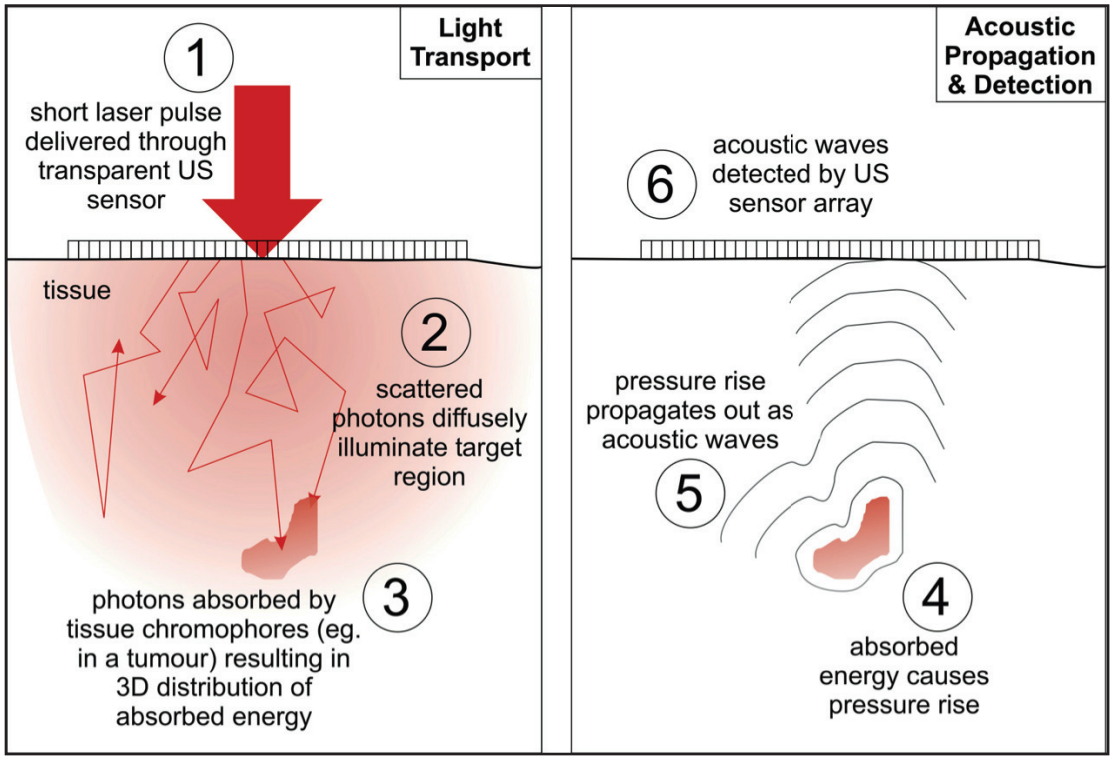


Figure 3.1: Schematic showing basic mechanisms for photoacoustic imaging

Since thermal diffusion takes time durations longer than the pulses used to form photoacoustic waves and the succeeding photoacoustic propagation intervals, generally it is omitted. Thus, energy deposition occurs with the following rate:

$$H(x,t) = \mu_a(x)\Phi(x)f(t) \tag{3.1}$$

Here $f(t)$ is the temporal pulse shape of the illumination source and it is normalized so that it has an integral equal to 1. We are interested in the total amount of energy that is deposited into the sample during the pulse duration, so we can define *density of absorbed energy* by:

$$H(x) = \int H(x,t)dt = \mu_a(x)\psi(x) \tag{3.2}$$

Here $\psi = \int \Phi dt$ is the integral of the fluence rate and it is known as *fluence*. There is a constant that is relating the density of the absorbed energy, H, with the distribution of the initial acoustic pressure, p_0, and it is a thermodynamic quantity named as *Grüneisen parameter*. Relation is given below;

$$p_0 = \Gamma H \tag{3.3}$$

3.2.3 Supercontinuum Generation

Supercontinuum generation is a method to convert relatively narrow spectral bandwidth laser light into light with very wide bandwidth and low temporal coherence. During this process, spatial coherence is usually preserved. This phenomenon was first observed in 1970 by Shapiro and Alfano [82, 83]. Desired spectral widening is frequently achieved by means of propagating a pulsed laser through a nonlinear media. To give one example, supercontinuum can be obtained by sending high pulse energy femtosecond pulses through a piece of glass. Another way to obtain the same broad spectrum is possible by propagating lower pulse energy pulses through an optical fiber. In this case, although the pulse energy is less, due to confined nature of the laser beam and longer length of optical fiber, the beam is exposed to much higher total nonlinearity while preserving high beam quality. Photonic crystal fibers are of particular interest since they can be manufactured to have high nonlinearity by adjusting their chromatic dispersion characteristics. By using modest level laser powers, very broad spectra light can be achieved using photonic crystal fibers as supercontinuum generation medium.

There are many important applications of broadband light source applications that supercontinua sources can be used for. Some of these applications are; fluorescence microscopy [84], coherence tomography [85], the characterization of optical materials [86], flow cytometry [87], optical fiber communication systems [88], frequency combs [89].

The physical mechanism of supercontinuum generation in optical fibers varies according to the parameters such as chromatic dispersion of the fiber, length of the fiber, the pulse width, input beam's peak power and wavelength. In case of the femtosecond pulses are used as the pump, the most dominant effect is self-phase modulation. When the self-phase modulation is used in combination with anomalous dispersion, it can lead to some complex soliton dynamics such as the separation of higher-order solitons into multiple main solitons. This process is called *soliton fission*. In the case of longer pulse pumping(picoseconds or nanoseconds), four-wave mixing and Raman scattering begin to take place in the process[90]. It is even shown that using continuous wave pulses, supercontinuum is achievable inside optical fibers. In order to obtain supercontinuum in this regime, lasers with multiple watts of power levels and long fiber lengths should be used to obtain Raman scattering and four-wave mixing[91].

Properties of the generated supercontinuum in terms of noise may vary significantly according to the parameter regions. For example, for the self-phase modulation dominant supercontinuum generation, if the dispersion is positive, the generation process is highly deterministic and the generated supercontinuum can have pulses that have high coherence despite of being highly broadened spectrally. For the cases comprising higher-order soliton effects, even very low-amplitude fluctuations can effect the generation process and cause the resulting supercontinuum pulses to be very noisy and vary significantly from pulse to pulse.

Although it has been decades since the first generation of supercontinuum, intensely nonlinear nature of it makes the comprehending the details of the process and calculating the underlying mechanism with analytical tools very hard. Thus, numerical analysis for propagation of such pulses (using special precautions due to very wide spectral bandwidth) is required to predict the outcome of the

supercontinuum processes.

3.3 Experimental Setup

The laser system that is built for photoacoustic signal generation is consisted of mainly three parts: Oscillator, two preamplifier stages with an AOM in between for repetition rate control and lastly, power amplifier with a PCF added to the end for supercontinuum generation. Here oscillator is the part that is generating nanosecond pulses that is amplified in the preamplifier part. AOM reduces the repetition rate of the pulses for amplification to higher power levels. Power amplifier is the part that main amplification takes place. PCF is added at the end of power amplifier to accomplish broadband spectrum via superontinuum generation. All these parts are examined in this section in detail:

3.3.1 Oscillator

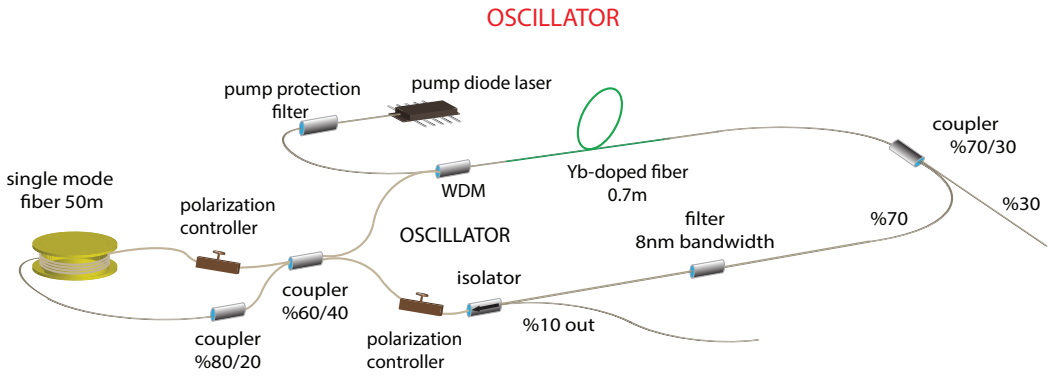


Figure 3.2: Schematic for the Oscillator Setup. WDM: Wavelength-division multiplexer.

The oscillator consists of a 0.7 m long Yb-doped fiber, followed by a %70 coupler, an 8 nm bandpass filter, an inline isolator to ensure unidirectional operation, an output coupler of %10, two polarization controllers, a 50 m long HI-1060 single mode fiber for Sagnac loop, and 2x2 %40 coupler for NOLM (non linear optical loop mirror)[92]. Although the oscillator can operate without the bandpass filter, it adjusts the central wavelength and improves stability. As a pump source, a fiber-coupled single-mode 980-nm diode laser delivering a maximum power of 650 mW is used. Pump-protection filter rejects unwanted backward propagating light within the fiber, if any, because light in the backward direction can cause laser diode to break down. The fundamental repetition rate of the cavity is 3.1 MHz and this repetition rate is decided by the fiber lengths used in the cavity. Polarization controllers are used manually in order to assist mode-locked operation of the laser. Part of the output is split with a %10 fiber which seeds the amplification stage with oscillations of 24 mW power and 8 nJ energy. Figure 3.2 shows the schematics of the oscillator setup.

3.3.2 Preamplifiers and AOM for Repetition Rate Control

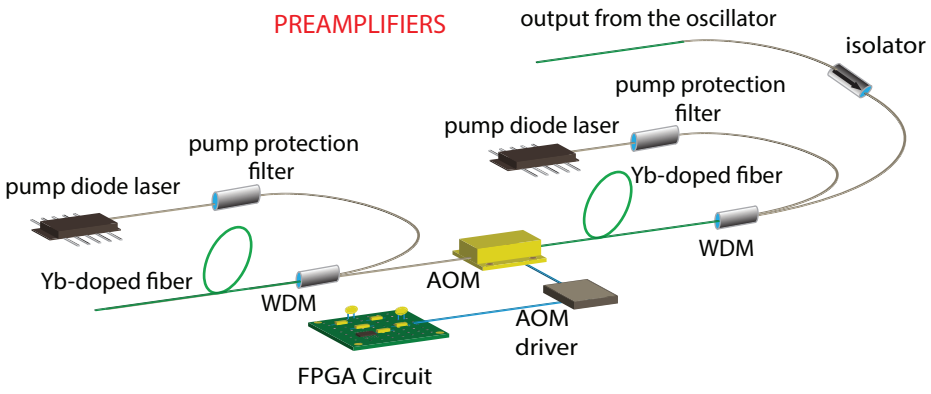


Figure 3.3: Schematic of the preamplifiers and AOM

Preamplifier comprises of 1.0 m long Yd doped fiber followed by a fiber-integrated acousto-optic modulator (AOM) that is connected to FPGA (field programmable gate array) circuit. Fiber-coupled single-mode 980 nm diode laser delivering a maximum power of 650 mW is used as pump source. The amplifier levels the signal up to 300 mW power that corresponds to 100 nJ energy. Using the acousto-optic modulator, pulse repetition frequency is reduced to 50 kHz, but for the safe operation for the amplified spontaneous emission to not to occur, frequency is held at 100 kHz. Complete control over the pulse train, including generation of non-uniform pulse trains, is achieved via the AOM through custom-developed field-programmable gate- array (FPGA) electronics explained below. Since the average power of the signal is also reduced by the reduced repetition rate in addition to the internal AOM loss and average power, to compensate these losses and prepare a signal that is enough high to saturate the power amplifier, another amplifier including 980 nm diode laser delivering a maximum power of 650 mW and 1.0 m long Yb-doped fiber is built. Using this amplifier, the obtained signal is 150 mW at 100 kHz repetition rate that corresponds to 1.5 μJ pulse energy. Figure 3.3 shows the schematics of the setup of the preamplifiers and AOM.

3.3.3 Power Amplifier and Supercontinuum Generation

A 105 μm core multimode fiber coupled 976 nm diode laser of delivering a maximum power of 10W is used as a pump source. The amplifier also includes 2 m long wide band double-clad Yb-doped fiber with 20 μm core diameter and numerical aperture of 0.07. The octagonal shaped cladding of the power amplifier has 125 μm diameter and numerical aperture of 0.46. Figure 3.4 shows the schematics of the final amplifier.

Power amplifier pump light is coupled to the gain fiber via an MPC (multpile pump combiner). The diode is temperature-stabilized to preserve the wavelength used to pump the gain fiber since the diode output wavelength is shifting with the changing temperature. Yb-doped fibers have a peak for absorption around

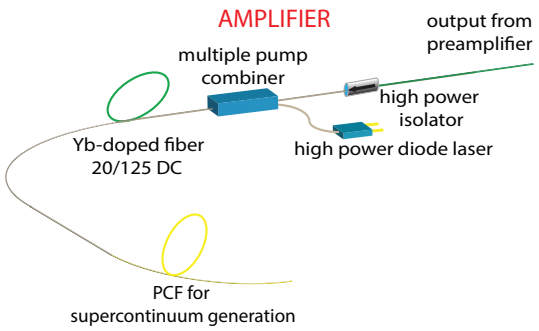


Figure 3.4: Schematic of the Power Amplifier and PCF for supercontinuum generation

976 nm wavelength and any shift that may occur results in the decrease of the absorption rate of the pump, consequently efficiency drop in amplification process. This may even cause the burning of the fiber or components in the amplifier since the unabsorbed pump may reach to high enough levels that the components are not suitable to operate for. The temperature stabilization is achieved via a PID controller-driven peltier heater that is attached to the surface of the pump diode.

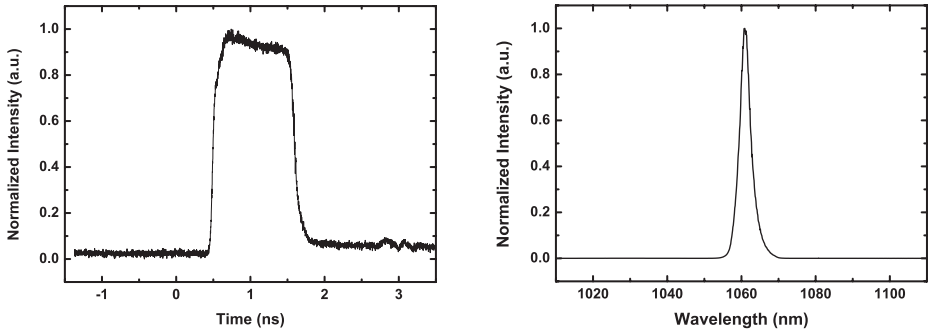


Figure 3.5: (a)Pulse duration and (b)optical spectrum of the laser at the input of PCF

The optical power can be increased up to 1.8 W and the protection of the

preamplifier from any backward propagating light is ensured by a high-power isolator placed between preamplifier output and MPC. Figure 3.5 shows the pulse duration and the optical spectrum of the laser before supercontinuum generation.

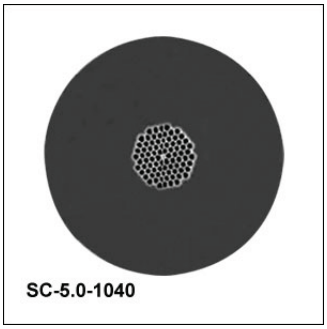


Figure 3.6: Photo of the cross-section of the PCF (NKT SC-5.0-1040) used for supercontinuum generation

A 3.5 meter long photonic crystal fiber is spliced to double-clad Yb-doped fiber of the final amplifier for supercontinuum generation. The power delivery between wide band fiber to photonic crystal fiber is around %35; thus, the output power is 600 mW corresponding to 6 μJ pulse energy. Nonlinear optical propagation is dramatically enhanced in a PCF due to its air silica honeycomb-like microstructure(Figure 3.6 and low core diameter(4.8 μm). The zero dispersion wavelength of the PCF is 1040 nm. As a result of non-linear effects, the spectrum broadens and supercontinuum between 600-1100 nm is generated. Figure 3.7a shows supercontinuum spectrum.

Figure 3.7b shows the light that seems yellow and dominantly red since the wavelengths in the supercontinuum correspond to that colors in the visible range of electromagnetic spectrum.

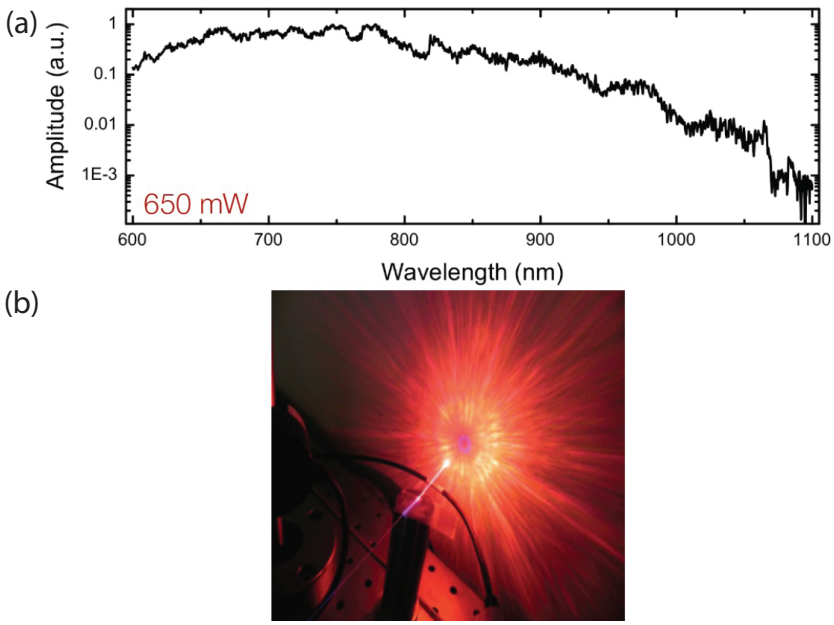


Figure 3.7: (a)Spectrum for the generated supercontinuum at the output of the PCF, (b) Photograph of the output of PCF clearly showing that the light is in the visible domain and have different wavelengths together

3.4 Photoacoustic Signal Results

Fiber laser output is focused onto a ceramic sample and generated photoacoustic signal is detected using a photoacoustic transducer. Since photoacoustic signals are absorbed in the air, sample and transducer are placed in a water tank. Transducer scanned the sample at different angles and generated photoacoustic signal is amplified in a low-noise amplifier and observed in oscilloscope. The sample was 10 cm away from the transducer and the detected signal is showing the same result(Figure 3.8).

The detection of photoacoustic signals from biological samples necessitates careful sample preparation and parameters of the laser such as wavelength, pulse duration and power should be adjusted differently according to the prepared

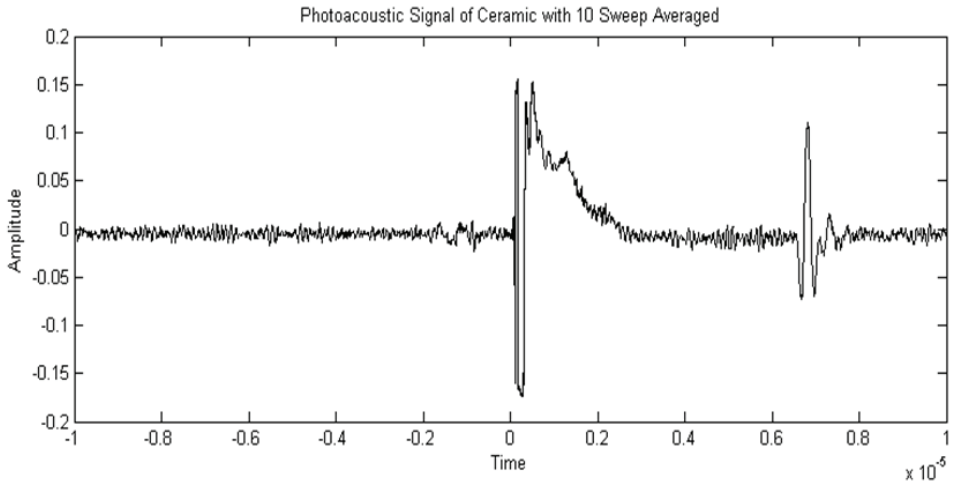


Figure 3.8: Photoacoustic signal detected from the ceramic signal

sample.

Figure 3.9 shows the total laser system integrated with acousto-optic tunable filter and galvo scanner.

3.5 Conclusion

Available lasers in the market have specific characteristics. Although, some have tunability over wavelength on the expense of energy, repetition frequency and pulse energy are usually constant. As a result of the constraints, lasers are chosen regarding the application. A laser suitable for melanoma cell detection with a wavelength of 1064 nm, e.g., is not appropriate for hemoglobin imaging since at the particular wavelength the absorption of hemoglobin is very low. Another laser with tunable wavelength may not be used for real time imaging because of having low PRF. Lasers having control over PRF, usually fiber lasers, have fixed wavelengths which is not suitable for spectroscopic measurements. Fixed energy obligates to perform microvasculature or cellular imaging. In this thesis, the

laser designed specifically for photoacoustics gives freedom to select wavelength between 600 nm and 1100 nm , energy between 2 nJ to 10 μJ, and repetition frequency between 50 kHz to 3 MHz; thus allows only one laser usage for many different applications. Using this laser system preliminary photoacoustic signal detection results are obtained on a ceramic sample and the studies are going on in Boğaziçi University to obtain photoacoustic images on biological samples.

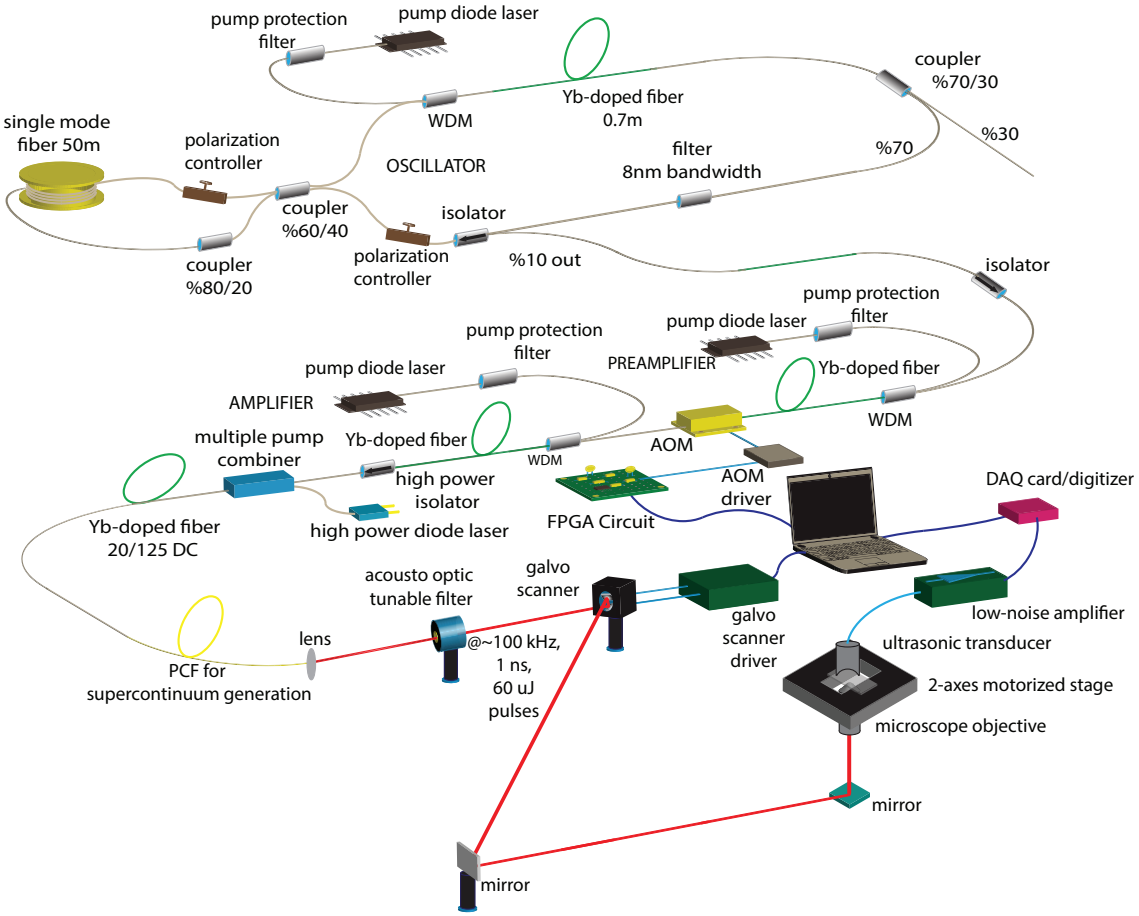


Figure 3.9: Schematic of the system to be integrated with galvo scanner system and photoacoustic tunable filter

Chapter 4

Femtosecond Fiber Laser Development for Terahertz Spectroscopy

4.1 Introduction

Scientists in terahertz (THz) wave technologies have benefited from the recent developments in ultrafast laser technologies and RF technologies and applied these new gained techniques into characterizing a wide variety of phenomena. Undoubtedly, the most successful of these applications has been in the development of time-domain terahertz spectroscopic and imaging systems which has been utilized in the characterization of dielectrics and semiconductors. This pulsed technique has allowed users to characterize dynamical behavior inside materials under illumination with picosecond resolution. Typically pump/probe or similar dynamical measurements require the use of amplified pulses derived from free-space solid state lasers in the μJ - mJ range and since interferometric techniques are typically used in pulsed measurements, the measurement time of a THz spectrum can last at least tens of minutes. Better systems can be realized

based on fiber laser technologies. Here we discuss the advantages of a THz spectrometer driven by an ultrafast Ytterbium-doped fiber laser whose repetition rate can be tuned rapidly allowing for rapid dynamical measurements. The efficient gain medium, robust operation and compact design of the system opens up the possibility of exploring rapid detection of various materials as well as studying dynamical behavior using the high brightness source.

4.2 THz-Time Domain Spectroscopy

Pump-probe spectroscopy is a valuable method to inspect fast events in metals and semiconductors on microscopic scales. In pump-probe experiments, many lasers in visible and infrared region are utilized to investigate material properties[93]. By the advances in the time-domain methods in the terahertz region such as THz time-domain spectroscopy(THz-TDS), far infrared region began to be utilized for these measurements. In order to achieve that, femtosecond laser pulses are used for excitation and THz pulses are used as probe signals to examine material properties in nanoscale materials[94]. The use of these techniques in this region where material architectures are formed by hollow gaps or huge areas of dielectric background amongst a rare presence of nanomaterial have driven system architectures that require special tools. Usually, these systems necessitate lasers that can generate high powers in order to yield a high number of carriers in the samples to alter probe characteristics.

For the first pump-probe systems that were used for terahertz generation, the same laser source was generating the pulse for both generation and detection of THz radiation in addition to excitation of the sample[95]. The general method to produce terahertz waves with broad spectral width is to use mode-locked lasers that can generate pulses less than 200 fs optical pulse width[95]. These femtosecond mode-locked lasers have generally pulse energies in the orders of nanojoules with pulse repetition rates around tens of MHzs. In order to generate terahertz pulses with required pulse energy using femtosecond pulses, these mode-locked lasers necessitates to be amplified to microjoules region [96]. However, most of

the lasers used for this purpose are big in size, costly, hard to operate and need external cooling systems such as chillers. When these systems are coupled to the already complex THz-TDS system, total system becomes extremely complex and hard to operate since there are many optical components need precise alignment. In addition, according to the scan type, two or three optical arms may be required and this will add more complexity to the overall system.

Since there has been significant processes in the development of mode-locked fiber lasers that can generate sub-200 fs pulses, these lasers become promising for more compact and less complex systems to be built. Mode-locked fiber lasers are also generating nJ level pulse energies with much simpler design comparing to bulky lasers that are used for THz pump-probe systems. In addition, the observed pulse to pulse jitter level for these passively mode-locked systems are better comparing to solid-state mode-locked femtosecond systems that generally use active components to obtain mode-locking [97]. The low-jitter property of fiber laser systems allow the use of pulses other than the fundamental pulse in the same pulse train to perform THz experiments [98]. Using this feature, all-fiber designs can be implemented to generate THz pulses. In these systems, both pump and probe generation can be done without need for free-space propagation and mechanical delay lines in order to use the same pulse for both purposes [99]. The required microjoule pulses can be achieved using the amplification of nanojoule-level pulses by using highly efficient fiber based amplifiers such as Yb-doped fibers that are easy to cool due to their double-clad structure, which simplifies the sytem more since they do not need cooler system based on chillers.

For the last 20 years, in order to characterize dynamic actions in nanomaterials, dielectrics and semiconductors, time resolved terahertz spectroscopy(TRTS) has become a crucial tool [100]. A common TRTS system based on Ti:sapph femtosecond laser system is given in Figure 4.1. In this system, in order to generate THz waves, photoconductive antenna (PCA) is used while detection is made using electro-optic sampling method. In this system, pump-probe measurement can be conducted either in transmission or reflection mode. In both cases the vital condition is that the excitation pulse and the THz probe pulse should be matched

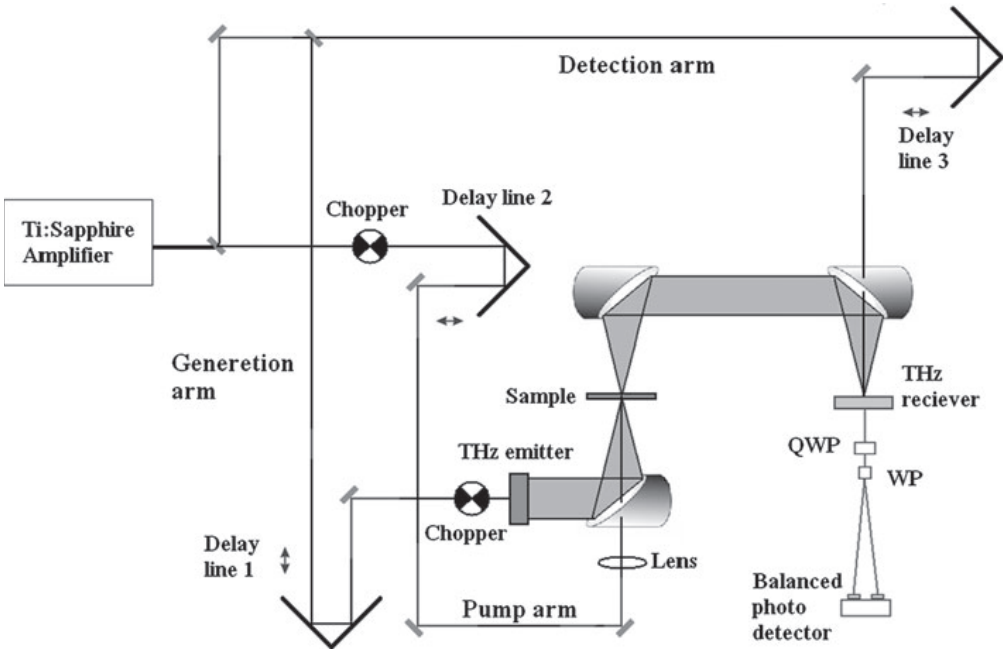


Figure 4.1: Schematic of a basic time resolved terahertz spectroscopy system based on Ti:sapphire laser

spatially and temporally. The THz region that should be covered in these measurements is typically between a few meV to 100 meV. This entire region should be covered in order to correctly characterize the material under photo-excitation. Usually frequency insensitive techniques are used for this aim since they are easier to implement. These techniques are based on scanning one pulse (either probe or pump pulse) over the other that is held fixed. These techniques are defined as 1D and 2D scan, respectively [95]. In 1D scan, while holding one arm fixed, the other arm is scanned. A 1D pump scan delivers valuable data about the average THz absorption by the material. In order to achieve 2D scan, a series of pump-probe delay times with THz difference is collected. Both of these techniques are shown in Table 4.1.

As it was mentioned earlier, microjoule level pulses are needed to generate sufficient number of carriers in the material to observe a significant alteration in the

Table 4.1: Scan Types

	1D Scan	2D Scan		
	Probe Scan	Pump Scan	1st Method	2nd Method
Pump	Fixed	Scanned	Fixed	Scanned (Synchronously)
Detection	Scanned	Fixed	Fixed	Scanned (Synchronously)
Generation	Fixed	Fixed	Scanned (in reverse)	Fixed

probe beam. Hence, it is necessary to amplify Yb-doped fiber lasers using a fiber amplifier especially for thin samples that the response is further reduced. Thus, another prerequisite for laser source as being stable with low jitter is revealed. In the recent years, techniques based on Yb-doped mode-locked fiber laser systems that are combined with nonlinear optical techniques in OPA configuration began to be used [101].

4.3 Fast Scan THz Detection Method:OSCAT

In conventional terahertz time-domain spectroscopy measurements, in order to measure THz profile of the pulses, time difference between generation and detection arms in THz spectroscopy system is measured [102]. This way of measurement may take up to tens of minutes depending on the length of the scan. As a result, environmental effects may affect the measurement. Thus, alternative methods are proposed to overcome this problem and shorten the length of measurement. One of these methods is asynchronous optical sampling method [103]. In this technique, two lasers that have repetition rates that are locked with an offset of $\Delta f = f_{rep1} - f_{rep2}$ are used. Instead of scanning with a mechanical delay line, one of the lasers cavity length is changed using a piezo and THz profile is measured. The biggest disadvantage of this method is that the requirement of two mode-locked femtosecond system that increases the overall complexity and price of the system. In addition, the control electronics to lock the repetition rates of the lasers are also sophisticated. This disadvantage pushed the researchers to

develop a new method named "Optical Sampling by Laser Cavity Tuning" (OSCAT) [98]. In this technique, one laser source is used, and the different pulses that are separated from the same source are superimposed by scanning the repetition rate of the fiber laser. It is principally shown in a THz spectrometer driven by a mode-locked Er-doped fiber laser [99]. Time difference between two pulses in this system can be given by:

$$\Delta\tau = i\left[\frac{1}{f_{ref}} - \frac{1}{(f_{ref}+\Delta f)}\right] \tag{4.1}$$

Here f is the repetition rate of the laser and Δf is the difference in repetition rate, $\Delta\tau$ is the time difference between pulses and i is the index number of the pulse. In order to obtain the wanted time delay, length difference between two arms can be calculated as:

$$l_{fiber} = \frac{\Delta\tau c_0(f_{ref}+\Delta f)}{\Delta f n} \tag{4.2}$$

Here l_{fiber} is the needed fiber length in one arm, c_0 is the light speed and n is the refractive index of the medium [99]. Using this technique, the expected data acquisition time can be as low as a minute for a THz waveform with at least 100 ps long.

The OSCAT method applied TRTS design is given in Figure 4.2. Using this system it is possible to make the measurements as required by the 2D pump-probe scan technique for either fixed pump pulse arrival derived from the detection pulse arm of the system (1st method in Table 4.1) or synchronous scanning of detection and pump arms for fixed generation (2nd method in Table 4.1). For both cases the measurements can be done using OSCAT method by adjustment of t, time difference between generation and pump pulses, using mechanical stage.

A new technique enables scientist to conduct experiments without external scan lines. Optical sampling by cavity tuning technique is able to be achieved by tuning the repetition rate of the laser source in order to create a time delay

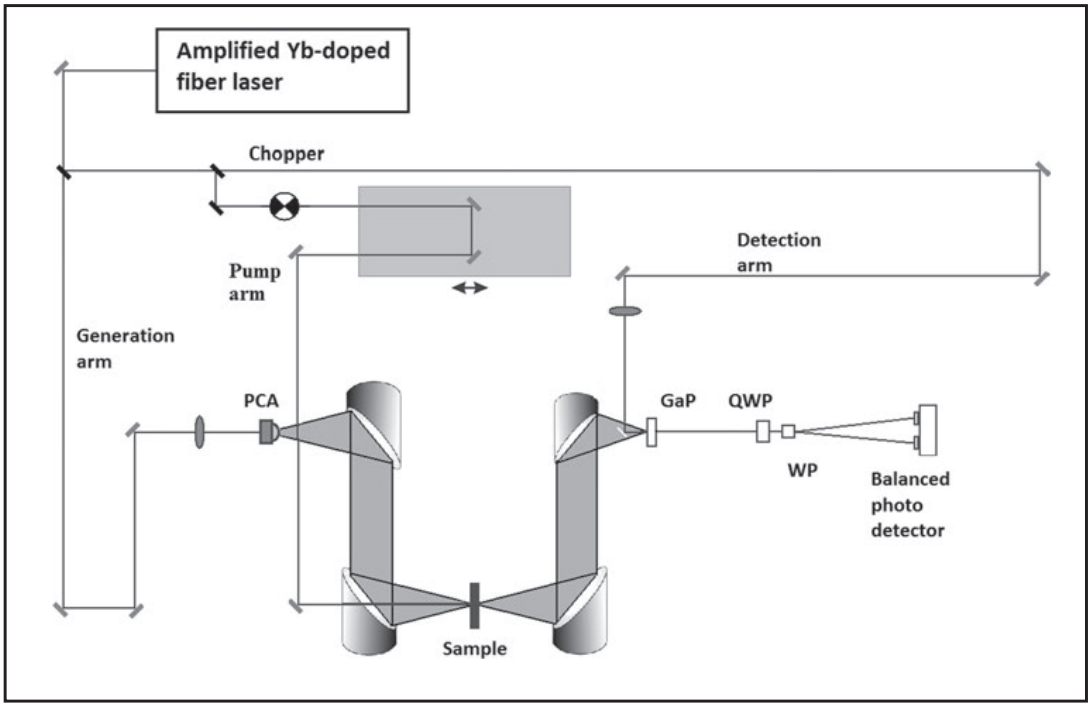


Figure 4.2: Schematic of a time resolved terahertz spectroscopy system based on fiber laser

between two outputs of the laser with different optical lengths as shown in Figure 4.3. After pulse i is divided into two arms, pulses in second path travel an extra path length of l_d in time, t_d. In order to create a time delay of Δt between paths, repetition rate of the laser is tuned and the second arm is shifted more with respect to the first arm.

However this technique is developed with an Er-doped fiber laser which has an inefficient gain medium compared to Yb-doped fiber laser. In this thesis study, repetition-rate tuning of Yb-doped fiber oscillator is studied[104]. Theoretical analysis is same in both cases. Assuming that the second path has more pulses as number of a at repetition rate of f_{rep}, the time delay between pulses in the first path i and second path $i + a$ is given by:

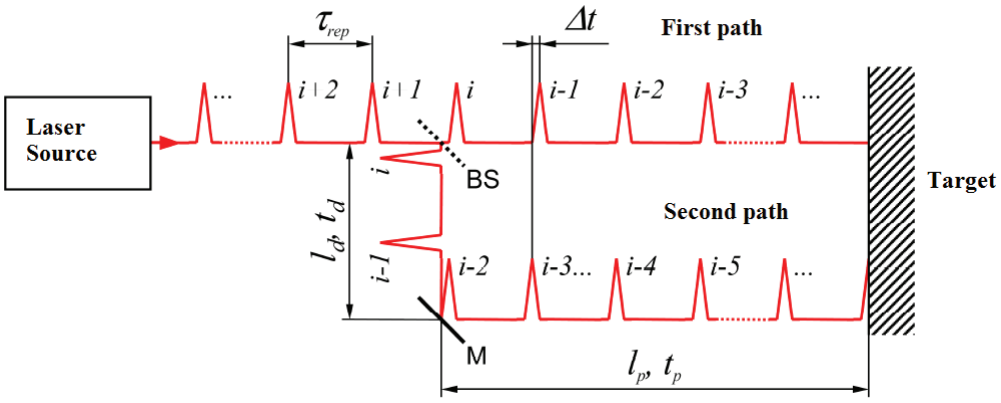


Figure 4.3: Schematic for the OSCAT system

$$\Delta t = t_d - a \cdot \tau_{rep} \tag{4.3}$$

where $\tau_{rep} = \frac{1}{f_{rep}}$. Desired total time scan range can be calculated as:

$$\Delta t_{range} = \Delta t_{max} - \Delta t_{min} = a \left(\frac{1}{f_{min}} - \frac{1}{f_{max}} \right) \tag{4.4}$$

where minimum and maximum repetition rates scanned are, f_{min}, f_{max} respectively. Corresponding length difference for desired scan range can be calculated with pulse number a as:

$$l_d = \frac{a \cdot c_0}{f_{min} \cdot n} \tag{4.5}$$

where c_0 is speed of light and n is refractive index of medium pulses are guided in.

4.4 Fiber Laser Results

4.4.1 Laser Setup

The oscillator of the laser system is pumped by a laser diode operating at 976 nm wavelength. In order to prevent possible damages caused by any back reflection that may occur in the system, the laser diode is protected via an SPLP. WDM combines and transmits the pump and the signal to the highly doped Yb-gain fiber which has core diameter of 4 μm. The active fiber has a numerical aperture (NA) of 0.14, and absorption value of 1200 dB/m at 976 nm pump wavelength. At the end side of the gain fiber, a fiber coupler (with coupling ratio of % 80 to %20) is put in order to form an optional output to construct a fiber amplifier. Free space part of the oscillator is starting with a collimator and includes wave plates as NPE components. It ends with another collimator in the other end.

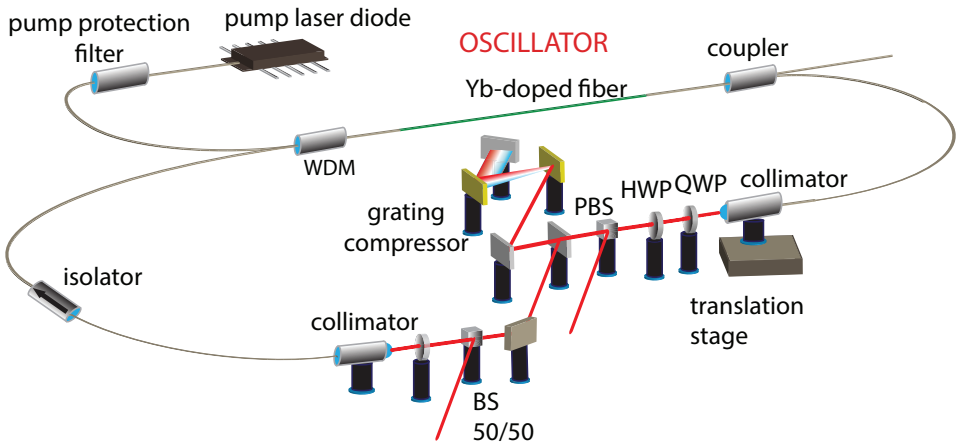


Figure 4.4: Schematic of the oscillator. QWP: quarter-wave plate; HWP: half-wave plate; BS: beam splitter; PBS: polarizing beam splitter

In fiber ring cavities, usually a separate polarizing beam splitter (PBS) is used

to support nonlinear polarization and extract the undesired polarization components to the outside of the cavity. However, in our design, since we are also using a free-space isolator that makes the pulses to propagate in only one direction, which also contains a PBS that transmits the horizontal polarization and eliminates the vertical polarization, we decided to remove the extra PBS from the system and simplify the free-space part of the cavity. Laser oscillator is designed such that the total group velocity dispersion of the cavity is equal to nearly zero. The reason of choosing such a design was to obtain pulse widths as short as possible by acquiring as much optical bandwidth as we can while preserving a stable mode-lock. In order to achieve that, oscillator is designed such that the dispersion caused by the fiber is compensated by a negative dispersion grating pair. For the THz measurement system that will be developed on necessitates 50 MHz of repetition rate. Hence, total fiber length and free-space part including the grating pair is calculated accordingly. According to the calculations total fiber length is estimated to be 310 cm and free-space part is calculated to be 88 cm, while a dispersion grating pair is used with 5.7 cm distance from each other. For this case, total group velocity dispersion caused by the fiber is found to be 80600 fs^2 and the negative dispersion due to grating pair is found as -80370 fs^2. Here fiber group velocity dispersion (GVD) is assumed to be 26 fs^2/mm and grating pair have GVD of -1410 fs^2/mm. Using these values, total dispersion of the cavity is calculated to be nearly zero (230 fs^2). Second collimator that is at the end side of the free space port is placed onto a translation stage to obtain tunability in repetition rate by changing the total cavity length.

The desired tunability range is calculated as follows; According to Equation 4.5, scan range of time depends on, repetition rate of laser, laser tuning range and length of passive delay line. According to this formula, calculated OSCAT parameters of Yb-doped fiber laser oscillator are given in Table 4.2.

The output from the oscillator is taken using two output ports; one of them is via a beam splitter just after PBS as free-space port, and the other one is from the coupler at the output of the gain fiber. An additional output coupler with a ratio of %95 to %5 is placed after the collimator for diagnostic purpose. The power measured from the output ports are 33 mW and 40 mW, which corresponds

Table 4.2: Calculated OSCAT parameters

$f_{REP}(MHz)$	50
$\Delta f(kHz)$	50
$\Delta\tau(ps)$	100
Step size (ps)	0.1
Cavity length (m)	6
Scan length (mm)	6
Pulse index (i)	5,005
$l_{fiber}(m)$	20,02

to 0.65 nJ and 0.8 nJ respectively from free space and fiber ports. The output taken from the BS is coupled to a collimator with polarization maintaining fiber. All of the fibers from this point on are chosen as PM fibers. The aim of this is to preserve the polarization of the already-polarized light coming out of the oscillator and reduce the losses at the output of the pre-amplifier while dechirping the pulses via a grating pair that are highly polarization dependent. Pre-amplifier fiber lengths are chosen such that the pulse evolution will mimic the behavior in fiber part of the oscillator and hence obtain the shortest pulse possible [105]. Thus, the pre-amplifier is realized as shown in Figure 4.5. At the end of the fiber amplifier a grating pair with negative GVD is placed to compensate the positive GVD caused by the fibers. The laser characterization and the parameters that are achieved are given in the next part.

4.4.2 Laser Characterization

In order to measure ultrashort pulses generated from the oscillator and amplifier systems, in temporal domain, intensity autocorrelation technique is used. Traditionally, two QWPs, one HWP and a PBS are used to achieve mode-locking condition by nonlinear polarization evolution (NPE) technique. It is known from NPE technique that, PBS eliminates the less intense off-center wavelengths by rejecting the vertical polarization of oscillation beams leading the pulse to shorten with every round-trip of pulses. Generally, this output is used for amplification

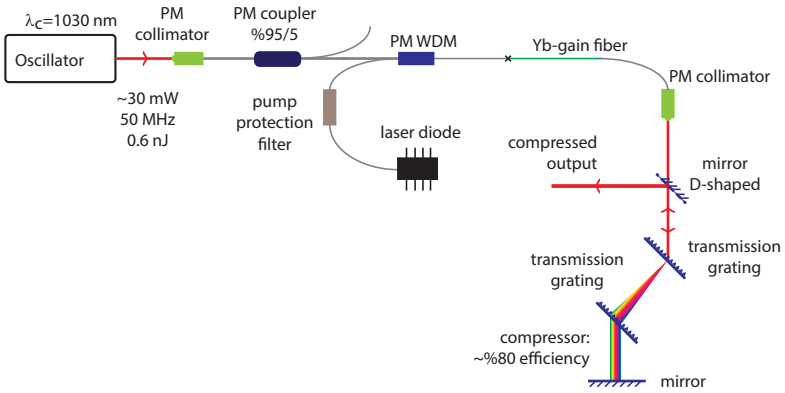


Figure 4.5: Schematic of the preamplifier of the fiber laser based THz spectroscopy system

in the preamplifier part. However, shorter pulse durations can be achieved by using another free space output from oscillator according to our simulations. Using a non-polarizing beam splitter right after transmission gratings, shorter pulse widths are possible comparing to PBS output. After gratings, pulses become negatively chirped due to dispersion and coupled to the fiber through collimator. Material dispersion of silica causes pulses to be positively chirped. This cycle achieves a certain point at which pulses can be compressed to shortest possible pulse duration. This region is calculated to be within just after the gain medium of the oscillator. When pre-amplifier design mimics the oscillator design (gratings followed by Yb-doped fiber and succeding fiber region) including components and fiber length, BS output from oscillator delivers most compressible pulses to the pre-amplifier. Additionally, PBS is extracted from system because bulk isolator is functional only for horizontal polarization. In other words, it rejects vertical polarization similar to PBS.

Using the two free-space ports from PBS and BS, pulse widths are measured using intensity autocorrelation technique. In this study, for both oscillator and pre-amplifier output autocorrelation measurements, Femtochrome FR-103MN Rapid

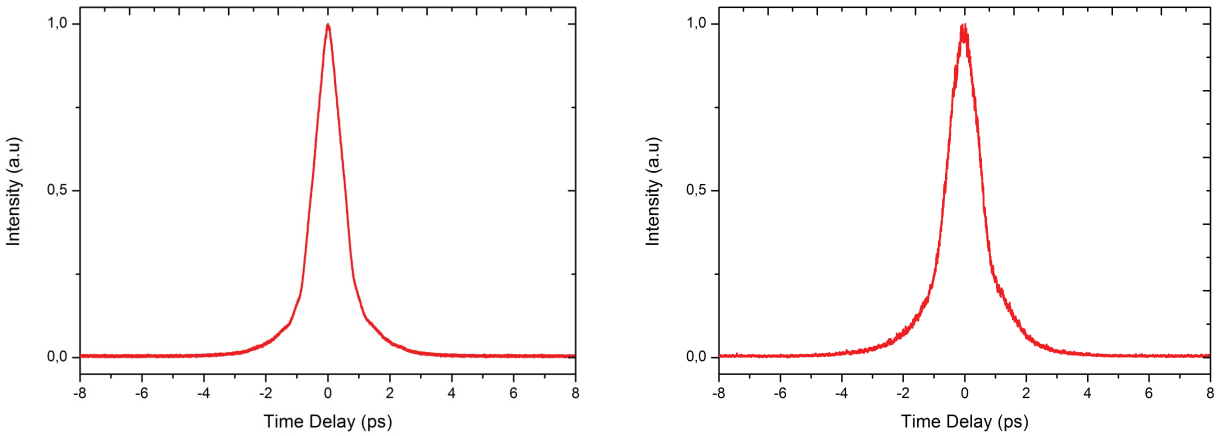


Figure 4.6: Autocorrelation of the outputs from BS port (left) and PBS port (right). Both of the pulses are directly measured, hence they are uncompressed

Scanning Autocorrelator is used. The autocorrelation traces obtained from PBS and BS is given in Figure 4.6. Assuming that the pulses generated from the oscillator are in Gaussian shape and applying the corresponding correction factors, uncompressed and directly measured pulses from the PBS and BS ports are comparable and measured as 1.20 ps and 1.09 ps respectively. Simulation results for pulse duration also shows that the oscillator delivers 1.07 ps pulses from BS output which is verified by the experimental results.

If the pulses inside laser cavity have too much energy, wave-breaking occurs due to Kerr nonlinearity and in some cases mode-locked state survives by simultaneous division of the pulse energy to the multiple pulses that are propagating in the cavity synchronously. Such a situation is undesired since this behavior is not highly controllable, and repetition rate may differ during the operation of the laser that may result in permanent damage to different parts of fibers and fiber components. This behavior can be avoided by keeping the pulse energies lower than the threshold levels for pulse breaking to occur in any part of the cavity. This energy threshold is around 4-5 nJ for laser oscillators like the ones used in this study. In our laser, we characterized the pulses using photodiode, autocorrelator

and RF spectrum analyzer and did not observe multiple pulsing in the operating region.

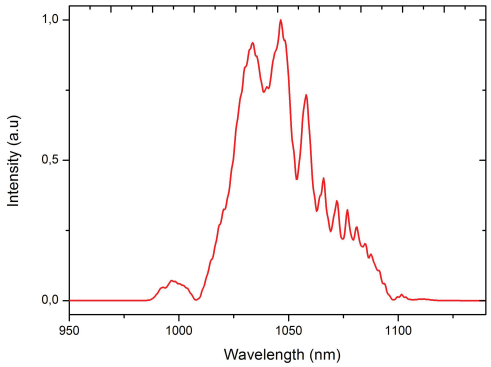


Figure 4.7: Spectrum graph taken from the output from PBS after coupling to the PM collimator

Spectrums that are measured from %5 and %20 ports are given in Figure 4.8. The output from PBS port was measured to be 30 mW and when it is coupled into the PM collimator of the pre-amplifier input, power measurement is done again and 15 mW of power is measured which corresponds to nearly %50 coupling efficiency. Coupled spectrum is also altered slightly due to filtering caused by the collimator and the bandwidth is reduced to nearly 35 nm(Figure 4.7).

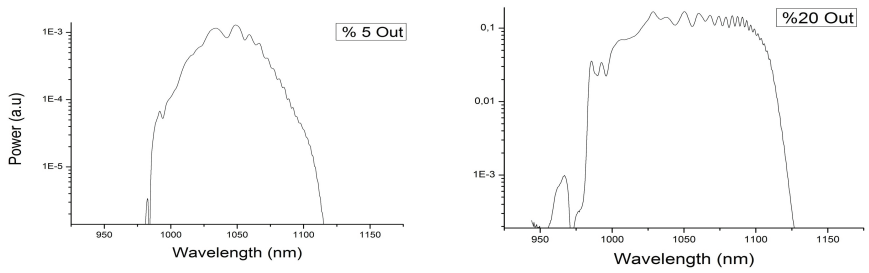


Figure 4.8: Spectrum graphs taken from the outputs at different locations of the laser oscillator from the fiber coupler outputs

In order to apply the scanning system for the oscillator to the OSCAT technique, mode-lock state should be preserved while changing the repetition rate and meanwhile pulse duration deviations should be minimum. For this purpose, the stability of the oscillator is checked by tuning the repetition rate for the entire THz range, which corresponds to 6 mm of translation stage movement. The repetition rate is characterized using an RF spectrum analyzer for the entire scan range and given in Figure 4.9a.

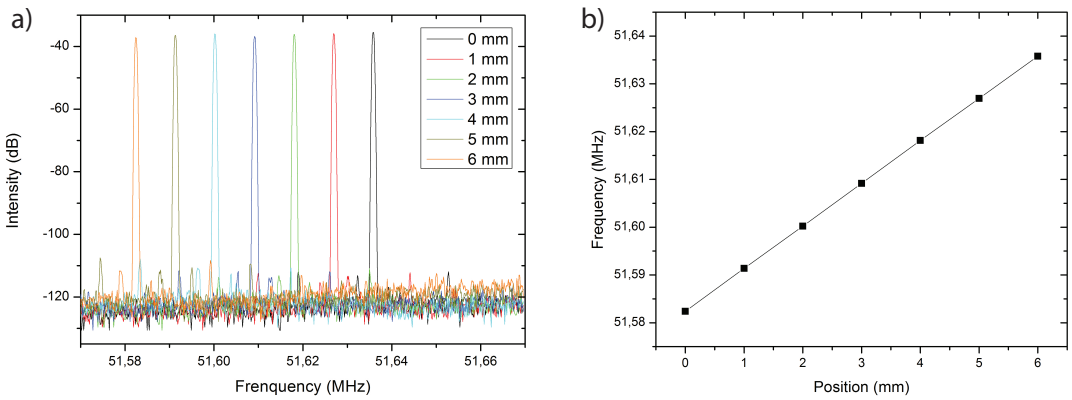


Figure 4.9: a) RF spectrum data showing the repetition rate values for different positions of the translation stage that is moving the collimator b) Graph showing the linear relation between the translation stage position and the repetition rate of the oscillator

The central repetition rate is measured to be 51.58 MHz which is close to the theoretical value. The reason of the difference is anticipated to be due to miscalculations at splice points where the fibers are shortened and the displacements in free space part while adjusting the laser to obtain mode-lock. Around this repetition rate, tunability of 53.4 kHz is accomplished. As it can be seen there is a difference between measured and calculated repetition rate tunability range, which is approximately % 6. The reason of this difference is manual translation stage that is used to move collimator of the oscillator. Even small errors in micrometer adjustment may cause large repetition shifts.

For the case of OSCAT technique, these shifts can be compensated by changing the scanning steps and range of the scan. For instance, instead of scanning all the THz range of 6 mm by small steps like 6 μm, THz profile can be obtained using shorter scan range corresponding to 53.4 kHz since the scan length is inversely proportional to the repetition rate (Equation 4.5). Repetition rate results in Figure 4.9a are illustrated in another graph to observe the linear change of frequency with the changing repetition rate(Figure 4.9b).

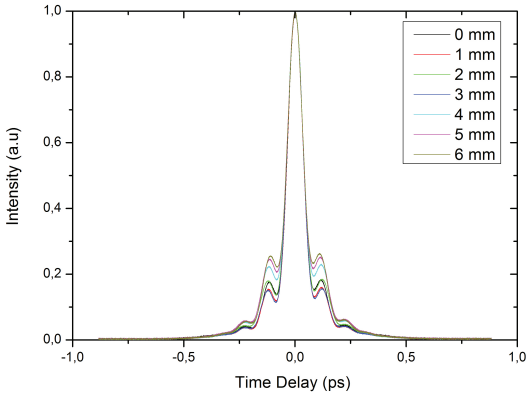


Figure 4.10: Graph showing the variation of pulse duration with the translation stage position

It can be seen from Figure 4.9b that, for 6 mm scan range that is divided into 1 mm of steps, oscillator central repetition rate of 51.58 MHz is changing by 8.9 kHz with every step in a linear manner.

For these scan points and range, pulse durations for compressed pulses at the output of the preamplifier are also measured for 90 mW of average power. The traces' amplitudes are normalized and plotted together in Figure 4.10. Although a slight difference between first and the final position traces, pulse width variance is less than %4 and the total stability of the system is quite good. The measured pulse durations for the first and last positions are 85 fs and 82 fs respectively with Gaussian pulse estimation.

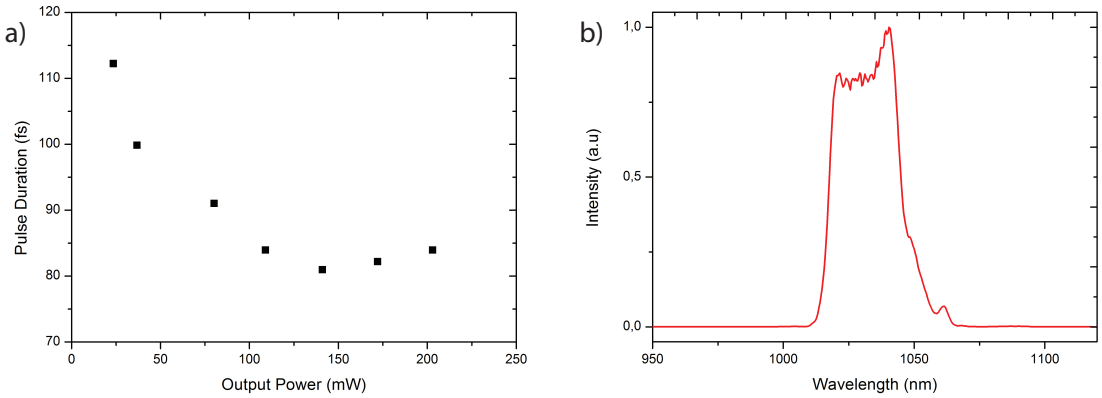


Figure 4.11: a) Pulse duration variation by changing the output power of the amplifier, b) The spectrum data taken from the output of the amplifier system

Another characterization made on the pre-amplifier system is the variation of the pulse duration according to the pre-amplifier output power. Pulse durations at different power values can be found in Figure 4.11a. It is clear that up to some point pulses are getting shorter due to self-phase modulation caused by Kerr effect, but after some point, in this case around 200 mW, gain narrowing begins to dominate the process, causing the spectrum to shrink and pulse durations to get longer.

The laser amplifier output spectrum is given in Figure 4.11b. The acquired data shows that the output has a central wavelength of 1031 nm and a width of 30 nm and these values don't change significantly during the scan process. Power characterization of the amplifier is done by measuring the amplifier output signal power as a function of amplifier pump power. By applying a pump power of 400 mW, over 200 mW of average power at the output is observed which is usual since the operating repetition rate is well above the values of efficiency decreasing effect of amplified spontaneous emission which is observable around 100 kHz and less. According to the measured output powers and corresponding applied pump powers, a conversion efficiency of % 65 is achieved(Figure 4.12a).

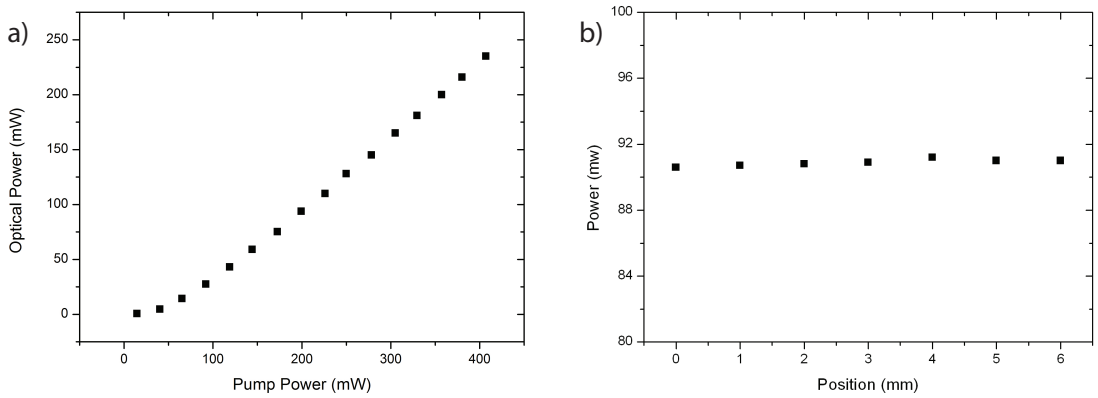


Figure 4.12: a) The amplifier pump power and obtained signal power, b) Graph showing the fluctuation of the amplifier power by changing the translation stage position at the operating power for spectroscopy measurement

Measured amplifier output power by changing the cavity length is also measured and the total power fluctuation in this scan range is found to be less than %1 (Figure 4.12b). This parameter is crucial since the pre-amplifier output is used as a source for THz-TDS system and in an ideal system the pulses should be identical.

Last stability test was made on the pulse duration variation in long time periods. For five hours with one hour steps, average power and pulse durations are measured and no visible change is observed.

4.5 THz-TDS Measurements at Different repetition Rates of the Fiber Laser

Schematic representation of the THz-TDS system integrated to the fiber laser is shown in Figure 4.13.

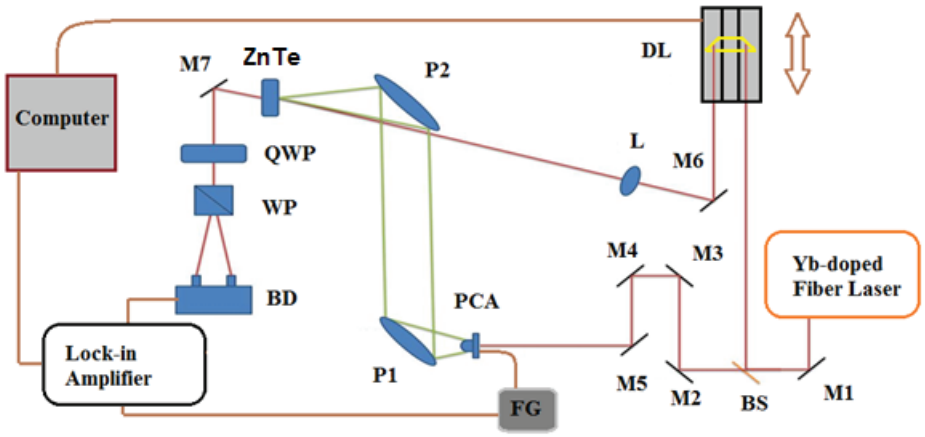


Figure 4.13: THz-TDS system integrated to the fiber laser. P1-P2: Off-axis parabolic mirrors, FG: Function generator, M1-M5: Mirror, BS: Beam splitter, PCA: Batop PCA-40-05-10-1060-h antenna, DL: Delay line consisting of corner cube on translation stage, L: Lens with focal length 300 mm, ZnTe: <110 >cut ZnTe crystal, QWP: Achromatic quarter wave plate for 700-1100 nm, WP: Wollaston prism, BD: New Focus 2307 balanced photo receiver, Lock-in amplifier: Stanford Research System SR830 Lock-in Amplifier

Ultrashort pulses from Yb-doped fiber laser are divided into two optical arms consisting of generation (pump) and detection (probe) arms. Both arms start from the beam splitter and end at EO crystal. Optical distances between these two components for both arms are equal to each other. Generation arm consists of BS, M2-M5, OL, PCA, FG, P1 and P2. BS, DL, M6, L form probe arm. ZnTe, M7, QWP, WP, BD and lock-in amplifier were used for data collection and data were recorded by computer.

Firstly, the system displayed in Figure 4.13 was tested with Ti:Al2O3 laser at 780 nm central wavelength in order to achieve equal length of generation and detection arm. After this condition was met, the system is modified for 1031 nm central wavelength of Yb-doped fiber laser. First one is to maintain a linearly polarized light before beam splitter (BS). Although PM components are used

in pre-amplifier part, to eliminate orthogonal polarization components, combination of half wave plate and polarizing beam splitter (PBS) was used. Transmitted light from PBS was horizontally polarized. Therefore, photoconductive antenna is placed according to this orientation. Mirrors used were broadband dielectric mirrors that work for 1031 nm. Mirror 6, 7 and corner cube were metallic mirrors. 35 mW after PBS were distributed 26 mW to 6.6 mW by BS for generation and detection arms respectively. Hence, no filter was needed to attenuate arms not to damage PCA and balanced photo detector. Detection arm focusing lens were changed to a lens with suitable coating for 1031 nm to reduce losses. Both GaP and ZnTe crystals can be used in electro-optic detection. Signal power is proportional to crystal thickness while broader bandwidth can be achieved with GaP for about 1 μm wavelength [106]. One of the main challenges was the collimation of pre-amplifier since the beam diameter arriving to PCA was directly dependent on the collimation quality. PCA has a maximum acceptable beam diameter of 5 mm. In the experimental setup we constructed, due to long distances the beam traveled, beam diameter exceeded 5 mm; therefore, all of the beam that came on to the PCA was not able to be coupled into the dipole structure. In order to prevent this loss, an additional lens with low-strength focusing (focal length of 175 cm) is used to couple all light into the PCA. Our main limitation was that a silicon based balanced photo detector is used in detection arm. For wavelengths longer than 1 μm, the response of detector decreases greatly. This can be improved by two ways. An InGaAs based balanced detector can be used for higher response. Second way is that antenna-antenna system can be constructed to overcome detector handicap. In this method, bandwidth would be limited to antenna characteristics. In modified PCA-ZnTe crystal THz-TDS system, three measurements are carried for three different repetition rates in order to observe the stability of THz generation. THz signals of these measurements are given in Figure 4.14.

Fourier transformations of these signals are displayed in Figure 4.14d in order to compare spectrum stability of measurements.

According to measurements, a high signal-to-noise ratio could not be achieved. The slight change in THz signal and power spectrum can be observed. However,

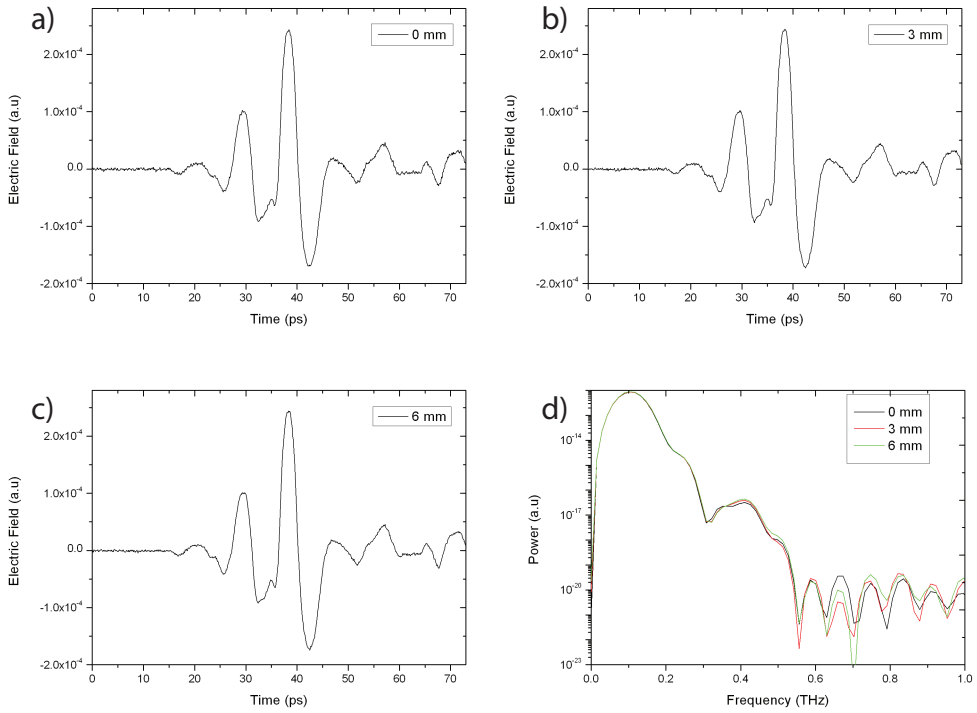


Figure 4.14: THz signal for a) 0 mm, b) 3 mm, c) 6 mm oscillator scan stage position. d) Power spectra of the THz signals for different scan stage position

first position corresponds to between second and last measurement. Thus, it can be deduced that the change in THz signals and power spectrum is caused by low signal-to-noise ratio and not the repetition rate tuning.

4.6 Conclusion

In this study, the development of a THz-TDS system driven by a novel Yb-doped fiber laser whose repetition rate can be tuned is discussed specifically for fast scan THz measurements. Traditionally THz-TDS systems use linear stages adjusting the time delay between generation and detection arms. This interferometric process usually takes more than ten minutes due to integration

times. Several techniques are developed to accelerate this process. The main goal of this study is to build Yb-doped fiber oscillator that can be used in OSCAT technique as an alternative method for fast scan THz measurements. To support this idea, stability of oscillator is examined in terms of power, spectrum and pulse duration at different repetition rates of laser. Afterwards, THz waveforms at different rep-rates are measured for additional verification.

The oscillator built for this purpose delivers pulses at average power of 15 mW at central wavelength of 1042 nm with 35 nm bandwidth at 51 MHz. Repetition rate tuning of oscillator is examined to observe the stability of laser. According to calculated OSCAT parameters, scanning 6 mm of oscillator tuned repetition rate of about 53 kHz over about 51.6 MHz. Repetition rate is changed linearly at each 1 mm tuning step. This tuning range can cover over 100 ps time window in OSCAT/THz-TDS measurements. Afterwards, pre-amplifier part is studied in terms of pulse duration, spectrum and power stability. Pre-amplifier delivers over 90 mW at the central wavelength of 1031 nm. Power fluctuation with rep-rate tuning is lower than %1 with %4 change in pulse duration over about 82 fs. These results are lower than the OSCAT with Er-doped fiber laser that was previously realized[98]. According to these parameters, great dynamic range can be achieved with an optimized THz-TDS system.

In the final part of the study, the laser that is built is applied to the spectroscopy. The spectroscopy system has bandwidth about 0.1 to 0.5 THz. Signal to noise ratio is about 60. THz waveform measurement is repeated for different repetition rates of Yb-doped fiber oscillator in order to study this system for OSCAT technique in terms of stability. Cavity length of oscillator is altered 6 mm to tune repetition rate about 50 kHz over 51 MHz. Although THz waveform and power spectrum changes at each oscillator scan position, an optimized system can achieve better results. In order to upgrade system, an InGaAs balanced detector can be implemented instead of silicon based detector. Another solution to response problem for 1 *mum* wavelength is to modify system to antenna generation-antenna detection system. Therefore, there will not be a need for balanced detector. The studies on these issues are going on in METU that we have collaborated with for the laser system development and integration to the

spectroscopy system.

In conclusion, stability of Yb-doped fiber laser shows that the system can be used in OSCAT technique as source to scan the THz waveform without the use of any external delay lines. However, THz-TDS measurements should be improved by necessary improvements in spectrometer as mentioned earlier. In OSCAT, the data acquisition is based on a novel method where the laser cavity repetition rate is tuned over the entire THz waveform thereby shortening the data acquisition times throughout the measurements. The oscillator for the amplified Yb-doped fiber laser system was constructed with a repetition rate of 51 MHz. For OSCAT technique, additional pre-amplifier system with a passive delay line should be constructed. To scan a length of 100 ps the cavity needs to be tuned over 25 kHz, for which the laser system exhibited little or no difference in output pulse duration, power and spectrum characteristics which is a testament to the stability of these lasers compared to other solid-state mode-locked lasers. Using this technique, scan times of obtaining one THz waveform for THz-TDS measurements is less than one minute.

Additionally, the importance of this system is that, Yb-doped fiber lasers can be amplified to sub-millijoule pulse energies more easily than other types of fiber lasers. Coupled with measurement techniques developed in OSCAT technique, an amplified Yb-doped fiber laser driven THz-TDS system can perform pump/probe measurements in a more compact and robust design. This will allow for rapid measurements of THz pulse profiled which will be essential for scanning the entire THz waveform through the excited sample, a technique commonly referred to as 2D-scan excite/THz probe measurements.

Chapter 5

Femtosecond Fiber Laser System Development for Glass Processing

5.1 Introduction

Glass is an amazing material with diverse areas of application in the modern society, ranging from architecture to smart phones. This versatility owes to the fascinating material properties of glass, bringing together a high bandgap for transparency over the entire visible range and beyond, excellent thermal and mechanical durability, chemical stability, among others. However, the same properties render processing of glass challenging, e.g., while it has great tensile strength, glass is brittle. Consequently, the history of techniques to process glass is as rich as the history of its applications. In the present day, laser-based techniques offer the most precise ways of processing glass. The most straightforward approach relies on use of single-photon absorption in wavelength ranges where glass is not highly transparent, either in the IR or the UV[107]. However, direct absorption leads to certain problems, including undesirable thermal effects and formation of heat-affected zones, which can seriously compromise mechanical stability by

seeding micro crack propagation. Furthermore, processing substantially below the surface, towards creation of 3D structures requires use of wavelengths of high transparency. While nanosecond-pulsed lasers can be used to create sub-surface structures in glass, the physical mechanisms involved also impose limitations to the finesse of the micromachining and can also cause microcracks. In recent years, an exciting alternative has become practical enough for industrial usage, namely, the use of ultrafast lasers, producing sub-picosecond pulses in near-infrared wavelengths[108]. In this approach, ultrashort pulses are focused tightly into the bulk of glass or its surface, with power densities instantaneously exceeding terawatts per square-cm, triggering exotic processes such as simultaneous absorption of multiple photons, avalanche and impact ionization, resulting in a highly localized disruption of the glass matrix with very little energy deposited (few microjoules or even less). Due to the very modest amounts energy used per pulse, the thermal effects to the region even immediately surrounding the focal volume can be kept negligible. This approach is often called "cold ablation" and enables creation of extremely precise 3D structures. The development of user-friendly, low-cost microjoule-range ultrafast fiber lasers is now transforming this technique from a niche application to a widely adopted industrial processing tool, from product authentication to glass cutting, to creation of sub-surface optical waveguides. In this part of the thesis study, an overview of the basic mechanisms of cold ablation will be given and a fiber laser-galvo scanner system that has been built[109] will be explained in detail.

5.2 Theoretical Background

Glass is a transparent and solid-like material with diverse areas of applications in our daily lives. It is a boundless material whose applications diversity is relentlessly growing and which is more and more finding use in combination with other materials for high-tech applications. Glass is made from excessively found materials such as soda ash, limestone and sand. These materials are melted at very high temperatures (around 1500 °C) so that it behaves like liquid and can be poured, blown, press and molded into plenty of forms. However at ambient

temperature it acts like solids and becomes much harder to process after cooling due to changes in mechanical properties.

Glass have some unique capabilities that none of the other materials have all together. It has fascinating optical properties such as reflecting, bending, transmitting and absorbing light and has high bandgap for transparency over the entire visible range and beyond. Chemically it is corrosion-resistant and inert for most of the chemicals so that it can be used as a container for most of the chemicals. Thermally and electrically it is an excellent insulator. Mechanically glass surface is hard so that it is scratch and abrasion resistant and in the recent years with various methods it even gained elasticity. However, the same properties render processing of glass challenging, e.g., while it has great tensile strength, glass is brittle.

Consequently, the history of methods to treat glass is as rich as the history of its applications. Glass producing has an ancient tradition which dates back to around 3500 BC. It is assumed to have been first artificially manufactured in Mesopotamia and Egypt to be used as jewelry and afterward as jugs. Since then processes have continuously evolved from workmanship to todays high-tech industrial methods and the numerous of glass types and uses have emerged. Even though the manufacturing of it has a pretty long history, processes made on the already-produced glass is limited to last few decades due to brittleness of it. Breaking and disintegrating of glass commonly begins with a small crack. After the crack forms in some part of the body, it travels and reach the edge and causing it to break. This brittle nature of glass makes it hard to process. On the other hand, the developing technology necessitates smaller and smaller structures to be formed in different types of glasses in many application areas. There are conventional precise methods like photolithography and electron beam lithography that can process glass too, but both of these techniques are expensive and hard to operate especially on large areas. In the present day, laser-based techniques offer the most precise ways of processing glass. The most straightforward approach relies on the use of single-photon absorption in wavelength ranges where glass is not highly transparent, either in the IR or the UV.

However, direct absorption leads to particular problems, including undesirable thermal effects and formation of heat-affected zones, which can severely compromise mechanical stability by seeding micro crack propagation. Furthermore, processing substantially below the surface, towards the creation of 3D structures requires use of wavelengths of high transparency. While nanosecond-pulsed lasers can be used to create sub-surface structures in glass, the physical mechanisms involved also impose limitations to the finesse of the micromachining and can also cause micro cracks.

In recent years, an exciting alternative has become practical enough for industrial usage, namely, the use of ultrafast lasers, producing sub-picosecond pulses in near-infrared wavelengths. In this approach, ultrashort pulses are focused tightly into the bulk of glass or its surface, with power densities instantaneously exceeding terawatts per square-cm, triggering exotic processes such as simultaneous absorption of multiple photons, avalanche and impact ionization, resulting in a highly localized disruption of the glass matrix with very little energy deposited (few microjoules or even less). Due to the very modest amounts energy used per pulse, the thermal effects to the region even immediately surrounding the focal volume can be kept negligible. This approach is often called cold ablation and enables creation of extremely precise 3D structures. Micromachining via femtosecond laser of transparent materials has distinctive advantages over other micromachining techniques. First, laser induced modifications are limited to the focal volume due to nonlinearity in absorption mechanism. Using scanning methods or sample translation micromachining geometrically difficult structures in three dimensions becomes possible. Second, material-independent nonlinear absorption process makes it possible to form fine structures like optical devices in transparent materials.

Femtosecond laser micromachining arises from a phenomenon called laser-induced optical break-down. In this process optical energy of the femtosecond laser is transferred to the processed material, exciting many electrons and causing them to ionize, after that transferring energy to the lattice. Subsequently, a structural or phase alteration in the material occurs and causes a permanent refractive index modification or even may leave a void just at the focal spot. Understanding

why ultrafast pulses are ideal for micromachining necessitates approaching the problem from timescale of the material processing point of view. The damage caused by the laser has been studied for long, but there are vital differences between damage caused by femtosecond pulsed laser and damage caused by pulses with a duration greater than picoseconds. In most of the materials phonons, that are the main reasons of thermal effects, need at least one picosecond of laser exposure to be excited and for femtosecond laser pulses exposure duration is lower than this limit. Hence, any ions will not be excited thermally by electrons since the femtosecond pulses would end before this time period. Heat diffusion outside, even in the vicinity, of the focal area is minimum that results in an increase at the precision of process. In addition, femtosecond laser material processing is highly deterministic since the seed electrons to seed the absorption process are generated through nonlinear ionization mechanism and no defect electrons in the material are not required. The repeatability and confinement of the nonlinear excitation empower the use of the femtosecond laser- micromachining for practical purposes that the other methods are not capable[110]. Until the recent years, usage of ultra-short pulses on glass was a known but not widely used method since the pulse energy needs for this process is relatively high and the only lasers that were providing these pulse energy levels were solid-state lasers that are complex, not reliable, hard to operate and expensive. Following the improvement at fiber laser technology at the last few years, fiber lasers have also begun to provide these pulse energy levels with short pulses and high beam quality and have become an important alternative for solid-state lasers. In addition fiber lasers are cheaper, more compact, more reliable and easier to operate since they are alignment-free. The development of user-friendly, low-cost microjoule-range ultrafast fiber lasers is now transforming this technique from a niche application to a widely adopted industrial processing tool, from product authentication to glass cutting, to creation of sub-surface optical waveguides.

5.2.1 Ultrashort Pulse-Transparent Material Interaction

As we have mentioned in the second chapter, when we focus an intense femtosecond light tightly into the bulk of a transparent material, the obtained intensity value just at the focal spot is so high that a nonlinear absorption process begins[111]. This nonlinear field ionization (in combination of multiphoton absorption and tunneling ionization) leads to avalanche ionization. This nonlinear absorption is followed by an electron-ion plasma occurrence at the focal volume. When the plasma recombines, and it dissipates its energy to the surrounding area, permanent structural damage occurs at the focal spot. Using this nonlinear absorption mechanism, energy can be deposited into the bulk material without affecting the surface that makes it possible to form 3D structures inside such materials by just focusing and scanning the sample.

Until now, using femtosecond lasers, three different permanent structural formation have been induced inside bulk transparent material. These are; isotropic refractive index change[112], birefringent refractive index change[113] and voids[114]. These structures depend mainly on the intensity at the focal volume and may vary according to the laser parameters like pulse duration, wavelength, pulse energy and material parameters such as thermal expansion coefficient, bandgap, etc. However, for the case of tightly focused (for example using a 0.65 N.A. objective) short femtosecond pulses (~100 fs), in fused silica, all of the mentioned structural formation types can be induced by just changing the pulse energy. The schematic showing these different mechanisms are given in Figure 5.1 [115].

The isotropic refractive index change is observed near localized melting threshold levels and is explained with localized melting and rapid resolidification of the material[116]. In fused silica, both the density and the refractive index are higher for heated and cooled (in other saying quenched) material[117]. Infrared spectroscopy measurements taken from such quenched fused silica samples indicate densification showing an alteration in Si-O-Si bonding scheme[118]. Another proof of this is demonstrated by several groups that have written waveguides

inside glass by just applying femtosecond laser and translating it causing a refractive index increase in the irradiated area[119]. In fused silica, it is possible to obtain this isotropic refractive index change by applying 40-150 nJ pulses at 800 nm wavelength with 100-fs pulses and using a 0.65 N.A. objective.

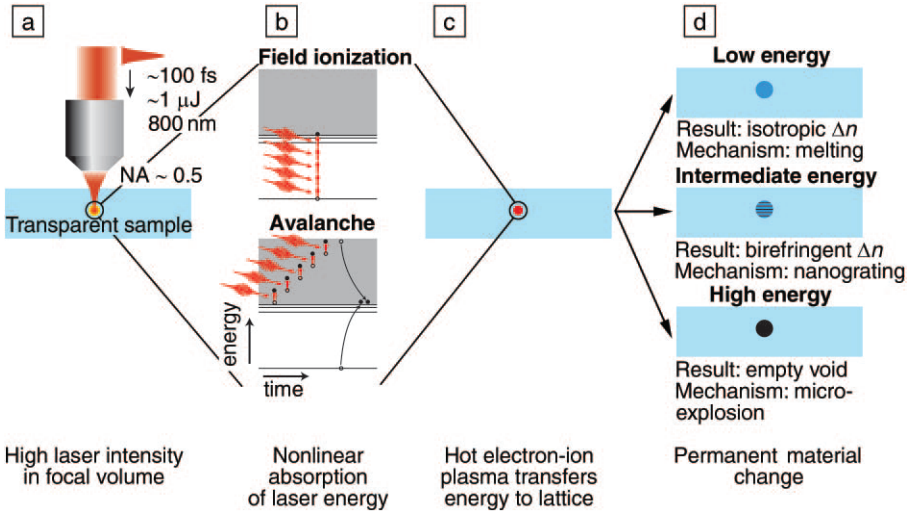


Figure 5.1: Schematic illustration of key steps in femtosecond-laser-induced structural change in bulk transparent materials. (a)(c) A hot electron-ion plasma is formed in the focal volume through nonlinear absorption of intense femtosecond laser pulses. (d) Depending on the amount of energy contained in the plasma, three different types of structural change can occur: isotropic refractive index change at low energy, birefringent refractive index change at intermediate energy, or void formation at high energy

Using the same parameters but by just increasing the pulse energy to the levels of 150 nJ to 500 nJ, another mechanism takes place inside glass forming birefringent refractive index change[113]. At these levels, Shimotsuma et al. observed that, nanometer-sized stripes are formed inside glass that have orientation perpendicular to the laser beam polarization[120]. These stripes were formed of alternating-density material layers such that at high-density parts the material density is slightly higher than normal material but at lower density areas the density was much lower than the normal density. These nanometer scale density changes that are alternating are named as "nanograting" and caused birefringence in the material[121]. It is also shown that these lower-density stripes can

be etched using hydrofluoric acid (HF) by 300 times faster comparing to unmodified material, which also indicates a structural change in the material[122]. The effect proposed to explain the mechanism of this periodic structure is the interference between the femtosecond laser beam and the electric field of the induced plasma on the material. This interference is leading to the periodic modulation of the surface[120].

When the pulse energy further increased above 500 nJ with the same parameters, voids occur inside bulk transparent material. The generation of voids is related to the explosive expansion of highly excited, vaporized material to the surrounding material around the focal volume, which is also called as "microexplosion" [123]. Since the expansion and the following microexplosion occurs inside the material, after the explosion a hollow or less dense core with densified shell of material is formed[124].

There are also some other processes that are known to occur during structural changes in the bulk of the transparent material by femtosecond laser. One example is forming E' color centers(positively charged oxygen vacancies) inside fused silica[125]. These formations do not make a major contribution to the refractive index change and when the materials with such formations are annealed thermally, these defects are eliminated and the material returns to the original state[119].

5.2.2 Applications of Ultrafast Laser Glass Processing

Surface texturing and roughening using ultra short pulses is a widely used method for especially metals since control over the process and precision provides amazing results and enables many applications such as biomedical implant roughening to increase cell adhesion, thin film etching for LED and solar cell efficiency increment, etc. Common methods like sand blasting and chemical etching for surface texturing on glass surface provides moderate level precision and nearly no control over the obtained pattern and often causes micro cracks that reduces the durability of the processed glass. Hence fiber lasers began to find usage in surface

texturing of glass, especially for the applications like hydrophobic/hydrophilic glass surface producing. The treatments made using ultra short pulsed lasers have shown that it is possible to get same or even better quality wettability conditions on glass surface in the last few years and they are highly promising for the future for surface treatment applications since they provide total control over the process pattern on surface which makes it possible to optimize liquid-glass interaction.

Another encouraging application for ultra-short pulsed fiber laser is laser welding of glasses. Widely used method to stick two glasses together are gluing them via some chemicals. Biggest drawback of this method is most of the chemicals used as glues are releasing some gases in time causing the power of bond between glasses reduce due to gas in between. Another method used is to polish the glass surfaces, bringing them together and treating with heat afterward. This method also have shortcomings especially if two different types of glasses are used since they may have different heat-expansion coefficients, causing the bond in between becomes weak after heat treatment. In recent years, high repetition rate (MHz) and high pulse energy (micro joule) level ultra-short laser pulsed lasers have begun to be used for welding of glasses. When the ultra-short pulses are focused at the interface of two glasses to be brought together, very small volumes from each glasses melt and cool-down together which results in very powerful bond between two glasses. With correct optimization of ultra-short laser welding process it is possible to obtain bonds as powerful as the glasses themselves.

Other application especially important for photonic and optic industry is writing waveguides inside glass in order to guide light in 3D which is possible only via ultra-short pulses. When ultra-short pulses are focused inside glass, a refractive index change occurs at the focal volume and this change is generally in the way of an increase in the index. By scanning the glass using a translation stage, this increased-index region can be used to form paths. Similar to the optical fibers working principle, light can be guided through these paths by using the total internal reflection mechanism. Using this method it is possible to guide and transfer light in three dimensions from one place to another, combining or separating different wavelengths of light, making grating or lens structures inside glass,etc.

Thus ultra-short laser waveguide writing inside glass is vital since it is expected that photonics technology is going to dominate communication, biomedical and sensor technology that is mainly provided by electronics technology currently.

5.3 Results

The laser system that is built for glass processing is given in this section. The laser system is consisted of a fiber laser oscillator that is generating the pulses, a pre-amplifier that is amplfying the pulses, an AOM, a backward pumping amplifier, a compressor and a galvo scanner-translation stage system[109]. These components of the laser system is examined in detail below:

5.3.1 Laser Setup

The system scheme is given in Figure 5.2.

The system's laser part consists of four main parts; oscillator, preamplifier, power amplifier and compressor. System's oscillator is an ANDi laser oscillator which is generating 120 fs pulses at 22 MHz. Filtering is achieved via a 10 nm bandwidth birefringent filter between two polarizers (polarizing beam splitter and free space isolator). Mode-locking is initiated and stabilized by nonlinear polarization evolution. Oscillator output power is 80 mW, which corresponds to nearly 4 nJ pulses. Output of the laser is taken from NPE port which has a polarized output. There is no extra couplers after gain fiber which cause a reduce in losses and make the system more stable. Pulses acquired from the PBS are centered at 1037 nm with a spectral width of 15 nm (Figure 5.4a). There is a %5 coupling port after second collimator and this port is used for triggering an FPGA circuit to drive an acousto-optic modulator. Oscillators figure is given in Fig 5.3.

Output of the oscillator is coupled into a collimator with an efficiency around

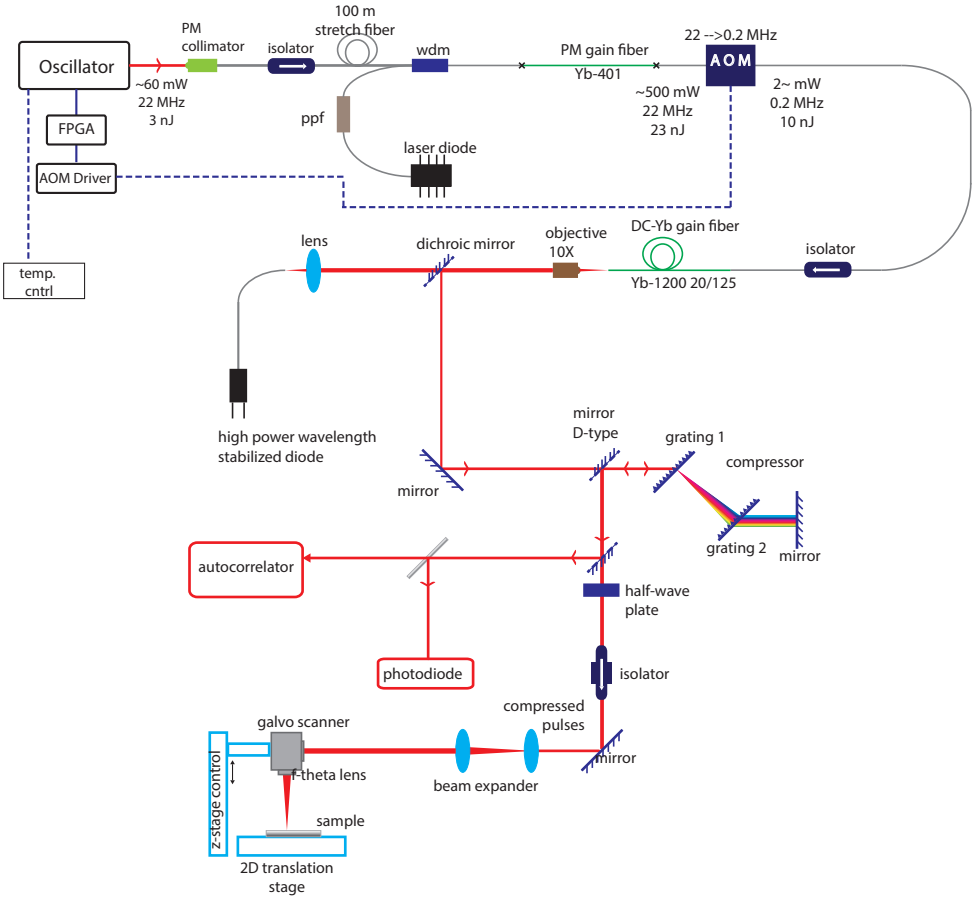


Figure 5.2: Schematic of the system built for glass processing

%75. It goes through an isolator which protects laser oscillator from possible back reflections from the succeeding amplifier stages. Then the pulses go through a 100 meters of passive of fiber to broaden the pulses in the temporal domain, so that they will have less peak power and will be ready for amplification to higher pulse energies without significant nonlinearity. At the output of stretcher pulses become around 55 ps. After this stage comes the preamplifier and it amplifies the pulses up to 450 mW, which corresponds to 20 nJ. Spectrum data for preamplifier output is given in Figure 5.4b.

Amplified pulses go through an acousto optic modulator and their repetition

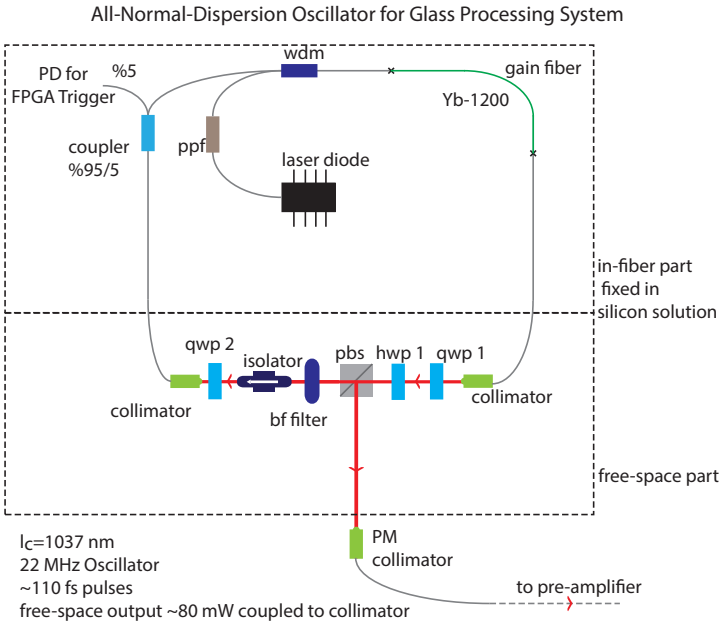


Figure 5.3: Schematic of the oscillator seeding the glass processing laser system

rate is either reduced to a uniform value of 200 kHz or bursts of pulses are produced at 50 kHz (Fig 5.5b) in a fiber-coupled acousto-optic modulator (AOM). The AOM is controlled by a special FPGA-based (SPARTAN 3E, Xilinx) electronic circuitry developed in house for synchronous pulse picking, burst formation and acts as a master controller for the entire system.

At the power amplifier stage, the setup consists of a 10-W pump diode stabilized to 976 nm by temperature control (with a deviation of %2 pump power), a short section of double-clad highly doped Yb gain fiber with core diameter of 20 μm, cladding of 125 μm and optics for backward pumping (Yb1200- 20/125DC-PM, Liekki). This configuration minimizes the nonlinear effects. Nearly %75 of the pump power is coupled into the gain fiber with a collimating lens of 25 mm focal length and a 10x objective. Amplified signal is extracted via a dichroic mirror which transmits the pump and rejects the signal wavelengths. The spectrum

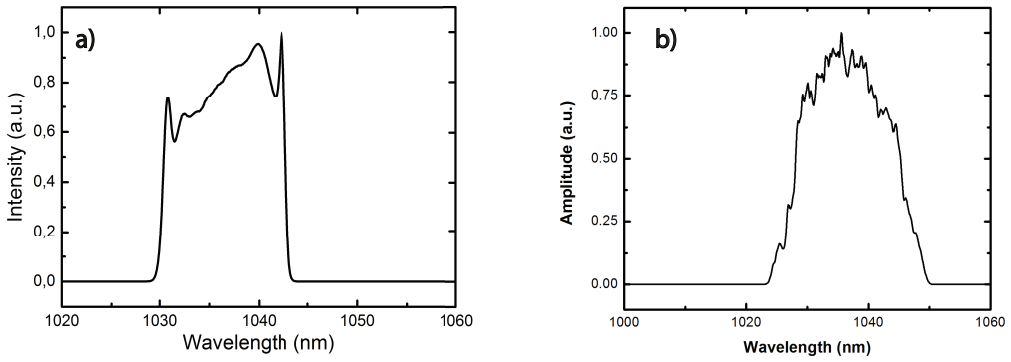


Figure 5.4: Spectrum graphs for a) Oscillator PBS port, b) Preamplifier output

of the amplified signal is given in Figure 5.5a.

We used numerical simulations to guide the experimental design. The details of the simulations can be found in [126]. The simulations predict pulse duration of 200 fs for 8 μJ shown in Figure 5.5c. The retrieved pulse form (Figure 5.5d) from measured autocorrelation and spectrum with PICASO algorithm [127], indicates around 300 fs FWHM. This result is in close agreement with the simulation, while the effective pulse width of 375 fs of the retrieved pulse reflects the effect of the pedestal caused by the interaction of uncompensated third order dispersion and nonlinearity. Even higher pulse energies (up to 40 μJ) can be generated, but result in longer pulses due to increased nonlinear phase accumulation and are not considered here.

Following dechirping, a high-power isolator is placed to prevent back reflections from the target. The optimized transmission of the compressor, half-wave plate and polarizing isolator (which allows continuous reduction of power and an isolation of 50 dB) is %80. The beam is then expanded with a telescope to completely fill the aperture of a 2D galvanometer scanner (ScanCube 14, ScanLab). The scanner focuses the beam with an f-theta objective, which ensures a constant spot size within a plane. The spot diameter is estimated to be around 8 μm, which is confirmed by directly observing craters formed after a raster scan

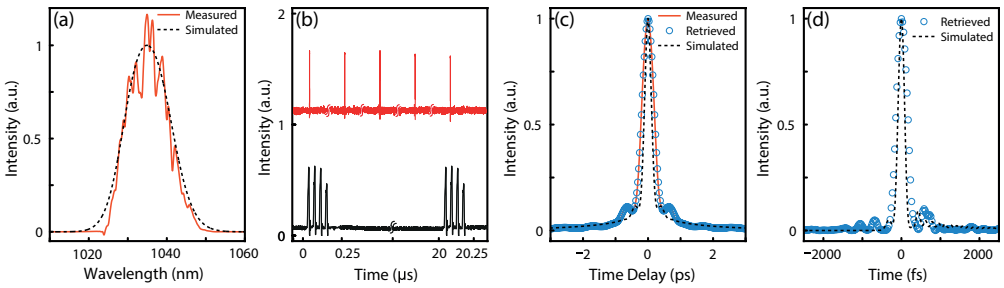


Figure 5.5: Measured temporal profile of 200 kHz pulses and 4-pulsed bursts that are generated via acousto-optic modulator driven by FPGA circuit

on the surface of a copper plate via reflection microscope and independently by the knife-edge method. The target sample is positioned on a motorized 3D stage, which allows translation by 10 cm in 3 axes. This translation stage is synchronized with the galvo-scanner such that 10 x 10 cm area can be scanned by just using the galvo scanner interface without a need for manual intervention.

In order to control the whole system, output ports for diagnostic purposes are added to the system after each section (oscillator, preamplifier, AOM and compressor). We have developed an electronic system such that every section is turned on after previous sections are checked and made sure that they are working correctly. In case some part of the system have a problem, all the following sections are turned off immediately, so that a possible damage due to noise amplification is being prevented since the biggest problem in these kind of systems is ASE amplification in gain fibers related to the lack of signal from the previous sections. Electronic system controlling the repetition rate of the laser system is given in Figure 5.6.

5.3.2 Glass Processing Results

Using this laser system some processes on glass were made in order to see the capability of the setup. To process the glass a scan system was needed. So we

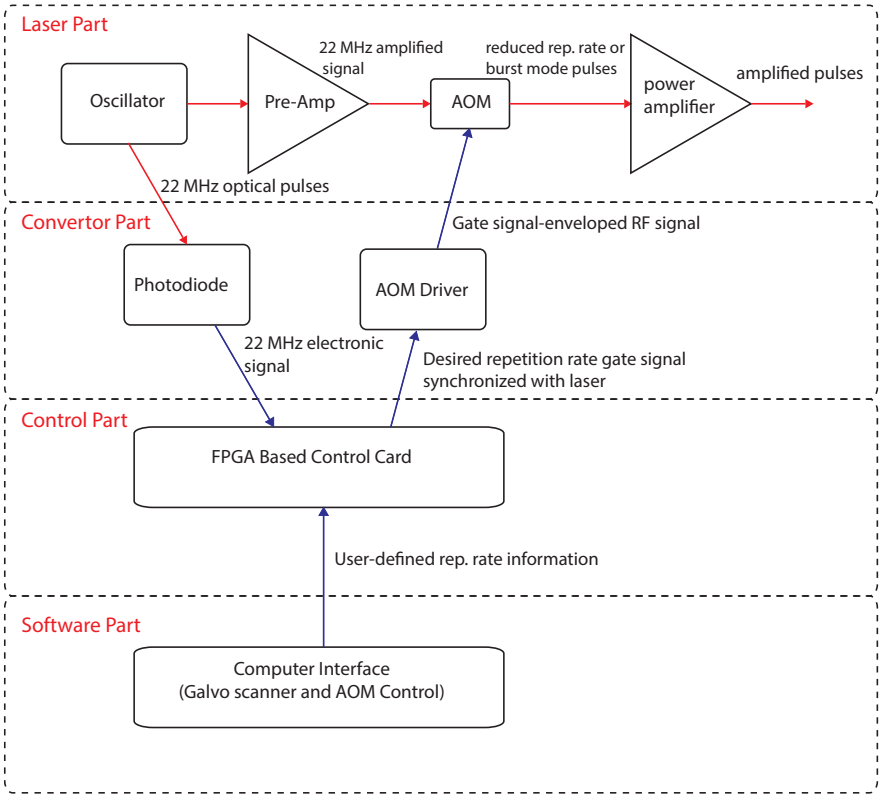


Figure 5.6: Schematic for the electronic system controlling the repetition rate of the system

have integrated a galvo scanner to the system to make process on glass. Galvo scanner has a clear aperture of 12 mm, so we have used a beam expander to increase the beam diameter at the input of scanner. Beam expander's expansion ratio is 1:3, which increased 4 mm diameter laser output beam to 12 mm, so that it will fill all the aperture to get minimum spot size on sample. We used a 56 mm focusing f-theta lens, providing around 6-8 μm beam at the sample on a plane surface of around 10 mm. To examine the beam diameter we have scanned a glass sample with the focused beam such that there will be only one pulse per spot, which corresponds to 1000 mm/s scanning speed even in the case we have 5 μm spot size. We have measured the sample using a known scale which has lines

at every 10 μm. We also used knife-edge technique to understand beam spot size by using a thin edge non-transparent razor and scanning it along the beam. By taking power measurements after the razor we have formed different spot sizes along the optical axis. By Gaussian beam approximation we have calculated that the spot size is slightly less than 10 μm.



Figure 5.7: Photo of the processed glass, alexandrite and quartz samples using femtosecond pulses

Using this laser output and scanner system, we have made some processes on glass. By focusing the beam onto the surface we ablated the surface and made some markings on the surface. By continuous scanning of the same area we were able to make clean cuts and shapes around 5 mm size on 180 μm thick microscope cover glass. Total process per shape took less than 15 minutes. Using this process, threshold for the ablation of glass is measured as 40 TW/cm^2. Photo of the processed glass sample is given in Figure 5.7. In addition to glass we have also managed to make process on glass like materials such as alexandrite and quartz. They are also given in Figure 5.7.

Instead of focusing the laser onto the surface, we have focused it into glass and scanned lines with 10 μm distance to form a square area. We have observed a pehenomenon which is called photodarkening in literature. With different scan speeds and different pulse energies, obtained photodarkening rate was different. With high pulse energies photodarkening was more effective even in fast scanning speeds and it was nearly the same with the ones obtained at lower pulse energy but slower scanning speeds. So it means that fluence is important for photodarkening.

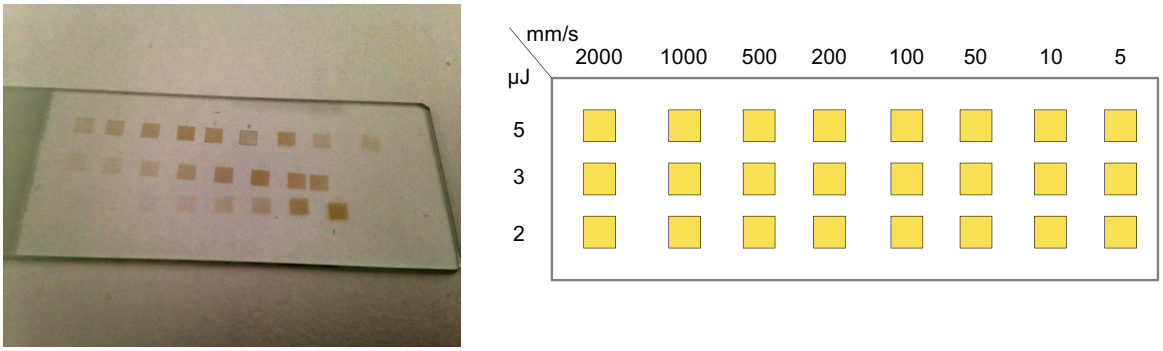


Figure 5.8: Photo and schematic for the glass photodarkening experiments done by changing pulse energy and scanning speed

But if you scan the sample very slow, even at high pulse energies photodarkening vanishes, which means that cumulative heat is also effecting it and causing it to vanish. To confirm that, we have made some photodarkening on a glass sample and put it into an oven which is 500 °C and waited for half an hour. After that we left it to cooldown at room temperature. In the end photodarkening was completely vanished which shows it is a reversible effect. In Figure 5.8 photo for photodarkened samples is given with the diagram shows the squares' scanning speeds at different pulse energies. Using these values, intensity threshold for photodarkening for our glass samples is found to be 14 TW/cm^2.

5.4 Conclusion

Since glass is a brittle and transparent material, it is hard to process using conventional mechanical and laser methods especially in 3D. Using femtosecond pulsed laser, multiphoton ionization makes it possible to process the glass. But the pulse energies needed to process laser is relatively high and generally solid-state lasers are used for this purpose. Since these lasers are hard to operate, big in size and costly, fiber lasers constitute an alternatve since they can reach to the same pulse energies with proper design. In this study, we developed a fiber laser system that

can generate 8 μJ pulses at 200 kHz with burst-mode option at 50 kHz, with pulse duration around 300 fs and in a user-friendly and turn-key manner. The laser output is coupled into a galvo scanner with 2 m/s which is synchronized with a translation stage, which provides a total of 10 cm x 10 cm process area. The galvo scanner is placed on a z-translation stage which aids in finding the focal plane precisely. Using this system, engraving and cutting experiments are done on glass, quartz and alexandrite specimens. In addition, glass ablation and photodarkening fluence threshold is examined using the same system by focusing on surface and inside the glass.

Chapter 6

Conclusion

In the first part of this thesis study, we have developed an integrated ultrashort fiber laser-microscope system and utilized it for sub-cellular surgery. The system is comprised of a mode-locked oscillator that is seeding a multi-stage amplifier which incorporates a fiber-pigtailed AOM that is controlling the repetition rate of the system, a diffraction grating pair that is compressing the pulses and a telescope system used for preparing the beam for coupling into the microscope. Another free-space AOM is placed between compressor part and microscope in order to control laser exposure duration on sample as well as pulse repetition rate. The laser output is coupled to a flurescence microscope system with computerized imaging and precise sample positioning.

The system's capability is first tested on frozen mouse gastrocnemius muscle tissue by performing photodisruption. Using this system, 2.2 μm cuts are made on the specimen using a 20X microscope objective. After that cellular ablation studies are made on fixated osteosarcoma cells by using 60X objective. Sub-micron features are obtained using this system proving that the processing is made by a nonlinear ablation mechanism since the cuts are smaller than our laser's wavelength.

Further trials are made on single organelle by using 100X objective. In order

to do this experiment, mitochondria of cells are stained using organelle specific fluorescent dyes. The laser is applied onto a single targeted mitochondrion, and disappearance of fluorescence light is observed. In order to understand the fluorescence disappearance is caused by the ablation or the photobleaching that the laser irradiance may cause, FRAP (fluorscence recovery after photobleach) technique is applied and the ablation is confirmed. Irradiated cells are monitored for the next few hours and it is observed that they preserve the cell viability, showing that the laser pulses do not cause damage to the surrounding area and not affect cell viability.

Nonlinear biophotonics or ultrashort-pulsed biophotonics is a novel research area and offers a potential for biological applications. Over the past decade, a number of proof-of-principle study demonstrated that such a methodology is extremely efficient and provides an exceptional control both on spatial and temporal domains. In addition to those proof-of-concept studies, publications utiilizing this methodology as an experimental tool have begun to accumulate in the scientific literature as well. Thereby it seems that, especially by taking the above-mentioned advantages of fiber lasers, the diversity of applications of ultrashort-pulsed biophotonics will continue to develop in further different directions, in addition to the fact that biologists will further adopt this methodology as a routine technique for their laboratories.

In the second part of thesis study we have built a fiber laser setup for photoacoustic imaging. Available lasers in the market that are used for photoacoustic signal generation have specific characteristics. Although, some have tunability over wavelength on the expense of energy, repetition frequency and pulse energies are usually constant. As a result of the constraints, lasers are chosen regarding the application and the probes that will be imaged. A laser suitable for melanoma cell detection with a wavelength of 1064nm, e.g., is not appropriate for hemoglobin imaging since at the particular wavelength the absorption of hemoglobin is very low. Another laser with tunable wavelength may not be used for real time imaging because of having low PRF. Lasers having control over pulse repetition rate, usually fiber lasers, have fixed wavelengths which is not suitable for spectroscopic measurements. Fixed energy obligates to perform

microvasculature or cellular imaging. In this study, the laser designed specifically for photoacoustics gives freedom to select wavelength between 600 nm and 1100 nm , energy between 2 nJ to 10 μJ, and repetition frequency between 50 kHz to 3 MHz, thus allows only one laser usage for many different applications. The system comprises of a NOLM fiber laser oscillator that is generating 1-3 ns flat top pulses, followed by multi-stage amplifier system including an AOM for repetition rate control via an FPGA based circuit, and a PCF spliced to the end of the power amplifier to generate supercontinuum from the nanosecond pulses. The system is built and utilized for photoacoustic sginal generation using a ceramic sample in a water tank. Photoacoustic signal is generated and verified using the distance measurements. After that the laser is transferred to the Boğaziçi University Photoacoustics Research Laboratory. Further studies on biological samples for obtaining photoacoustic image by scanning the sample using a translation stage are going on in collaboration with UFOLAB.

In the third part of the thesis study, an Yb-doped fiber laser and amplifier system is utilized for a THz-TDS system for fast scanning THz measurements. Conventionally THz-TDS systems use linear delay lines to change delay between generation and detection arms for spectroscopy system. However, this method takes tens of minutes to scan all the THz range. In this thesis study, an Yb-doped fiber laser is utilized for OSCAT technique, which needs much less scanning times, by adding adjustability to the oscillator pulse repetition rate. This tunability is provided by placing one of the collimators of the oscillator onto a translation stage. After building the system, characterization of the system is realized and THz waveforms are measured for verficaton of the ability of the system.

The oscillator that is built is designed to have zero net GVD. The desired repetition rate is 50 MHz and tunability of 50 kHz is designated. For this tunability range, 6 mm of translation stage movement is needed. During the scan movement, the repetition rate linearity is examined and found to be very linear (8.9 kHz/mm). 53 kHz of repetition rate tunability is achieved around the central frequency of 51 MHz, which are quite close to the desired parameters. 90 mW at the output of the amplifier is obtained with 82 fs of pulses, which is sufficient to cover all THz range. While scanning the repetition rate, fluctuations in the

amplitudes and pulse durations are measured to be %1 and %4 respectively. Both of these parameters are better than the previously obtained Er-doped fiber laser parameters in the past. According to these parameters, a high-dynamic range THz-TDS system is achievable using this laser.

Using this laser system, preliminary THz-TDS measurements are also done and acquired quite good results. The obtained signal-to-noise measurement is 60, and during the measurements system preserved the mode-lock state and the stability in the pulse parameters. Further studies are going on in METU for implementing it with OSCAT technique for fast THz-TDS measurements. Using this technique, scan times of obtaining one THz waveform for THz-TDS measurements is planned to be less than one minute.

In the last part of this thesis study, a femtosecond fiber laser with high pulse energy that can generate both uniform and burst-mode pulses is utilized for glass processing. Since glass is a transparent material at our operation wavelength of 1 μm, processing it is possible only by inducing nonlinear absorption mechanism on it. Nonlinear absorption mechanism's biggest advantage is the possibility to make 3D structures inside transparent materials since it selectively affects just the focal volume. The laser system that is built for this purpose is capable of generating 8 μJ pulses with 300 fs pulse duration at 200 kHz uniform repetition rate or 50 kHz repetition rate at burst-mode operation. The system output is coupled to a galvo-scanner through a telescope system to fill the aperture of the galvo-scanner in order to obtain inimum focal spot on the sample. Using a 56-mm f-theta lens at the output of galvo-scaner, slightly less than 10 μm spot size is obtained. Galvo scanner is also combined with a translation stage in order to achieve higher scanning areas(10 cmx 10 cm). Consequently, very precise(resolution 2 μm and fast system (2m/s) with very large processing area (10 cmx 10 cm) is accomplished. System is designed to be commercialized for the use in Şişecam,Inc. R&D department for laser-glass processing experiments. So it has user friendly computer interface to control pulse repetition rate, adjustment on pulse energy and average power, observation of spectrum in real-time in addition to a single interface for controlling and forming the sequences for galvo-scanner and translation stage.

As a summary, pulsed fiber lasers are increasingly finding applications in many different areas. While it is replacing currently dominating laser technologies like Ti:sapphire lasers, it also creates its new niche application areas that the other lasers could not be utilized due to their complexity, price and size. Since it is misalignment-free, it is easier to commercialize for being easier to operate. Another big advantage of fiber laser is the high surface to volume ratio makes it better candidate for high-power applications. However, biggest improvement necessity is on the side of stability, especially for the mode-locked fiber lasers. NPE-based modelocks are being highly affected by the environmental effects. By overcoming this problem and further increase in pulse energies that the fiber lasers can achieve, their usage in both research and industry will continue to grow.

Bibliography

[1] A. W. Snyder and J. Love, *Optical waveguide theory*, vol. 190. Springer Science & Business Media, 1983.

[2] E.-G. Neumann, *Single-mode fibers*. Springer-Verlag, Berlin, 1988.

[3] G. P. Agrawal, *Nonlinear fiber optics*. Academic press, 2007.

[4] R. W. Boyd, *Nonlinear optics*. Academic press, 2003.

[5] R. H. Stolen, J. P. Gordon, W. Tomlinson, and H. A. Haus, "Raman response function of silica-core fibers," *JOSA B*, vol. 6, no. 6, pp. 1159–1166, 1989.

[6] K. J. Blow and D. Wood, "Theoretical description of transient stimulated raman scattering in optical fibers," *Quantum Electronics, IEEE Journal of*, vol. 25, no. 12, pp. 2665–2673, 1989.

[7] P. Mamyshev and S. V. Chernikov, "Ultrashort-pulse propagation in optical fibers," *Optics letters*, vol. 15, no. 19, pp. 1076–1078, 1990.

[8] D. Gloge, "Weakly guiding fibers," *Applied Optics*, vol. 10, no. 10, pp. 2252–2258, 1971.

[9] O. Martinez, J. Gordon, and R. Fork, "Negative group-velocity dispersion using refraction," *JOSA A*, vol. 1, no. 10, pp. 1003–1006, 1984.

[10] M. Suzuki, N. Edagawa, H. Taga, H. Tanaka, S. Yamamoto, and S. Akiba, "10 gb/s, over 12200 km soliton data transmission with alternating-amplitude solitons," *Photonics Technology Letters, IEEE*, vol. 6, no. 6, pp. 757–759, 1994.

[11] M. J. Digonnet, *Rare-earth-doped fiber lasers and amplifiers, revised and expanded*. CRC press, 2002.

[12] P. S. J. Russell, "Photonic-crystal fibers," *Journal of lightwave technology*, vol. 24, no. 12, pp. 4729–4749, 2006.

[13] P. Russell, "Photonic crystal fibers," *Science*, vol. 299, no. 5605, pp. 358–362, 2003.

[14] J. Broeng, S. E. Barkou, T. Søndergaard, and A. Bjarklev, "Analysis of air-guiding photonic bandgap fibers," *Optics letters*, vol. 25, no. 2, pp. 96–98, 2000.

[15] B. Mangan, L. Farr, A. Langford, P. J. Roberts, D. P. Williams, F. Couny, M. Lawman, M. Mason, S. Coupland, R. Flea, *et al.*, "Low loss (1.7 db/km) hollow core photonic bandgap fiber," in *Optical Fiber Communication Conference*, p. PD24, Optical Society of America, 2004.

[16] T. A. Birks, J. C. Knight, and P. S. J. Russell, "Endlessly single-mode photonic crystal fiber," *Optics letters*, vol. 22, no. 13, pp. 961–963, 1997.

[17] M. Koshiba and K. Saitoh, "Applicability of classical optical fiber theories to holey fibers," *Optics letters*, vol. 29, no. 15, pp. 1739–1741, 2004.

[18] J. Herrmann, U. Griebner, N. Zhavoronkov, A. Husakou, D. Nickel, J. Knight, W. Wadsworth, P. S. J. Russell, and G. Korn, "Experimental evidence for supercontinuum generation by fission of higher-order solitons in photonic fibers," *Physical Review Letters*, vol. 88, no. 17, p. 173901, 2002.

[19] I. Duling, "Subpicosecond all-fibre erbium laser," *Electronics Letters*, vol. 27, no. 6, pp. 544–545, 1991.

[20] I. N. Duling, "All-fiber ring soliton laser mode locked with a nonlinear mirror," *Optics letters*, vol. 16, no. 8, pp. 539–541, 1991.

[21] P. France, *Optical fibre lasers and amplifiers*. Springer, 1991.

[22] I. Duling III, R. Moeller, W. K. Burns, C. Villarruel, L. Goldberg, E. Snitzer, and H. Po, "Output characteristics of diode pumped fiber ase sources," *Quantum Electronics, IEEE Journal of*, vol. 27, no. 4, pp. 995–1003, 1991.

[23] A. Komarov, H. Leblond, and F. Sanchez, "Passive harmonic mode-locking in a fiber laser with nonlinear polarization rotation," *Optics communications*, vol. 267, no. 1, pp. 162–169, 2006.

[24] H. Haus, K. Tamura, L. Nelson, and E. Ippen, "Stretched-pulse additive pulse mode-locking in fiber ring lasers: theory and experiment," *Quantum Electronics, IEEE Journal of*, vol. 31, no. 3, pp. 591–598, 1995.

[25] U. Keller, K. J. Weingarten, F. X. Kartner, D. Kopf, B. Braun, I. D. Jung, R. Fluck, C. Honninger, N. Matuschek, and J. Aus der Au, "Semiconductor saturable absorber mirrors (sesam's) for femtosecond to nanosecond pulse generation in solid-state lasers," *Selected Topics in Quantum Electronics, IEEE Journal of*, vol. 2, no. 3, pp. 435–453, 1996.

[26] X. Zhou, D. Yoshitomi, Y. Kobayashi, and K. Torizuka, "Generation of 28-fs pulses from a mode-locked ytterbium fiber oscillator," *Optics express*, vol. 16, no. 10, pp. 7055–7059, 2008.

[27] I. P. Kaminow, "Polarization in optical fibers," *IEEE Journal of Quantum Electronics*, vol. 17, pp. 15–22, 1981.

[28] K. Tamura, H. Haus, and E. Ippen, "Self-starting additive pulse mode-locked erbium fibre ring laser," *Electronics Letters*, vol. 28, no. 24, pp. 2226–2228, 1992.

[29] H. G. Winful, "Self-induced polarization changes in birefringent optical fibers," *Applied Physics Letters*, vol. 47, no. 3, pp. 213–215, 1985.

[30] C.-W. Chang and S. Chi, "Mode-locked erbium-doped fibre ring laser using nonlinear polarization rotation," *journal of modern optics*, vol. 45, no. 2, pp. 355–362, 1998.

[31] C.-W. Chang and S. Chi, "Ultrashort pulse generation from mode-locked erbium-doped fibre ring lasers," *Journal of Modern Optics*, vol. 46, no. 9, pp. 1431–1442, 1999.

[32] A. E. Siegman, "Lasers. mill valley," 1986.

[33] P. Milonni and J. Eberly, *Lasers*. Wiley Series in Pure and Applied Optics, Wiley, 1988.

[34] D. C. Hanna, *Principles of Lasers*. Springer, 1998.

[35] G. P. Agrawal, "Optical pulse propagation in doped fiber amplifiers," *Physical Review A*, vol. 44, no. 11, p. 7493, 1991.

[36] M. Asobe, T. Kanamori, and K. Kubodera, "Applications of highly nonlinear chalcogenide glass fibers in ultrafast all-optical switches," *Quantum Electronics, IEEE Journal of*, vol. 29, no. 8, pp. 2325–2333, 1993.

[37] U. Keller, "Recent developments in compact ultrafast lasers," *Nature*, vol. 424, no. 6950, pp. 831–838, 2003.

[38] B. Y. Lee, T. Kobayashi, A. Morimoto, and T. Sueta, "High-speed electrooptic deflector and its application to picosecond pulse generation," *Quantum Electronics, IEEE Journal of*, vol. 28, no. 7, pp. 1739–1744, 1992.

[39] R. F. Enscoe and R. J. Kocka, "Electro-optic modulation: Systems and applications," *Lasers Appl*, vol. 6, pp. 91–5, 1984.

[40] D. McCarron, "A guide to acousto-optic modulators," tech. rep., Technical report, Durham University, 2007.

[41] N. Uchida and N. Niizeki, "Acoustooptic deflection materials and techniques," *Proceedings of the IEEE*, vol. 61, no. 8, pp. 1073–1092, 1973.

[42] M. de Lima Jr, M. Beck, R. Hey, and P. Santos, "Compact mach-zehnder acousto-optic modulator," *Applied physics letters*, vol. 89, no. 12, p. 121104, 2006.

[43] D. Royer and E. Dieulesaint, *Elastic waves in solids II: generation, acousto-optic interaction, applications*, vol. 2. Springer Science & Business Media, 2000.

[44] P. Becker, H. Fragnito, C. B. Cruz, R. Fork, J. Cunningham, J. Henry, and C. Shank, "Femtosecond photon echoes from band-to-band transitions in gaas," *Physical review letters*, vol. 61, no. 14, p. 1647, 1988.

[45] C. P. Slichter, *Principles of magnetic resonance*. Sl, 1990.

[46] W. Knox, C. Hirlimann, D. Miller, J. Shah, D. Chemla, and C. Shank, "Femtosecond excitation of nonthermal carrier populations in gaas quantum wells," *Physical review letters*, vol. 56, no. 11, p. 1191, 1986.

[47] J. Goldman and J. Prybyla, "Ultrafast dynamics of laser-excited electron distributions in silicon," *Physical review letters*, vol. 72, no. 9, p. 1364, 1994.

[48] D. Von der Linde, J. Kuhl, and H. Klingenberg, "Raman scattering from nonequilibrium lo phonons with picosecond resolution," *Physical Review Letters*, vol. 44, no. 23, p. 1505, 1980.

[49] D. Von der Linde, K. Sokolowski-Tinten, and J. Bialkowski, "Laser–solid interaction in the femtosecond time regime," *Applied Surface Science*, vol. 109, pp. 1–10, 1997.

[50] P. S. Banks, B. C. Stuart, A. M. Komashko, M. D. Feit, A. M. Rubenchik, and M. D. Perry, "Femtosecond laser materials processing," in *Symposium on High-Power Lasers and Applications*, pp. 14–21, International Society for Optics and Photonics, 2000.

[51] W. Kautek, J. Krüger, M. Lenzner, S. Sartania, C. Spielmann, and F. Krausz, "Laser ablation of dielectrics with pulse durations between 20 fs and 3 ps," *Applied physics letters*, vol. 69, no. 21, pp. 3146–3148, 1996.

[52] B. Stuart, M. Feit, A. Rubenchik, B. Shore, and M. Perry, "Laser-induced damage in dielectrics with nanosecond to subpicosecond pulses," *Physical Review Letters*, vol. 74, no. 12, p. 2248, 1995.

[53] J. Cheng, C.-s. Liu, S. Shang, D. Liu, W. Perrie, G. Dearden, and K. Watkins, "A review of ultrafast laser materials micromachining," *Optics & Laser Technology*, vol. 46, pp. 88–102, 2013.

[54] W. Denk, J. H. Strickler, W. W. Webb, *et al.*, "Two-photon laser scanning fluorescence microscopy," *Science*, vol. 248, no. 4951, pp. 73–76, 1990.

[55] P. So, H. Kim, and I. Kochevar, "Two-photon deep tissue ex vivo imaging of mouse dermal and subcutaneous structures," *Optics express*, vol. 3, no. 9, pp. 339–350, 1998.

[56] M. F. Yanik, H. Cinar, H. N. Cinar, A. D. Chisholm, Y. Jin, and A. Ben-Yakar, "Neurosurgery: functional regeneration after laser axotomy," *Nature*, vol. 432, no. 7019, pp. 822–822, 2004.

[57] L. Sacconi, R. P. OConnor, A. Jasaitis, A. Masi, M. Buffelli, and F. S. Pavone, "In vivo multiphoton nanosurgery on cortical neurons," *Journal of biomedical optics*, vol. 12, no. 5, pp. 050502–050502, 2007.

[58] W. Watanabe, S. Matsunaga, T. Shimada, T. Higashi, K. Fukui, and K. Itoh, "Femtosecond laser disruption of mitochondria in living cells," *Medical Laser Application*, vol. 20, no. 3, pp. 185–191, 2005.

[59] J. Colombelli, E. G. Reynaud, and E. H. Stelzer, "Investigating relaxation processes in cells and developing organisms: from cell ablation to cytoskeleton nanosurgery," *Methods in cell biology*, vol. 82, pp. 267–291, 2007.

[60] A. L. A. Mascaro, L. Sacconi, and F. S. Pavone, "Multi-photon nanosurgery in live brain," *Frontiers in neuroenergetics*, vol. 2, 2010.

[61] P. S. Tsai, P. Blinder, B. J. Migliori, J. Neev, Y. Jin, J. A. Squier, and D. Kleinfeld, "Plasma-mediated ablation: an optical tool for submicrometer surgery on neuronal and vascular systems," *Current opinion in biotechnology*, vol. 20, no. 1, pp. 90–99, 2009.

[62] S. Yavaş, M. Erdogan, K. Gürel, F. Ö. Ilday, Y. B. Eldeniz, and U. H. Tazebay, "Fiber laser-microscope system for femtosecond photodisruption

of biological samples," *Biomedical optics express*, vol. 3, no. 3, pp. 605–611, 2012.

[63] J.-L. Boulnois, "Photophysical processes in recent medical laser developments: a review," *Lasers in Medical Science*, vol. 1, no. 1, pp. 47–66, 1986.

[64] A. Vogel and V. Venugopalan, "Mechanisms of pulsed laser ablation of biological tissues," *Chemical reviews*, vol. 103, no. 2, pp. 577–644, 2003.

[65] A. Chong, J. Buckley, W. Renninger, and F. Wise, "All-normal-dispersion femtosecond fiber laser," *Optics Express*, vol. 14, no. 21, pp. 10095–10100, 2006.

[66] Ö. Ilday, H. Lim, J. Buckley, F. Wise, *et al.*, "Practical all-fiber source of high-power, 120-fs pulses at 1 μm," *Optics letters*, vol. 28, no. 15, pp. 1362–1364, 2003.

[67] T. K. Meyvis, S. C. De Smedt, P. Van Oostveldt, and J. Demeester, "Fluorescence recovery after photobleaching: a versatile tool for mobility and interaction measurements in pharmaceutical research," *Pharmaceutical research*, vol. 16, no. 8, pp. 1153–1162, 1999.

[68] R. Siphanto, K. Thumma, R. Kolkman, T. Van Leeuwen, F. De Mul, J. Van Neck, L. van Adrichem, and W. Steenbergen, "Serial noninvasive photoacoustic imaging of neovascularization in tumor angiogenesis," *Optics express*, vol. 13, no. 1, pp. 89–95, 2005.

[69] J.-T. Oh, G. Stoica, L. V. Wang, M.-L. Li, H. F. Zhang, and K. Maslov, "Three-dimensional imaging of skin melanoma in vivo by dual-wavelength photoacoustic microscopy," *Journal of biomedical optics*, vol. 11, no. 3, pp. 034032–034032, 2006.

[70] H. A. MacKenzie, H. S. Ashton, S. Spiers, Y. Shen, S. S. Freeborn, J. Hannigan, J. Lindberg, and P. Rae, "Advances in photoacoustic noninvasive glucose testing," *Clinical Chemistry*, vol. 45, no. 9, pp. 1587–1595, 1999.

[71] S. Hu, K. Maslov, and L. V. Wang, "Noninvasive label-free imaging of microhemodynamics by optical-resolution photoacoustic microscopy," *Optics express*, vol. 17, no. 9, pp. 7688–7693, 2009.

[72] J. Bodzenta, R. J. Bukowski, A. Christ, and T. Pogoda, "Photoacoustic detection of drug diffusion into a membrane: theory and numerical analysis," *International journal of heat and mass transfer*, vol. 45, no. 22, pp. 4515–4523, 2002.

[73] J. Shah, L. Ma, K. Sokolov, K. Johnston, T. Milner, S. Y. Emelianov, S. Park, S. Aglyamov, and T. Larson, "Photoacoustic imaging and temperature measurement for photothermal cancer therapy," *Journal of biomedical optics*, vol. 13, no. 3, pp. 034024–034024, 2008.

[74] K. Aizawa, S. Sato, D. Saitoh, H. Ashida, and M. Obara, "Photoacoustic monitoring of burn healing process in rats," *Journal of biomedical optics*, vol. 13, no. 6, pp. 064020–064020, 2008.

[75] X. Wang, Y. Pang, G. Ku, X. Xie, G. Stoica, and L. V. Wang, "Noninvasive laser-induced photoacoustic tomography for structural and functional in vivo imaging of the brain," *Nature biotechnology*, vol. 21, no. 7, pp. 803–806, 2003.

[76] S. Yavas, E. Aytac-Kipergil, M. U. Arabul, H. Erkol, O. Akcaalan, Y. B. Eldeniz, F. O. Ilday, and M. B. Unlu, "A novel fiber laser development for photoacoustic microscopy," in *SPIE BiOS*, pp. 85813S–85813S, International Society for Optics and Photonics, 2013.

[77] S. Thomsen, "Pathologic analysis of photothermal and photomechanical effects of laser–tissue interactions," *Photochemistry and photobiology*, vol. 53, no. 6, pp. 825–835, 1991.

[78] V. Levine and R. Geronemus, "Tattoo removal with the q-switched ruby laser and the q-switched nd: Yaglaser: a comparative study.," *Cutis*, vol. 55, no. 5, pp. 291–296, 1995.

[79] C. Swain, P. Salmon, J. Kirkham, S. Bown, and T. Northfield, "Controlled trial of nd-yag laser photocoagulation in bleeding peptic ulcers," *The Lancet*, vol. 327, no. 8490, pp. 1113–1117, 1986.

[80] B. Cox, "Introduction to laser-tissue interactions," *PHAS*, vol. 4886, pp. 1–61, 2007.

[81] P. Li, J. Sage, and P. Champion, "Probing picosecond processes with nanosecond lasers: electronic and vibrational relaxation dynamics of heme proteins," *The Journal of chemical physics*, vol. 97, no. 5, pp. 3214–3227, 1992.

[82] R. Alfano and S. Shapiro, "Emission in the region 4000 to 7000 å via four-photon coupling in glass," *Phys. Rev. Lett.*, vol. 24, pp. 584–587, Mar 1970.

[83] R. Alfano and S. Shapiro, "Observation of self-phase modulation and small-scale filaments in crystals and glasses," *Phys. Rev. Lett.*, vol. 24, pp. 592–594, Mar 1970.

[84] K. Isobe, W. Watanabe, S. Matsunaga, T. Higashi, K. Fukui, and K. Itoh, "Multi-spectral two-photon excited fluorescence microscopy using supercontinuum light source," *Japanese journal of applied physics*, vol. 44, no. 1L, p. L167, 2005.

[85] S. Moon and D. Y. Kim, "Ultra-high-speed optical coherence tomography with a stretched pulse supercontinuum source," *Optics express*, vol. 14, no. 24, pp. 11575–11584, 2006.

[86] M. Balu, L. A. Padilha, D. J. Hagan, E. W. Van Stryland, S. Yao, K. Belfield, S. Zheng, S. Barlow, and S. Marder, "Broadband z-scan characterization using a high-spectral-irradiance, high-quality supercontinuum," *JOSA B*, vol. 25, no. 2, pp. 159–165, 2008.

[87] W. G. Telford, F. V. Subach, and V. V. Verkhusha, "Supercontinuum white light lasers for flow cytometry," *Cytometry Part A*, vol. 75, no. 5, pp. 450–459, 2009.

[88] T. Morioka, H. Takara, S. Kawanishi, O. Kamatani, K. Takiguchi, K. Uchiyama, M. Saruwatari, H. Takahashi, M. Yamada, T. Kanamori, *et al.*, "1 tbit/s (100 gbit/s× 10 channel) otdm/wdm transmission using a single supercontinuum wdm source," *Electronics Letters*, vol. 32, no. 10, pp. 906–907, 1996.

[89] J. Sun, B. Gale, and D. Reid, "Composite frequency comb spanning 0.4-2.4 μm from a phase-controlled femtosecond ti: sapphire laser and synchronously pumped optical parametric oscillator," *Optics letters*, vol. 32, no. 11, pp. 1414–1416, 2007.

[90] W. Wadsworth, N. Joly, J. Knight, T. Birks, F. Biancalana, and P. Russell, "Supercontinuum and four-wave mixing with q-switched pulses in endlessly single-mode photonic crystal fibres," *Optics Express*, vol. 12, no. 2, pp. 299–309, 2004.

[91] S. Popov, J. Taylor, *et al.*, "Continuous-wave, high-power, raman continuum generation in holey fibers," *Optics letters*, vol. 28, no. 15, pp. 1353–1355, 2003.

[92] K. Özgören, B. Öktem, S. Yilmaz, F. Ö. Ilday, and K. Eken, "83 w, 3.1 mhz, square-shaped, 1 ns-pulsed all-fiber-integrated laser for micromachining," *Optics express*, vol. 19, no. 18, pp. 17647–17652, 2011.

[93] J. B. Baxter and C. A. Schmuttenmaer, "Carrier dynamics in bulk zno. ii. transient photoconductivity measured by time-resolved terahertz spectroscopy," *Physical Review B*, vol. 80, no. 23, p. 235206, 2009.

[94] M. C. Beard, G. M. Turner, and C. A. Schmuttenmaer, "Size-dependent photoconductivity in cdse nanoparticles as measured by time-resolved terahertz spectroscopy," *Nano Letters*, vol. 2, no. 9, pp. 983–987, 2002.

[95] M. C. Beard, G. M. Turner, and C. A. Schmuttenmaer, "Transient photoconductivity in gaas as measured by time-resolved terahertz spectroscopy," *Physical Review B*, vol. 62, no. 23, p. 15764, 2000.

[96] J. B. Baxter and C. A. Schmuttenmaer, "Conductivity of zno nanowires, nanoparticles, and thin films using time-resolved terahertz spectroscopy," *The Journal of Physical Chemistry B*, vol. 110, no. 50, pp. 25229–25239, 2006.

[97] F. Ilday, F. Wise, and T. Sosnowski, "High-energy femtosecond stretched-pulse fiber laser with a nonlinear optical loop mirror," *Optics letters*, vol. 27, no. 17, pp. 1531–1533, 2002.

[98] T. Hochrein, R. Wilk, M. Mei, R. Holzwarth, N. Krumbholz, and M. Koch, "Optical sampling by laser cavity tuning," *Optics express*, vol. 18, no. 2, pp. 1613–1617, 2010.

[99] R. Wilk, T. Hochrein, M. Koch, M. Mei, and R. Holzwarth, "Terahertz spectrometer operation by laser repetition frequency tuning," *JOSA B*, vol. 28, no. 4, pp. 592–595, 2011.

[100] R. Ulbricht, E. Hendry, J. Shan, T. F. Heinz, and M. Bonn, "Carrier dynamics in semiconductors studied with time-resolved terahertz spectroscopy," *Reviews of Modern Physics*, vol. 83, no. 2, p. 543, 2011.

[101] Y.-W. Tzeng, Y.-Y. Lin, C.-H. Huang, J.-M. Liu, H.-C. Chui, H.-L. Liu, J. M. Stone, J. C. Knight, and S.-W. Chu, "Broadband tunable optical parametric amplification from a single 50 mhz ultrafast fiber laser," *Optics express*, vol. 17, no. 9, pp. 7304–7309, 2009.

[102] D. Grischkowsky, S. Keiding, M. v. Exter, and C. Fattinger, "Far-infrared time-domain spectroscopy with terahertz beams of dielectrics and semiconductors," *JOSA B*, vol. 7, no. 10, pp. 2006–2015, 1990.

[103] T. Yasui, E. Saneyoshi, and T. Araki, "Asynchronous optical sampling terahertz time-domain spectroscopy for ultrahigh spectral resolution and rapid data acquisition," *Applied Physics Letters*, vol. 87, no. 6, p. 061101, 2005.

[104] H. Keskin, H. Altan, S. Yavas, F. O. Ilday, K. Eken, and A. B. Sahin, "Development of a rapid-scan fiber-integrated terahertz spectrometer," *Optical and Quantum Electronics*, vol. 46, no. 4, pp. 495–503, 2014.

[105] I. Pavlov, A. Rybak, C. Cenel, and F. Ilday, "Balancing gain narrowing with self phase modulation: 100-fs, 800-nj from an all-fiber-integrated yb amplifier," in *Lasers and Electro-Optics Europe (CLEO EUROPE/IQEC), 2013 Conference on and International Quantum Electronics Conference*, pp. 1–1, IEEE, 2013.

[106] B. Pradarutti, G. Matthäus, C. Brückner, J. Limpert, S. Riehemann, G. Notni, S. Nolte, and A. Tünnermann, "Electrooptical sampling of ultrashort thz pulses by fs-laser pulses at 1060 nm," *Applied Physics B*, vol. 85, no. 1, pp. 59–62, 2006.

[107] C. Buerhop, B. Blumenthal, R. Weissmann, N. Lutz, and S. Biermann, "Glass surface treatment with excimer and co2 lasers," *Applied surface science*, vol. 46, no. 1-4, pp. 430–434, 1990.

[108] R. R. Gattass and E. Mazur, "Femtosecond laser micromachining in transparent materials," *Nature photonics*, vol. 2, no. 4, pp. 219–225, 2008.

[109] C. Kerse, S. Yavas, H. Kalaycıoğlu, M. D. Aşık, Ö. Akçaalan, and F. Ö. Ilday, "Efficient, high-speed ablation of soft tissue with few-microjoule, femtosecond pulse bursts," *arXiv preprint arXiv:1410.6730*, 2014.

[110] W. Steen, K. G. Watkins, and J. Mazumder, *Laser material processing*. Springer Science & Business Media, 2010.

[111] B. Stuart, M. Feit, S. Herman, A. Rubenchik, B. Shore, and M. Perry, "Nanosecond-to-femtosecond laser-induced breakdown in dielectrics," *Physical Review B*, vol. 53, no. 4, p. 1749, 1996.

[112] K. Miura, J. Qiu, H. Inouye, T. Mitsuyu, and K. Hirao, "Photowritten optical waveguides in various glasses with ultrashort pulse laser," *Applied Physics Letters*, vol. 71, no. 23, pp. 3329–3331, 1997.

[113] L. Sudrie, M. Franco, B. Prade, and A. Mysyrowicz, "Writing of permanent birefringent microlayers in bulk fused silica with femtosecond laser pulses," *Optics Communications*, vol. 171, no. 4, pp. 279–284, 1999.

[114] E. Glezer, M. Milosavljevic, L. Huang, R. Finlay, T.-H. Her, J. P. Callan, and E. Mazur, "Three-dimensional optical storage inside transparent materials," *Optics Letters*, vol. 21, no. 24, pp. 2023–2025, 1996.

[115] K. Itoh, W. Watanabe, S. Nolte, and C. B. Schaffer, "Ultrafast processes for bulk modification of transparent materials," *MRS bulletin*, vol. 31, no. 08, pp. 620–625, 2006.

[116] J. Chan, T. Huser, S. Risbud, and D. Krol, "Structural changes in fused silica after exposure to focused femtosecond laser pulses," *Optics Letters*, vol. 26, no. 21, pp. 1726–1728, 2001.

[117] R. Brückner, "Properties and structure of vitreous silica. i," *Journal of Non-Crystalline Solids*, vol. 5, no. 2, pp. 123–175, 1970.

[118] K.-i. Kawamura, N. Sarukura, M. Hirano, and H. Hosono, "Holographic encoding of fine-pitched micrograting structures in amorphous sio 2 thin films on silicon by a single femtosecond laser pulse," *Applied Physics Letters*, vol. 78, no. 8, pp. 1038–1040, 2001.

[119] M. Will, S. Nolte, B. N. Chichkov, and A. Tünnermann, "Optical properties of waveguides fabricated in fused silica by femtosecond laser pulses," *Applied Optics*, vol. 41, no. 21, pp. 4360–4364, 2002.

[120] Y. Shimotsuma, P. G. Kazansky, J. Qiu, and K. Hirao, "Self-organized nanogratings in glass irradiated by ultrashort light pulses," *Physical review letters*, vol. 91, no. 24, p. 247405, 2003.

[121] E. Bricchi, B. G. Klappauf, and P. G. Kazansky, "Form birefringence and negative index change created by femtosecond direct writing in transparent materials," *Optics letters*, vol. 29, no. 1, pp. 119–121, 2004.

[122] C. Hnatovsky, R. Taylor, P. Rajeev, E. Simova, V. Bhardwaj, D. Rayner, and P. Corkum, "Pulse duration dependence of femtosecond-laser-fabricated nanogratings in fused silica," *Applied Physics Letters*, vol. 87, no. 1, p. 014104, 2005.

[123] J. Qiu, K. Miura, and K. Hirao, "Three-dimensional optical memory using glasses as a recording medium through a multi-photon absorption process," *Japanese journal of applied physics*, vol. 37, no. 4S, p. 2263, 1998.

[124] C. B. Schaffer, A. O. Jamison, and E. Mazur, "Morphology of femtosecond laser-induced structural changes in bulk transparent materials," *Applied Physics Letters*, vol. 84, no. 9, pp. 1441–1443, 2004.

[125] J. Chan, T. Huser, S. Risbud, and D. Krol, "Modification of the fused silica glass network associated with waveguide fabrication using femtosecond laser pulses," *Applied Physics A*, vol. 76, no. 3, pp. 367–372, 2003.

[126] B. Oktem, C. Ülgüdür, and F. Ö. Ilday, "Soliton–similariton fibre laser," *Nature Photonics*, vol. 4, no. 5, pp. 307–311, 2010.

[127] J. Nicholson, J. Jasapara, W. Rudolph, F. Omenetto, and A. Taylor, "Full-field characterization of femtosecond pulses by spectrum and cross-correlation measurements," *Optics letters*, vol. 24, no. 23, pp. 1774–1776, 1999.